Title	Electrical characterisation of emerging photo anodes suited to water dissociation with an applied bias
Authors	Walsh, Adrian
Publication date	2018
Original Citation	Walsh, A. 2018. Electrical characterisation of emerging photo anodes suited to water dissociation with an applied bias. PhD Thesis, University College Cork.
Type of publication	Doctoral thesis
Rights	© 2018, Adrian Walsh. - http://creativecommons.org/licenses/by-nc-nd/3.0/
Download date	2025-06-07 07:37:22
Item downloaded from	https://hdl.handle.net/10468/6787

Electrical Characterisation of Emerging Photo Anodes Suited to Water Dissociation with an Applied Bias

A thesis presented to

The National University of Ireland, Cork

For the Degree of Doctor of Philosophy

by

Adrian Walsh B.E.

College of SEFS,

Tyndall National Institute,

University College Cork,

2018

Head of College: Professor Paul Ross

Supervised by Dr Ian M. Povey, Prof Paul K. Hurley & Dr Karim Cherkaoui

Contents

2   An investigation of barrier heights for Indium-Tin-Oxide/Silicon Contacts over n and p type silicon   63

3   Investigation into the hole conduction mechanism of ALD grown TiO$_2$ 78

4   Investigating the effect of TiO$_2$ thickness on the electrical conductivity and photoelectrochemical response of metal/TiO$_2$/SiO$_x$/Si photoanodes   104

Declaration

This is to certify that the work I am submitting is my own and has not been submitted for another degree, either at University College Cork or elsewhere. All external references and sources are clearly acknowledged and identified within the contents. I have read and understood the regulations of University College Cork concerning plagiarism.

_____

Signature of author

_____

Date

List of Figures

10

List of Tables

Acknowledgements

Firstly, I would like to extend my sincerest gratitude to my supervisors, Dr Ian Povey, Professor Paul Hurley, and Dr Karim Cherkaoui for this research opportunity at the Tyndall National Institute. In particular for their support, advice and direction during my PhD. A thanks to Professor Martyn Pemble, the PI of the project, to Professor Andrew Mills and Professor Paul McIntyre, our collaborators on the project, with a special thanks to Professor Paul McIntyre and his group for allowing me to spend time in Stanford University to learn the electrochemistry behind a water splitting cell.

Most importantly I would like to thank my partner Jenna for her support and belief during my PhD journey over the last number of years. Additionally, a special thank you for my parents for all of their help for everything, in particular during this PhD. A very special thanks to Dr Barry Hutchinson, for his help throughout this PhD, his friendship and advice. A second special thanks to Louise Ryan, for her help particularly at the end of this journey. Furthermore, I would like to thank Dr Brendan Sheehan, and Melissa McCarthy for their friendship and advice over many years. In addition, I would like to thank all members of both the Advanced Materials and Surfaces Group and the Nanoelectronic Materials and Devices Group, both past and present including Dr Shane O'Brien, Dr Eamon O'Connor, Dr Richard Winfield, Dr Scott Monaghan, Dr Vladimir Djara, Jan Kegal and Igor Kazadojev who have all contributed to making my time spent at Tyndall a very enjoyable experience.

Particular thanks to Dr Patrick Carolyn for the microscopy work which is contained in this thesis and to Dan O'Connell for the many device fabrications. A thanks to Dr Fathima Laffir from the University of Limerick for the XPS measurements that were performed in this thesis.

I would like to thank my friends outside of Tyndall, namely JP Toner, Raymond Santry, Florence McCarthy, Ger O'Callaghan and Tobias Good. Who

have been there in both the good times and the bad times. I would also like to thank my brother Christopher and sister Sinead

Abstract

One of the pivotal challenges of the 21st century is to develop alternative energy sources to replace the inevitable depletion of fossil fuels. One candidate for a non-polluting, abundant and renewable source of energy is sunlight. The significant challenge for the large-scale uptake of solar energy is overcoming the intermittent nature of solar radiation using energy storage methods. Synthesis of fuels from sunlight is one potential storage approach, providing the need for optimized photo-electrochemical devices and materials. The direct photovoltage of water to produce hydrogen and oxygen represents the most direct route to the synthesis of clean fuel. Recently it has been showing that technology from the microelectronics industry can be used to fabricate metal oxide semiconductors for use as photoanodes.

Given that the protective oxide needs to be transparent to allow light to the photoactive material, two possible solutions are available. To have a thicker transparent conducting oxide, such as indium-tin-oxide, which would create a Schottky junction with the silicon below, or to use very thin oxides such as titanium dioxide, which when a catalyst is deposited on top creates a MOS structure.

Of interest to the first option are the electrical properties of the Schottky junction in particular the barrier height, as this will dictate the current flow through to the water and drive the electrochemical reaction. For the second option to be successful, the thin oxide must not have any pinholes, i.e. to isolate the photoactive material below from the water. Atomic layer deposition is able to provide this level of conformality. A conduction mechanism study was performed and an investigation into the relationship between the stoichiometry of the titanium dioxide and the leakage current. It was shown that the level of oxygen vacancies played a key role in the level of leakage current, but a dominant conduction mechanism was not proved. Next a study into how the

thickness affects the conduction through the films was performed, where results show that an increased thickness results in an increased leakage current, opposite of what would be expected. Some ellipsometry data shows a definite change in the films as they get thicker. The relationship between these electrical properties and the electrochemical properties of interested in a water splitting cell were also studied and shown that it is not always possible to compare the two, especially when, the electrochemical measurement includes a light source.

In addition, an investigation into deposition of mixed oxides based on titanium dioxide, was undertaken, using a novel ALD method whereby the titanium precursor was not pulsed in saturation. In this way a number of reaction sites were left unfilled, meaning that when a second metal precursor was pulsed, a single cycle of growth contained two different types of metal atoms, as opposed to the more traditional method of the supercycle detailed in chapter 1. The electrical properties of these films were measured, and a definitive trend showed that, creating mixed oxides in this way can change the electrical properties but that the incorporated amount of the second metal is an important factor. An anneal study was found to vastly change the electrical properties of these mixed oxides samples, where the leakage current fell by a number of orders of magnitude. For a water splitting application, this is not a desirable effect.

Chapter 1

Introduction

1.1 Overview

Solar radiation provides a potentially vast source of energy, some of which may be employed to produce chemical fuels to replace hydrocarbons. As countries move away from fossil fuels, there has been a lot of interest in renewable energy sources, of which the solar energy resource dwarfs all other energy sources, renewable and fossil combined [1]. In order to be a legitimate replacement for fossil fuels, solar energy must be captured, converted and stored in a cost-effective and easily utilised fashion. Water has attracted the most attention as a feedstock for solar fuel synthesis at a large scale. Where water is split into hydrogen (H_2) and oxygen (O_2), hydrogen has the potential to meet the requirements as a clean non-fossil fuel, and doubles as a way to store the energy from the sun. One major challenge is the harvesting of this solar energy. One method is to use photoactive materials to create a voltage to split water, in a photoelectrochemical cell (PEC) in which solar energy is directly harvested to drive the water splitting reaction. Another major challenge is to make the PEC cost effective. Due to the materials that are used in solar water splitting devices at present, such as iridium, which is used as the oxygen evolution catalyst, the price per kWh is very high. Therefore reducing

manufacturing cost so that the price per kWh is able to rival current fossil-based technologies is a key consideration. One of the goals of solar water splitting cells, is to use cheap and relatively abundant materials for the semiconductor photoactive layer, the surface protection layers and the H_2 and O_2 evolution catalysts. [1–3]

More specifically, what is needed is an efficient and long-lived system for splitting water, with light in the terrestrial $(AM1.5)$[1] solar spectrum at an intensity of one sun, to obtain hydrogen fuel [2]. For practical systems an efficiency of 10% is necessary [2]. An efficiency of 10% means that the hydrogen and oxygen produced have a fuel value of 10% of the solar energy required to produce them. For example, if the instantaneous maximum intensity of the sun is approximately 1 kW/m^2 and the average intensity of a 24-hour day over the course of the year is about 250 W/m^2, then hydrogen should be produced at about 0.7g/s per m^2 at maximum solar intensity, and at a cost of \$2-4/kg H_2. Long-lived implies an operating lifespan of 10 years, this includes the photoactive materials, catalysts and the materials of the systems and that they will not be degraded under irradiation. [2]

Fujishima and Honda first demonstrated water splitting using a photoelectrochemical junction in 1972 [4], and it has progressed significantly since then [2, 3, 5–9]. Simple semiconductor liquid junctions were initially used, where the photogenerated holes in the semiconductor interact directly with the liquid. Figure 1.1 shows the schematic of a water splitting cell. This shows a semiconductor anode, but the anode could also be a metal with separate photovoltaic cell. Here, photons are absorbed in the semiconductor anode generating an electron-hole pair. Due to band bending, the electrons flow

---

[1]The Air Mass is the path length which light takes through the atmosphere normalised to the shortest possible path length (that is, when the sun is directly overhead). The Air Mass quantifies the reduction in the power of light as it passes through the atmosphere and is absorbed by air and dust. The air mass coefficient is commonly used to characterise the performance of solar cells under standardised conditions

[2]1 sun is typically defined as the nominal full sunlight intensity on a bright clear day on Earth, which measures 1000 W/m^2

towards the cathode to drive the hydrogen evolution reaction, while the holes flow towards the semiconductor-liquid junction to drive the oxygen evolution reaction. The conduction and valence bands of the semiconductor must straddle the hydrogen and oxygen evolution bands of the water in order to drive the reaction. They also have to be able to drive the overpotentials of the two reactions. Metal-oxide-semiconductor photoanodes described below have gained much traction, where the oxide is ideally conductive to electrons and/or holes but is impermeable to water and therefore stopping oxidation of the semiconductor, which will cut off the H_2 and O_2 evolution reactions. The metal of the photoanode is then chosen to be a catalyst for the H_2 reaction, such as iridium, or nickel [10].
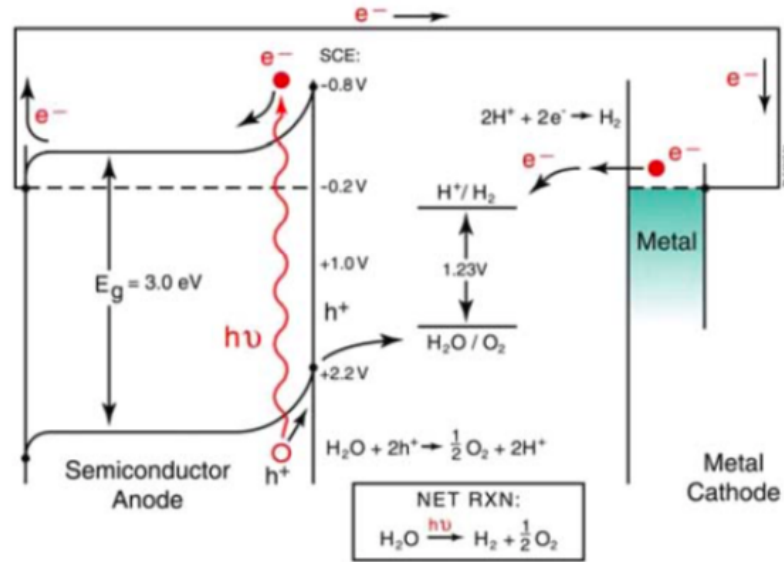
Figure 1.1: Schematic of water splitting using a semiconducting photoanode with 3.0 eV bandgap. Adapted from [11].

Three different junction types have been investigated for water splitting photoanodes: semiconductor-liquid junction (SL, herein referred to as Type 0) requiring a stable semiconducting metal oxide in contact with water; Schottky junctions, either with a direct metal contact to the semiconductor [12, 13], or with an interposed protective metal oxide layer, forming a MIS (or Type 1) structure [10, 14, 15]; and buried pn junctions (Type 2), which likewise may [15] or may not [16] incorporate additional protective oxides. The fabrication

complexity increases, in general, from Type 0 to 1 to 2 and the hole extraction barrier induced by protection layers can be made to decrease accordingly for each type, for the same insulator layer. Figure 1.2 shows the three different junction types. Here, each junction configuration is shown for a silicon cell protected by TiO_2. The insulators introduce a series resistance, which when located inside the junction constitutes an extraction barrier. Therefore, the density of holes at the interface and the density of states of the contact play a key role. In Type 0 cells, holes will be accumulated at the semiconductor/insulator interface during current flow, and charge transfer may still be significantly limited owing to a low density of states in the contact. Such a situation may arise from using electrolytes as well as non-metallic catalysts as the hole conduction mediator. In Type 1 cells, moderate hole accumulation is sufficient to efficiently extract minority carriers, but the photovoltage suffers an insulator-thickness-dependent loss. In Type 2 cells, the p+ region ensures a high hole concentration at the interface that is independent of illumination and bias, resulting in no barrier to hole extraction. As a result, these cells exhibit no dependence of photovoltage on the insulator thickness and achieve record photovoltages at all oxide thicknesses and pH values studied.

A number of protection layers have been investigated such as TiO_2 grown by chemical vapour deposition [18], noble metal [19] and noble metal silicide [20] layers, however, most were unsuccessful at both obtaining a high performance, and a long-lasting PEC. Due to the nature of the PECs, the protective layer needs to minimize the resistance to hole transport, while still preventing oxidation of the substrate. In 2011 Chen *et al.* [14] showed that a Si substrate with a native oxide layer could be coated with a pinhole-free 2 nm TiO_2 layer grown by ALD. This layer was able to prevent oxidation of the Si substrate while being thin enough to allow the tunnelling of holes from the Si substrate to the catalyst top layer.

The work of Chen *et al.* [17] (see Appendix .2), demonstrates the results of
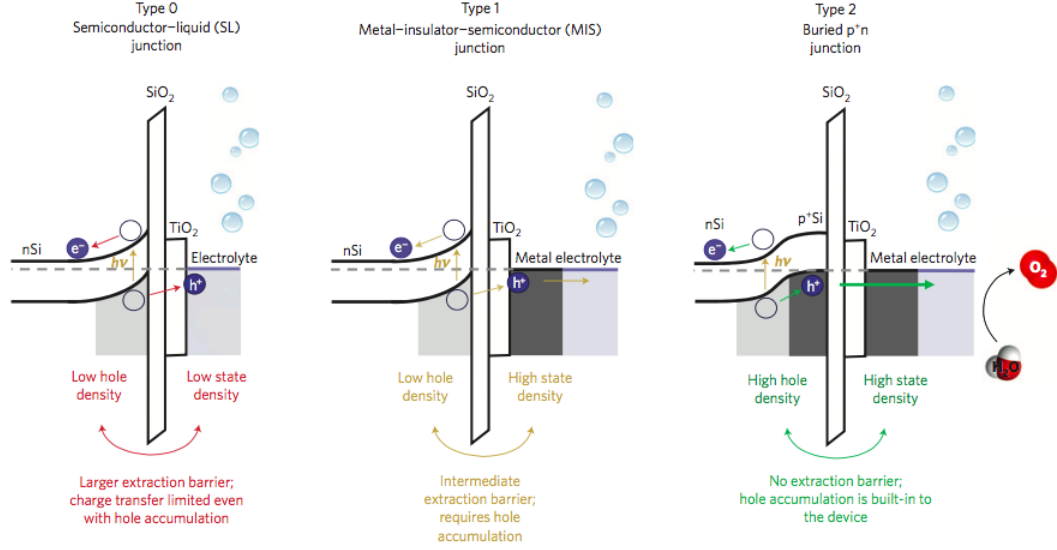
Figure 1.2: Three junction types showing the extraction barrier imposed by the protection layer illustrated with silicon water-oxidation photoanodes. Three types of photoanode junctions have been employed in the literature, the Type 0 semiconductor–liquid (SL), Type 1 MIS Schottky, and Type 2 MIS p+n junction. Adapted from [17].

the new design i.e. Type 2 junction. The junction reported achieves the highest photovoltage for water-splitting silicon photoanodes to date at 630 mV. The loss mechanism is systematically probed in metal-insulator-semiconductor Schottky junction cells compared to buried junction p+n cells. revealing the need to maintain a characteristic hole density at the semiconductor/insulator interface. The paper goes further to formulate design principles to maximize the photovoltage of oxide-protected water splitting anodes, from interface quality and hole extraction to the optimization of the built-in field.

1.2 Thesis Motivation

In the work outlined in this thesis, protective oxides are investigated for water splitting applications. First indium-tin-oxide (ITO) is investigated. ITO is a transparent conductive oxide (TCO) and is commonly used in photovoltaic applications. TiO_2 is also investigated, which has been shown to be an interesting conductive protective oxide for water splitting applications. The

majority of this thesis concentrates on TiO_2 as the protective oxide of choice for silicon photoanodes.

Chapter 2 investigates the electrical properties of ITO on silicon photoanode, in particular looking at the Schottky junction formed between the ITO and the silicon. Although ITO is promising as a protective oxide, it has a number of drawbacks, including cost and stability at different pH levels. Consequently, TiO_2 has been investigated further. The subsequent chapters concentrate on TiO_2 as the protective oxide for the water splitting cells.

Chapter 3 investigates the current conduction mechanism through the TiO_2 and the role that the Ti^{3+} to Ti^{4+} ratio and therefore the oxygen vacancies, have on conduction. In order to understand the role stoichiometry plays, samples were grown under a number of different reaction conditions, resulting in films of different levels of oxygen vacancies. Then after determining the conduction methods of the samples, this mechanism was related to the stoichiometry of the films; the Ti^{3+} to Ti^{4+} ratio.

Chapter 4 involved the growth of a thickness series of TiO_2. The conduction of the thin film samples by electrical testing was compared to conduction of the samples when tested in an electrochemical cell, to examine particular aspects of performance in a water splitting PEC.

Chapter 5 investigates a novel ALD method for creating mixed oxides. A number of different metals were introduced into the TiO_2 film to change the electrical properties. An annealing study was performed on the mixed oxide thin films and their properties are assessed

1.3 Atomic Layer Deposition: An Overview

Atomic layer deposition (ALD) is a chemical vapour deposition (CVD) variant, that is able to produce highly conformal, precise growth control of ultra-thin

films [21–23]. An ALD cycle typically consists of two separate surface reactions that are self-limiting, thus allow the control of film growth at the monolayer level.
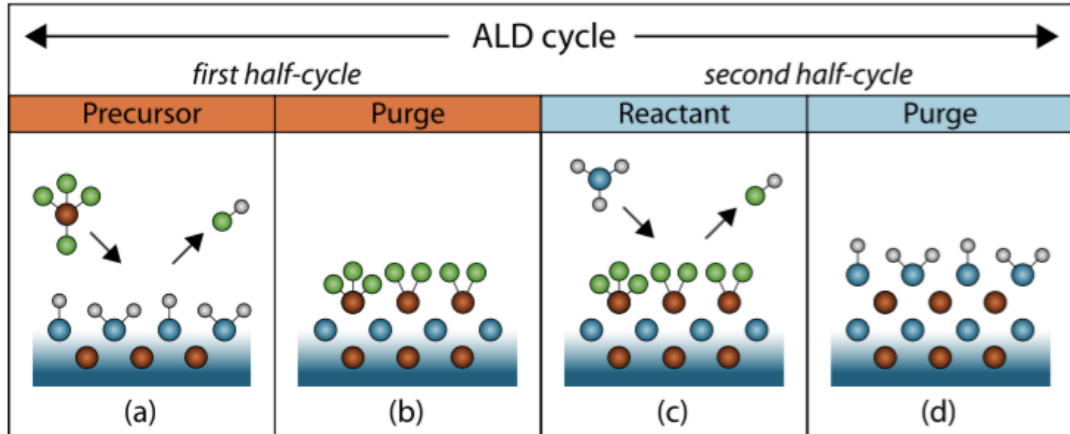
Figure 1.3: Basic ALD process, adapted from [24]. a) Consists of a surface limited reaction of the precursor onto the surface, b) A purge step to remove any excess precursor, c) The second precursor enters the chamber and reacts with the surface of the adsorbed first precursor, d) A second purge step to remove any excess of the second precursor. This completes the ALD cycle of one sub-monolayer and the process is repeated until the desired thickness is obtained.

1.3.1 Principle of an ALD cycle

The basic principle of ALD is that it operates as a sequence of alternating surface self-limiting half reactions as illustrated in figure 1.3. During each cycle the first gaseous reactant enters the vacuum deposition chamber, which reacts with the sample surface. Then a purge removes the excess of this reactant before the second gaseous reactant is pulsed into the chamber. The purge ensures the separation of the reactants. ALD uses precursors in the vapour phase which are chemically adsorbed (chemisorbed) onto the heated substrate surface. The gas purge removes any species that are physically adsorbed (physisorbed). Leaving one sub-monolayer grown. This cycle is then repeated in order to achieve the desired thickness.

1.3.2 ALD Processes

The most studied ALD method is thermal-ALD. This ALD method is driven by the thermal energy from the heating of the substrate. In addition, there is a temperature gradient, from the precursor (low end) to the substrate (high end), to maximise chemisorption at the substrate and thus growth. [24, 25]

Plasma enhanced ALD (PEALD) has gained a lot of momentum in recent years. PEALD utilises a more energetic, co-reactant in the form of a plasma, such as an oxygen plasma. PEALD can reduce the thermal budget of a thermal process. O_2 plasmas are very effective co-reactants that can remove organic ligands much easier than water, by O-radical driven combustion-like surface reactions [26, 27] Therefore plasma-based processes generally produce high quality materials at lower substrate temperatures. Other plasmas can be used to extend the variety of materials grown beyond oxides [25, 28].

Generally, film growth consists of two clear regimes, nucleation and bulk growth. Nucleation is dependent on the precursor and the substrate used. Nucleation regimes are studied in detail in order to understand the growth process. The nucleation regime can also affect the bulk regime, as it may lead to a bulk film of a particular phase. As the nucleation regime is different on different substrates, this can lead to differences in the bulk on different substrates.

1.3.3 The self-limiting ALD regime

The cyclic nature of ALD described in section 1.3.1 allows a material to be deposited monolayer by monolayer. This is due to the gaseous reactant only reacting with the substrate surface. The reactant will initially chemisorb onto the surface, with subsequent layers physisorbing on top of this. These subsequent layers will ideally detach, due to the weak physisorbsion bonds,

during the purge stage of the ALD cycle. However, if the purge is not sufficient some physisorbed molecules will remain. This ideal behaviour results in a monolayer of material chemisorbed onto the surface, non-ideal behaviour results in sub-monolayer growth. Equation 1.1 is the equation for the calculation of monolayer coverage during a pulse. It is defined as the number of atoms that remain on the substrate divided by the number of atoms needed for one monolayer of coverage. [29]

$$\Theta = (I_i - I_e)t_i/\Theta_i \tag{1.1}$$

Θ the atomic density for one monolayer coverage ($\Theta = 1$)

I_i the number of atoms per second impinging on the substrate of unit area

I_e the number of atoms per second re-evaporated from the substrate during deposition

t_i the duration of the pulse

Ideally, any species that is physisorbed onto the surface will be re-evaporated and only the chemisorbed, bonded species will remain. Chemisorbsion can occur as part of the ALD mechanism in one of three ways; ligand exchange, dissociation or association [29].

(i) *Ligand exchange mechanism*

The reactant molecule (ML_n) is adsorbed onto the surface ($\|$-S). One or more ligands from the molecule (-L) bonds with a surface ligand (-S) forming the volatile compound (LS) which is removed during the purge as an unreacted by product, then allowing the reactant molecule to bond to the surface forming ($\|$M) Equation 1.2.

$$\|\text{-}S + ML_n(g) -> \|\text{-}ML_{n-1} + LS(g) \tag{1.2}$$
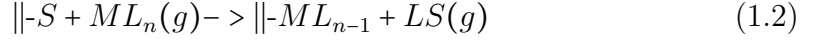
(ii) *Dissociative mechanism* In this method the incoming reactant (ML$_n$) is divided between multiple reactive sites ($\|$-M*-Z$\|$) on the surface Equation 1.3. No gaseous by-products are forming instead two species are coordinated to the substrate surface.

$$\|M*\text{-}Z\| + ML_n(g) -> \|\text{-}M*\text{-}L + \| - Z\text{-}ML_{n-1} \tag{1.3}$$
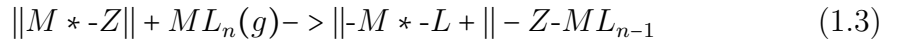
(iii) *Associative mechanism* The reactant (ML$_n$) forms a bond with an active site on the substrate surface and is chemisorbed without the release of ligands, Equation 1.4

$$| + ML_n -> \|{-}\!\!-\!\!-ML_n \tag{1.4}$$

Ligand exchange is reported as being the preferred mechanism of chemisorption during ALD, as its equilibrium favours toward the product by removing gaseous by-products [29, 30].

Generally, ALD consists of two growth regimes, nucleation and bulk growth. As nucleation may differ considerably depending on the substrate, it can affect the material properties of the film to a large degree. Nucleation may lead to a bulk film of a particular phase (templating) or introduce strain into the film and therefore influence the bulk growth regime.

During the nucleation regime, full monolayer growth is not always achieved. There will therefore be other elements or vacancies within the film. Other elements originate from the ligands of the precursor. The number of reaction sites bonded to will affect the stoichiometry, if not all are filled then this will create defects. The nucleation regime is affected by the substrate which

26

determines the number of available reaction sites.

In ALD the stoichiometry of the film can also be affected by a large number of parameters. The temperature for example can affect the reaction, where in general the lower the temperature, the greater incorporation of other elements from the ligands. Non-stoichiometry of the film can have large effects on the properties of the film. As this thesis will show, the stoichiometry of TiO_2 can be used to understand the electrical properties, and modification of the stoichiometry can be used to change these properties.

1.3.4 Growth per cycle

Once precursor doses are in excess of saturation (i.e. a monolayer of coverage) the growth per cycle (GPC), which is generally less than a monolayer of grown film, is determined by a combination of available surface sites, sticking coefficient and steric hindrance of ligands on the substrate surface [30]. The number of available surface sites is dependent on the substrate, the growth temperature and how the substrate is terminated. If the surface is H terminated it is usually not an active site, however an O-H terminated surface is an active site. The sticking coefficient is the reaction probability between a single precursor molecule, with a free reactive surface site. steric hindrance of ligands happens when a precursor molecule bonds with an active site, but due to bulky ligands, blocks adjacent active sites from incoming precursor molecules. Ritala *et al.*, demonstrates this for the growth of TiO_2 using different precursors [31]. With a well understood ALD process, very accurate thickness control can be obtained.

1.3.5 ALD Temperature Window

ALD reactions generally take place in the temperature range of 150°C to 400°C with some films possible to grow colder or hotter. The ALD window is the

temperature range at which deposition can occur within the self-limiting regime, as shown in figure 1.4. At lower temperatures, the reaction may not complete due to insufficient energy, or it is possible for the precursor to condense and therefore not produce a self-limiting reaction. At hotter temperatures the precursor can decompose or the precursor molecule can re-evaporate from the surface after initial bonding [32].
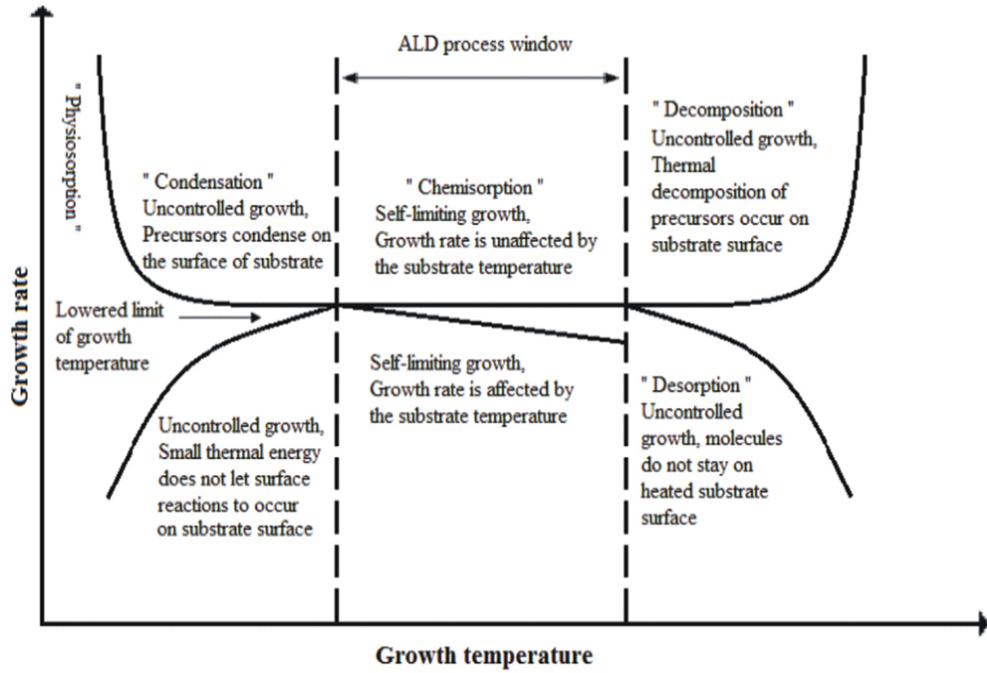
Figure 1.4: ALD temperature window. Adapted from [33].

1.3.6 Aluminium Oxide

The ALD of Al_2O_3 using trimethylaluminum (TMA) and water has developed as a model ALD system. The first references of this process date back to the 1980's and early 1990's [34, 35]. Although it is possible to use other precursors (e.g. $AlCl_3$, $Al(C_2H_5)_3$, etc.) and other co-reactants (e.g. ozone [36, 37], oxygen plasma), this section will only discuss the TMA and H_2O reaction as it has been thoroughly studied [30], being considered the ideal case ALD reaction, mostly due to the highly conformal growth over a wide temperature range (33^oC - 300^oC [38]), and substrates, including 3D structures [30].

28

The surface reactions during the TMA and H_2O ALD reaction are described via the two half reactions (equations 1.5, 1.6) giving the overall reaction, equation 1.7. [23, 39, 40]

$$AlOH^* + Al(CH_3)_3 \longrightarrow AlOAl(CH_3)_2{}^* + CH_4 \qquad (1.5)$$

In the first half reaction TMA reacts with the O-H terminated surface (where the asterisks denote the surface species), to form an Al-O bond and the release of a CH_4 molecule, which is purged away.

$$AlCH_3{}^* + H_2O \longrightarrow AlOH^* + CH_4 \qquad (1.6)$$
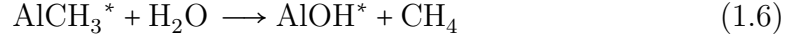
In the second half reaction, the water reacts with the $AlCH_3^*$ surface resulting a new OH terminated AlO surface and the release of a CH_4 molecule. The surface reactions are very efficient and self-limiting, with the main driver for the efficient reactions being the formation of a very strong Al-O bond, the complete reaction is:

$$2\,Al(CH_3)_3 + 3\,H_2O \longrightarrow Al_2O_3 + 3\,CH_4 \qquad (1.7)$$
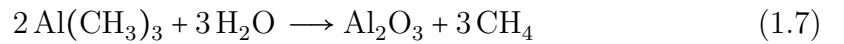
Al_2O_3 is widely used in the semiconductor industry as a high-k dielectric (8-10), and ALD of Al_2O_3 result in films with low concentrations of impurities. ALD of Al_2O_3 is also used on certain III-V semiconductor substrates due to having a cleaning effect on these substrates. This cleaning reportedly results in the reduction or removal of native oxides of the III-V semiconductor [41–47].

1.3.7 Titanium Oxide

Titanium dioxide (TiO_2) has emerged as a key area of interest for photoelectrochemical cells (PEC). It has been shown to protect the photo-absorbing substrate, from oxidation when placed in an aqueous environment, as it provides conductive, pin-hole free, smooth layers [48].

TiO_2 was first deposited by ALD in the early 90's by Lakomaa $et\ al.$ [49] and Ritala $et\ al.$ [50], using $TiCl_4$ and H_2O as reactants. The reaction takes place over a wide temperature range, as expected with the use of $TiCl_4$ as a reactant because it has high reactivity towards water and hydroxyl groups. The idealised mechanism is given by equations 1.8 and 1.9:

$$n(-OH) + TiCl_4 \longrightarrow (-O-)_n TiCl_{4-n} + nHCL \tag{1.8}$$

$$(-O-)_n TiCl_{4-n} + (4-n)H_2O \longrightarrow (-O-)_n Ti(OH)_{4-n} + (4-n)HCl \tag{1.9}$$
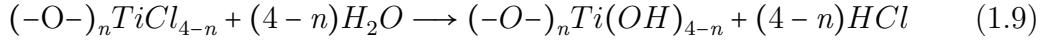
with n = 1-3. In the first half reaction $TiCl_4$ is introduced on the OH terminated surface, where it reacts very easily with the Ti bonding to the O, releasing a hydrochloric acid.

However, this is the idealised reaction. In reality the growth mechanism is more complicated than this. Species may exist in different configurations and will have alternative reaction mechanism.

On the surface of TiO_2, hydroxyl groups are either terminal or bridging between two cations. The terminal hydroxyls can be either adjacent with hydrogen bond interaction or isolated [51]. The amphoteric nature of the TiO_2 is due to the different chemical behaviour of the terminal and bridging hydroxyls [52]. Bridging groups are polarized by the cations and are thus acidic

whereas terminal hydroxyls are more basic. Instead of reacting with $TiCl_4$, surface hydroxyls can condensate with each other [51]:

$$Ti(OH) - O - Ti(OH) \longrightarrow Ti(-O-)_2Ti + H_2O \qquad (1.10)$$

$$2 - Ti(OH) \longrightarrow -Ti - O + -Ti + H_2O \qquad (1.11)$$
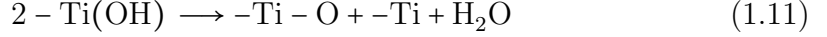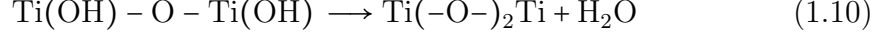
Reaction 1.10 states that if the hydroxyls are adjacent, the oxygen will be coordinated to two cations. However, if the hydroxyls are isolated (reaction 1.11 then the oxygen is coordinated bonded to only one cation, leaving the reaction unsaturated [51]. Reaction 1.10 is more favourable than reaction 1.11 at lower temperatures because hydrogen-bonded hydroxyls are more prone to dehydroxylation compared to isolated hydroxyls. In the ideal case it is assumed that $TiCl_4$ only reacts with hydroxyl groups but it can also react with oxygen bridges:

$$Ti(-O-)_2Ti + TiCl_4 \longrightarrow Ti(Cl)-O-Ti(TiCl_3) \qquad (1.12)$$
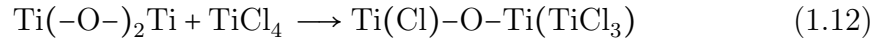
The growth mechanism becomes further complicated due to the possibility of the adsorption of HCl on the TiO_2 surface. [53]:

$$Ti-OH + HCl \leftrightarrow Ti(H_2O)-Cl \leftrightarrow Ti-Cl + H_2O \qquad (1.13)$$

$$Ti(-O)_2Ti + HCl \leftrightarrow Ti(OH)-O-Ti-Cl \qquad (1.14)$$
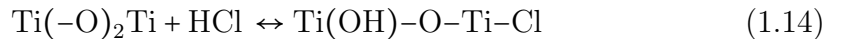
Due to these complications the real growth mechanism consists of competitive simultaneous reactions. When the $TiCl_4$ is pulsed, the hydroxyl groups can react with $TiCl_4$ (equation 1.8), or with the HCl (equation 1.13 and oxygen bridges with $TiCl_4$ (equation 1.12) or with HCl (equation 1.14). Only reactions 1.8 and 1.12

result in film growth. Equations 1.13 and 1.14 and the effects of dehydroxylation have to be taken into account.

$TiCl_4$ is a very versatile precursor, providing high quality films over a wide temperature range [50, 54, 55]. However, as HCl is released as a by-product, it is necessary for other possible Ti precursors to be tested, which do not have corrosive by-products, which will cause damage to the metal parts of the ALD kit. A number of other precursors have been investigated such as titanium tetraiodide TiI_4 [56–61], titanium methoxide $Ti(OMe)_4$ [62], titanium ethoxide $Ti(O(CH_3)_2)_4$ [63–67], Ti isopropoxide (TTIP)($Ti(OCH(CH_3)_2)_4$) [31, 68–73], and Tetrakis(dimethylamido titanium (TDMAT)($Ti(N(CH_3)_2)_4$) [74–78]. Only TTIP and TDMAT will be discussed in further detail as these are two of the most used precursors.

TTIP: TTIP is a widely used precursor that can deposit high quality TiO_2 [77, 79]. TTIP is widely used because of its good growth and desirable electrical properties of deposited materials, however does require relatively high temperature or a plasma to grow. The two possible growth mechanisms [32] of TiO_2 using TTIP is given by the following equations 1.15 and 1.16 or equations 1.17 and 1.18

$$n\text{--OH} + \text{Ti}(\text{OCH}_2\text{CH}_3) \longrightarrow (\text{--O--})_n\text{Ti}(\text{OCH}_2\text{CH}_3)_{4-n} + n\text{CH}_3\text{CH}_2\text{OH} \quad (1.15)$$

$$(\text{--O--})_n\text{Ti}(\text{OCH}_2\text{CH}_3)_{4-n} + (4\text{-}n)\text{H}_2\text{O} \longrightarrow (\text{--O--})_n\text{Ti}(\text{OH})_{4-n} + (4\text{-}n)\text{CH}_3\text{CH}_2\text{OH}$$
$$(1.16)$$
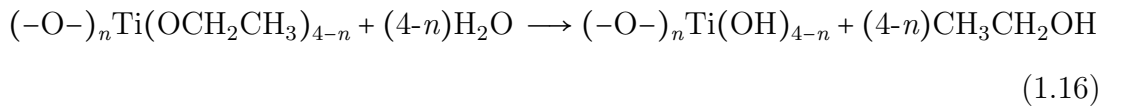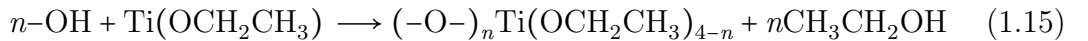
in which -OH is a surface hydroxyl and n=1-3. The ethanol may be dehydrated after its formation. The other mechanism:

$$\text{Ti}(\text{OCH}_2\text{CH}_3)_4 \longrightarrow \text{Ti}(\text{OCH}_2\text{CH}_3)_4\,(\text{cads}) \qquad (1.17)$$

$$\text{Ti}(\text{OCH}_2\text{CH}_3)_4\,(\text{cads}) + 2\,\text{H}_2\text{O} \longrightarrow \text{TiO}_2 + \text{Ch}_3\text{CH}_2\text{OH} \qquad (1.18)$$
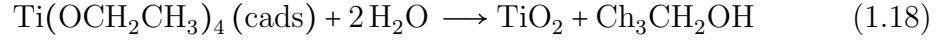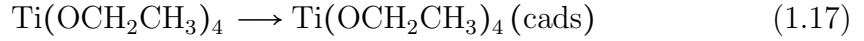
describes a TTIP molecule being chemisorbed (where cads represent chemisorbed species), with TiO_2 being formed when the H_2O pulse reacts with the molecule breaking the ligands, which are purged away.

TTIP (with H_2O as the co-reactant) has a low growth rate, in the region of 0.15 - 0.2 nm per cycle and an ALD window between 190-250°C [31, 69, 77], with steric hindrance and kinetic limitation suggested as the main reason for the low growth rate [31].

TDMAT: TDMAT has a higher reactivity than TTIP at lower temperatures, however some issues can arise at higher temperatures as TDMAT starts to decompose at 250°C [74]. TDMAT grows high quality pin-hole free, and highly conformal TiO_2 films, with good electrical properties [74, 77]. The growth rate of TiO_2 using TDMAT is generally between 0.04 - 0.06 nm/cycle [74, 76, 78].

The growth mechanism of TiO_2 using TDMAT and water can be described by the two half reactions, 1.19 and 1.20 [80].

$$n\text{--OH} + \text{Ti}(\text{N}(\text{CH}_3)_4 \longrightarrow (\text{--O--})_n\text{Ti}(\text{N}(\text{CH}_3)_{4-n} + n\text{NH}(\text{CH}_3)_2 \qquad (1.19)$$

$$(\text{--O--})_n\text{Ti}(\text{N}(\text{CH}_3)_{4-n} + (4\text{-}n)\text{H}_2\text{O} \longrightarrow (\text{--O--})_n\text{Ti}(\text{OH})_{4-n} + (4\text{-}n)\text{NH}(\text{CH}_3)_2$$
$$(1.20)$$
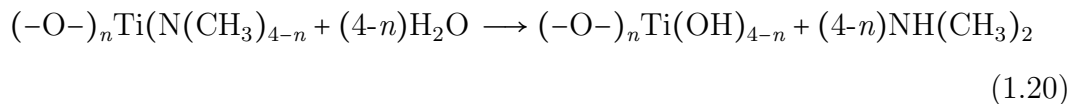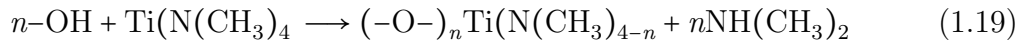
1.3.8 Titanium Dioxide Composite Materials

The electrical properties of any material are largely determined by the chemical nature of the bonds, the atomic arrangement, the physical dimensions (for nanomaterials), and the energy gap, including any defects in the energy gap. The chemical composition of TiO_2 can be altered by doping or creating a composite material.

Doping is defined as the introduction of impurities into the material, where the dopant has a different number of outer electrons than the element it is replacing. In the case of having more electrons in the outer shell, an unbonded "free" electron is able to move and add to the current, thereby creating an n-type doping. If the dopant has fewer outer electrons, a hole is created, which is free to move (other bonded electrons can move into the hole, this can be thought of as the hole moving) [81]. A TiO_2 composite is a combination of one or more materials (metal, metal oxide, metal sulphide, etc.) with TiO_2. This can be produced by various methods, most commonly for ALD by nanolaminates, which are created by alternating cycles of the two materials. It can also be grown in ALD by co-pulsing two metal precursors, however this method needs to be calibrated with strictly controlled process parameters.

Nanolaminates have been studied a great deal, as these nanolaminates can produce some novel materials. Commonly, the laminates create clearly identifiable sublayers, even for layers with thicknesses around 1 nm. However more mixed phase systems can be produced as well [82]. Figure 1.5 introduces the term supercycle, used in ALD when growing these alternative layers. A supercycle is shown as the combination of the starting material and the doping layer. The level of doping changes based on the ratio of n : dopant.

TiO_2 composites and doped TiO_2 have been extensively studied with many different materials, using many various methods, being summarised in [83]. In general, the materials formed improved the optical properties [81, 84],
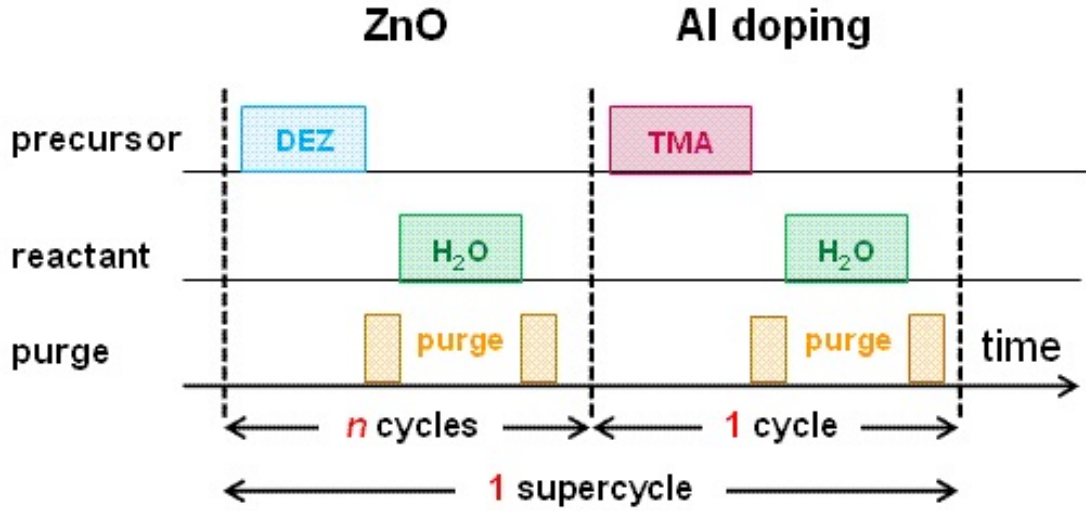
Figure 1.5: Illustration of an ALD supercycle, where DEZ is Diethylzinc, a precursor used for the deposition of ZnO.

photocatalytic behaviour [85–88], or in electronics to create a high-k, low leakage material for capacitors [89–92].

In the case of TiO_2, since the lower edge of the conduction band (CB) is made up of Ti^{4+} 3d orbitals, replacing Ti^{4+} with a different cation should have a large effect on the CB structure. Similarly, the valence bands (VB) upper edge consists of O^{2-} 2p orbitals and replacing the O^{2-} anion by a different anion will affect the energy of the VB [81]. Another factor to take into account is the atomic radius of the dopant, if the size is much bigger or smaller, this may introduce lattice distortion. An example of how the conduction and valence bands can change is illustrated in figure 1.6.
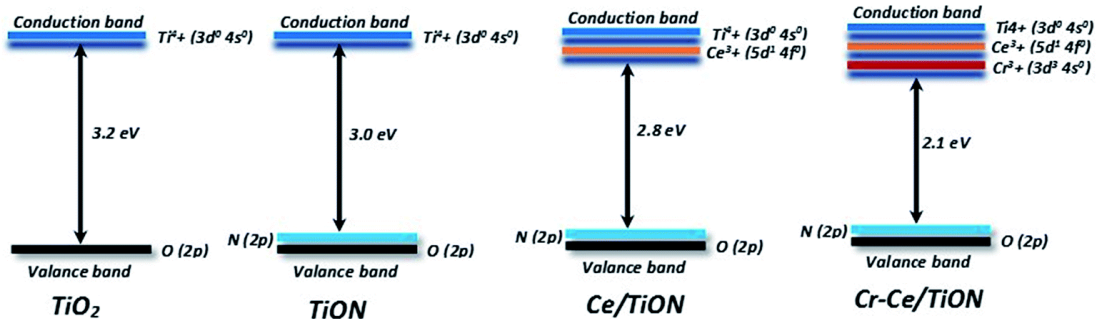
Figure 1.6: Illustration of how other elements can affect the band structure of TiO_2. Adapted from [93], Ce is cerium and Cr is chromium.

35

1.4   MOS Capacitor Physics

1.4.1   MOS Structure

The Metal-Oxide-Semiconductor system has been extensively studied because of its role in MOSFET operation. The ideal structure is shown in figure 1.7, where d is the thickness of the insulator (i.e. the oxide). V is the applied voltage where a positive V, denotes the gate metal positively biased with respect to the semiconductor.
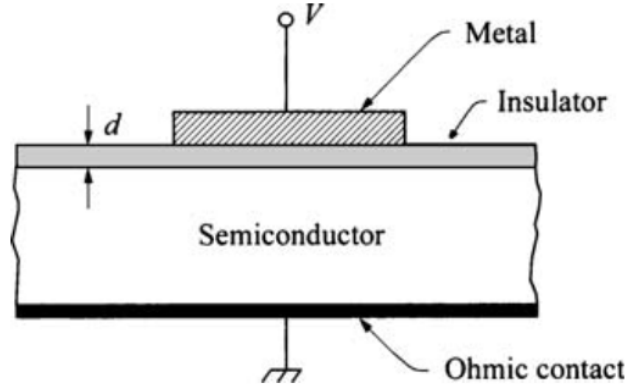
Figure 1.7: Metal Oxide Semiconductor in its simplest form. Adapted from [94].

In an ideal MOS structure, no charges exist in the oxide under any biasing conditions, and the oxide is perfectly insulating, i.e. there is no carrier transport through the film. Shown in figure 1.8 is the energy-band diagram for the ideal MOS structure, where difference in work function of the gate metal and the semiconductor is zero. Where χ and χ_i are the electron affinities for the semiconductor and the insulator (oxide) respectively and ψ_{Bn}, ψ_{Bp}, ϕ_n, ϕ_p, are the Fermi potentials of the semiconductor (where ψ is in relation to the midgap and ϕ in relation to the band edges) and ϕ_m is the metal work function. E_C, E_V, E_F, and E_i are the energy levels related to the conduction band, valence band, Fermi level, and intrinsic Fermi level, and E_g is the band gap. The Fermi level is moved from the intrinsic level due to the level of doping. With n-type doping moving the Fermi level closer to the conduction band, and p-type doping

moving the Fermi level closer to the valence band.
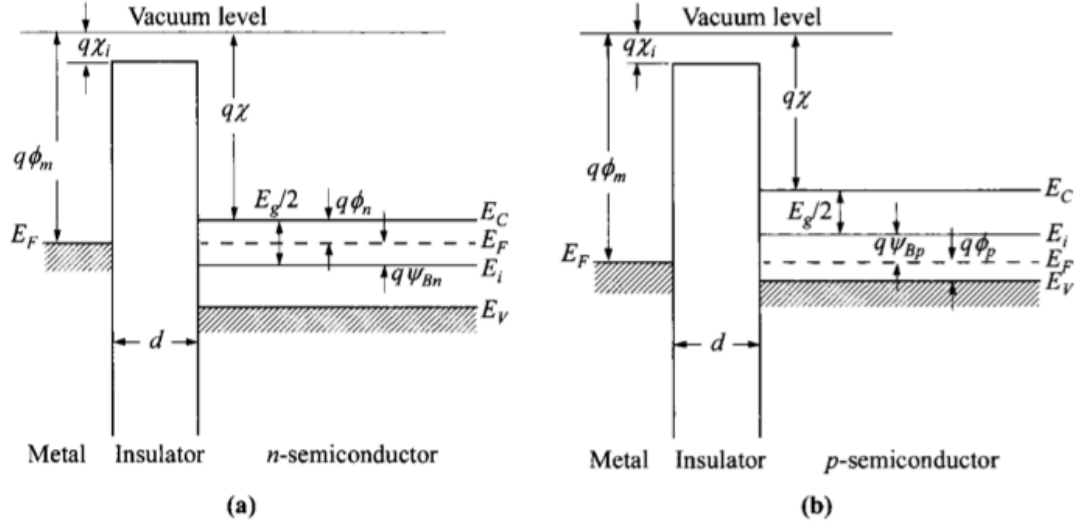
Figure 1.8: Ideal Metal Oxide Semiconductor energy band structure for a) NMOS and b) PMOS. Adapted from [94].

Figure 1.9 shows the operation of the MOS device under different bias operating conditions. Consider the PMOS device, when a negative voltage is placed on the gate, the valence-band E_v bends up towards the Fermi level (which in the ideal case remains flat, due to no current flow). Since carrier concentration is dependent on the energy difference between the Fermi level and the valence band, the band bending causes the material at the surface to be more heavily p-type, i.e. there is an accumulation of holes, the majority carrier. When a positive voltage is applied, the opposite happens, the bands bend downward, and the material becomes depleted of holes at the surface until the point where the bands bend so much that the surface ends up with more electrons (minority carriers) than holes, i.e. the surface has inverted and this is the inversion case. NMOS is the same but opposite, when a positive voltage is applied on the gate, the device goes into accumulation (of electrons), and with a negative gate voltage, the device goes into depletion/inversion.

In reality there are a number of other conditions to account for. Firstly, there will be a difference in work function of the metal and semiconductor, giving rise to band bending at zero applied voltage. There is therefore a particular voltage

37
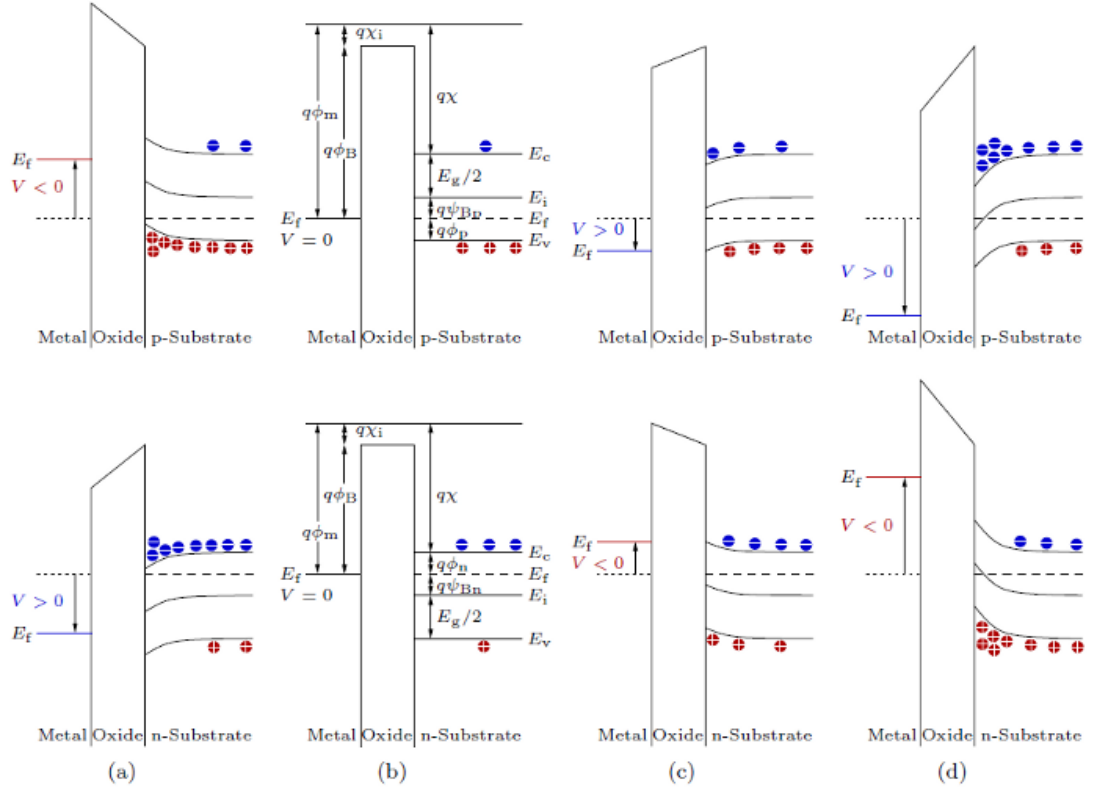
Figure 1.9: Energy band diagram showing the operation of the MOS device under different biases, a) accumulation, b) flat-band, c) depletion and d) inversion.

that when applied will bend the bands back to the point where they are flat. This voltage is the called the flat-band voltage V_{FB}. There is also the case where charges will exist in the oxide, there can be fixed charge in the oxide, fixed charge at the semiconductor-oxide interface, interface charge which varies with the applied ac voltage and mobile charge in the oxide, which all have an effect on device performance. Finally, there will also be leakage current through the oxide, which will play a large role on device performance.

1.4.2 Leakage Current

Leakage current has always been an important factor in microelectronics, and a lot of research has gone into the reduction of leakage current [95–97]. However, for the application of water splitting with PECs, and more generally photovoltaics, a higher leakage current is desirable. Recently *Chen et. al.* has

shown that very thin TiO$_2$ deposited by atomic layer deposition (ALD) can be used to protect silicon photoactive layers in PECs for water splitting [14]. The TiO$_2$ layers used were approximately 2 nm thick. In this thickness range, current should be dominated by direct tunnelling. However, in thicker layers, other current mechanisms will dominate. Figure 1.10 illustrates the different types of current flow in a MOS structure [98, 99].
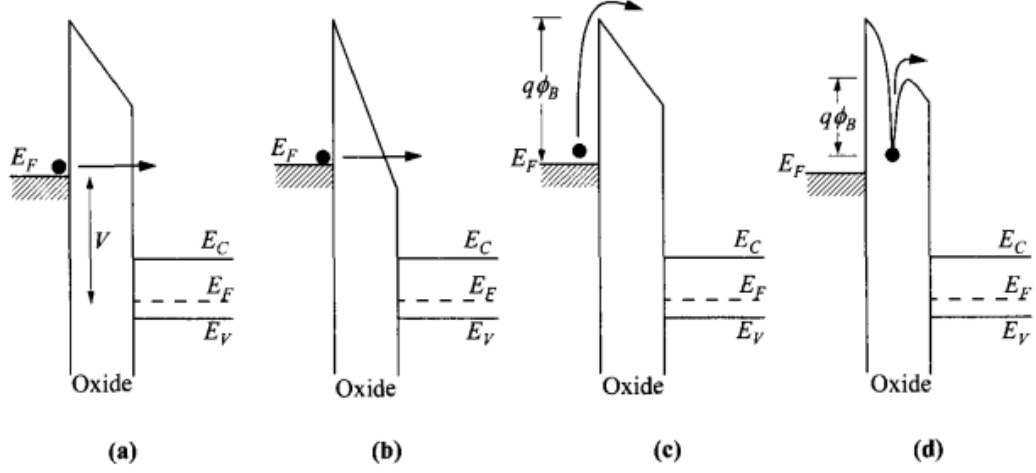
Figure 1.10: Illustration of the different types of current mechanism through a MOS capacitor. a) direct tunnelling, b) Fowler Nordheim tunnelling, c) thermionic emission and d) Frenkel-Poole emission. Adapted from [94].

Direct Tunnelling As mentioned above when the thickness of the oxide gets very thin, less than 5 nm, the current mechanism is dominated by direct tunnelling. The schematic energy band diagram for direct tunnelling is shown in figure 1.10. The expression of the direct tunnelling current density is

$$J_{DT} = \frac{A \cdot E_d^2}{[1 - (\Phi_b - q \cdot V_d)^{1/2}]^2} \cdot \exp\left[-\frac{B}{E_d} \cdot \frac{\Phi_b^{3/2} - (\Phi_b - q \cdot V_d)^{3/2}}{\Phi_b^{3/2}} \right]$$
$$\cdot \left[1 - \exp\left(-\frac{3}{2} \cdot \frac{B}{E_d} \cdot \frac{\Phi_b^{1/2} - (\Phi_b - q \cdot V_d)^{1/2}}{\Phi_b^{3/2}} \cdot E_{FS} \right) \right] \quad (1.21)$$

$$A = \frac{q^3 m_0}{8\pi h m_{ox} \Phi_b} \quad (1.22)$$

$$B = \frac{4\sqrt{2m_{ox}\Phi_b^3}}{3\hbar q} \qquad (1.23)$$

J is the current density, m_0 is the free electron mass, q is the electronic charge, Φ_b is the Schottky barrier height, E_d is the electric field across the dielectric, V_d is the voltage across the dielectric, E_FS is the semiconductor Fermi level, k is the Boltzmann's constant, h is Planck's constant.

Schottky or Thermionic Emission Thermionic emission takes place if the electrons can obtain sufficient energy, by thermal activation, to overcome the energy barrier between either the metal-oxide or oxide-semiconductor (depending on the gate bias and type of MOS) and get into the conduction band of the oxide. Thermionic emission is one of the most often observed conduction mechanisms in dielectric films, especially as the temperature increases. The Thermionic emission expression is:

$$J_{TE} = A^* T^2 \cdot \exp\left[-\frac{q}{kT}\left(\Phi_b - \sqrt{\frac{qE_d}{4\pi\varepsilon_0 k_d}}\right) \right] \qquad (1.24)$$

$$A^* = \frac{4\pi q k^2 m^*}{h^3} = \frac{120 m^*}{m_0} \qquad (1.25)$$

A^* is the effective Richardson constant, m^* is the effective electron mass in dielectric, T is the absolute temperature, ε_0 is the permittivity in vacuum and k_d is the dynamic dielectric constant.

Fowler Nordheim Tunnelling As can be seen from figure 1.10 FN tunnelling is similar to direct tunnelling. However, the electron does not see the full thickness of the dielectric. FN tunnelling occurs when the applied electric field is great enough so that the electron wave function may penetrate through to the conduction band of the dielectric. This mechanism only occurs at very high electric fields, larger than about 6 MV/cm for wide band insulators but can occur at measurable levels for smaller band gap insulators or insulators with a small band offset, which causes the triangular barrier at the top of the

dielectric [98, 99]. The expression for FN tunnelling is given by:

$$J_{FN} = A \cdot E_d^2 \cdot \exp\left[-\frac{B}{E_d} \right] \tag{1.26}$$

$$A = \frac{q^3 m_0}{8\pi h m_{ox} \Phi_b} \tag{1.27}$$

$$B = \frac{4\sqrt{2 m_{ox} \Phi_b^3}}{3\hbar q} \tag{1.28}$$

where m_{ox} is the effective mass in the dielectric film.

Poole-Frenkel Emission PF emission is a mechanism very closely related to thermionic emission, where thermally excited electrons jump to the conduction band of the dielectric. However, in PF the electrons are jumping from traps within the dielectric into the conduction band. An electrons Coulomb potential energy in a trap can be reduced by applying an electric field. The reduction in potential energy may increase the probability of an electron being thermally excited out of the trap. The expression for PF current is given by:

$$J_{PF} = E_d \cdot \exp\left[-\frac{q}{kT}\left(\Phi_b - \sqrt{\frac{qE_d}{\pi\varepsilon_0 k_d}} \right) \right] \tag{1.29}$$

Both PF and thermionic emission have been observed as the dominant conduction mechanism in TiO_2 [100]. There has also been some work to try and control the current in TiO_2. However, as TiO_2 was one of the contenders for a high-k dielectric in microelectronics, most research involved trying to reduce the leakage. For the application of water splitting the opposite is necessary, that of reducing the resistance that the dielectric, and therefore possibly being able to increase the thickness of the TiO_2 which should help with the long-term stability of the photoelectrochemical cell.

1.4.3 Capacitance

The capacitance (C), measured in Farads (F), is the amount of charge (Q) stored per unit voltage (V),

$$Q = CV \tag{1.30}$$

In the case of a parallel plate capacitor, the charge on the plates with vacuum (or air) between them is related to ε_0, the permittivity of free space. The use of a different insulating material can be used to increase the amount of charge stored on the plates by a factor or ε_r or κ, the relative permittivity or dielectric constant. The capacitance can then be calculated from:

$$C = \frac{\kappa \varepsilon_0 A}{t_{ox}} \tag{1.31}$$

where A is the area of the capacitor and t_{ox} is the thickness of the oxide or insulating material between the plates. The permittivity of a material is a measure of the resistance of the material to the formation of an electric field. Effectively it is a measure of the ability of a material to polarise in the presence of an electric field, which effectively reduces any field set up in it. The value of the permittivity in general varies over frequency of the ac component of the electric field, due to the different polarisation mechanisms, such as orientational, ionic and electronic. The ratio of the permittivity of a material to the permittivity of vacuum is the dielectric constant:

$$\kappa = \frac{\varepsilon}{\varepsilon_0} \tag{1.32}$$

In an ideal situation where the plates are infinitely large and planar symmetry is assumed, the electric field can be calculated using Gauss's law,

$$\Phi = \oint_A \vec{E} \, d\vec{A} = \frac{q_e}{e_0} \tag{1.33}$$

where Φ is the electric flux, $\vec{E}$ is the electric field vector, $d\vec{A}$ is the surface vector and q_e is the enclosed electric charge. The electric field is related to the electric flux by

$$E = \frac{\Phi}{A} = \frac{q_e}{A\varepsilon_0} = \frac{CV}{A\varepsilon_0} \tag{1.34}$$

The electric field is also related to the applied voltage and distance between the plates by

$$E = \frac{V}{d} \tag{1.35}$$

Rearranging and solving for C gives the capacitance of a parallel plate capacitor with a vacuum

$$C = \frac{\varepsilon_0 A}{d} \tag{1.36}$$

and including κ for other materials,

$$C = \frac{\kappa \varepsilon_0 A}{d} \tag{1.37}$$

For a MOS capacitor, the theory is similar, but the capacitance is a measure of the charge induced in the surface of the semiconductor due to the applied bias. In an ideal case, all of the induced charge on the gate metal will result in a corresponding surface charge density (Q_s) at the surface of the semiconductor.

An example of a capacitance voltage curve for a PMOS capacitor is shown in figure 1.11. In the accumulation region, the capacitance is independent of the measurement frequency because the charges are responding as majority carriers, which can respond to frequencies in excess of 1 GHz (majority carrier relaxation time = $\varepsilon_0 \varepsilon_s / \sigma$), therefore the measured capacitance approximates to the oxide capacitance. Coming out of the accumulation region the hole density at the surface decreases, meaning the differential capacitance is no longer large compared to the oxide capacitance, therefore the measured capacitance decreases overall. In the depletion region, the surface has no charge, creating a depletion region,

which makes the measured capacitance smaller. When the surface inverts, and electron density exceeds the bulk charge, relatively low frequencies, which the minority carrier generation can follow, see a large differential capacitance again. Meaning the measured capacitance again approximates the oxide capacitance. At high frequencies minority carrier generation cannot follow the applied ac voltage, therefore the measured capacitance only sees the oxide and a large depletion capacitance.
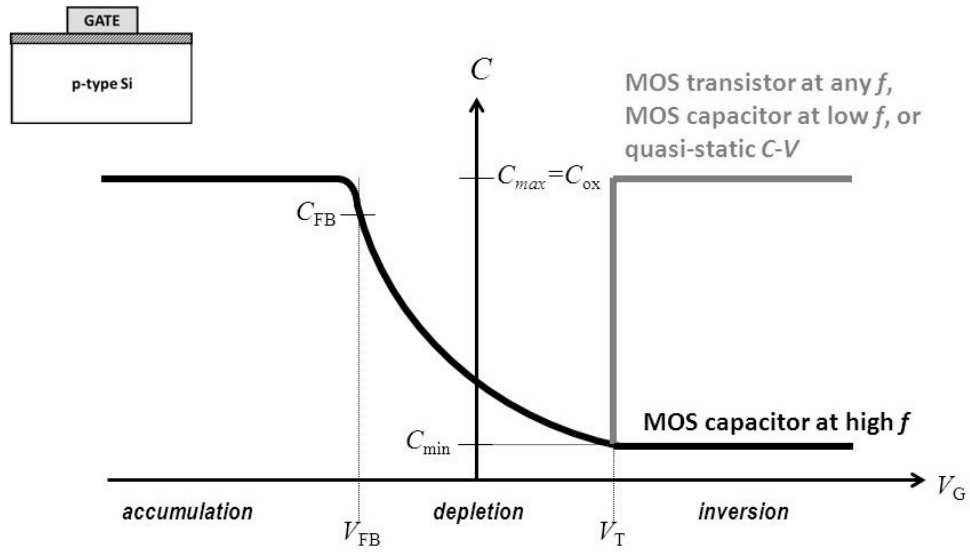
Figure 1.11: PMOS capacitance characteristics. Note this is an approximation, the change in C with V is a smooth function.

1.4.4   Non-Ideal MOS Capacitor

In the real world there are a number of non-ideal characteristics that must be accounted for, such as trapped charge in the oxide, fixed charges in the oxide and interface states. Figure 1.12 illustrates these charges. The issue of mobile charge will not be addressed as it is rare in ALD grown films.

1.4.4.1   Fixed Oxide Charge

Fixed oxide charge can exist both at the oxide/semiconductor interface and in the bulk of the oxide. This charge does not change with applied bias. The fixed
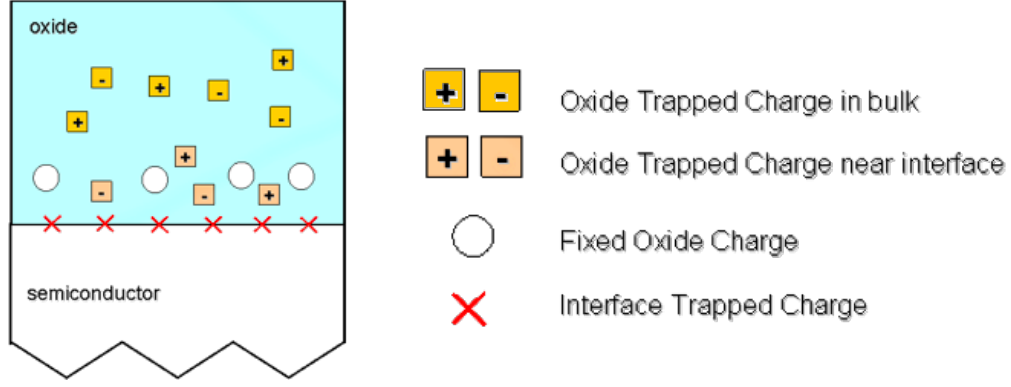
Figure 1.12: The different charges that can be present in a non-ideal MOS capacitor [101].

charge causes a parallel shift along the voltage axis of the CV. The direction of shift is dependent on the polarity of the fixed charge. If the fixed charge is negative, the CV will be shifted in the positive direction as the applied bias has to compensate for the inherent oxide charge and vice versa for positive fixed charge. The flat band voltage will also obviously be offset, the flat band voltage can be calculated from

$$V_{FB} = \phi_{ms} - \frac{Q_{fixed}}{C_o x}$$ (1.38)

where Q$_{fixed}$ is the fixed charge and C$_{ox}$ is the oxide capacitance.

1.4.4.2 Oxide Trapped Charge - Hysteresis

The dielectric layer may contain charge trapping sites due to non-stoichiometry in the film. While the device is being measured electrons or holes may become trapped or de-trapped in these sites.

Trapping or de-trapping is dependent on the electric field across the device. With a high enough electric field electrons or holes are able to tunnel in or out of the oxide from the gate or semiconductor respectively. This appears again as a shift of the CV but a shift that is reversible, resulting in a hysteresis in the CV if the voltage is swept in both directions. However, some traps can be more

permanent, for example if holes are trapped and cannot be refilled with electrons for the bias range and temperature examined, then this shift is permanent. An example of the effect is demonstrated in figure 1.13.
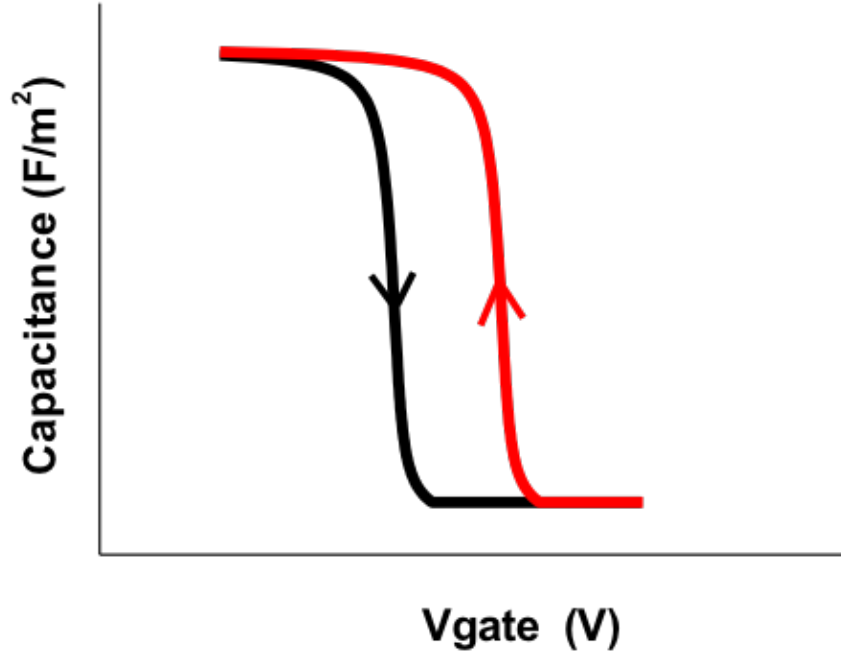
Figure 1.13: Effect of hole injection and trapping from the substrate on the ideal CV curve.

1.4.4.3 Interfacial Layer

There will often be an SiO_2 interface layer between the dielectric and the silicon substrate. The SiO_2 will add a capacitor in series with the oxide capacitance and the semiconductor capacitance, and will generally result in interface states, due to stoichiometry and/or dangling bonds. The interface state density (D_{it}) of the MOS capacitor refers to the density of electrically active interface charge due to the structural defects between the semiconductor substrate and the dielectric. Each of the defects will have an associated energy level. The defects, whose energy levels are located in the band gap of the semiconductor, will have a large influence of the MOS performance. Depending on where the defect energy level exists in the bandgap along with its response time and density, the interface

states may cause stretch out or frequency dependent bumps if the capture and emission of charge from the interface defect to the semiconductor conduction or valence band can follow the ac signal frequency. Figure 1.14 demonstrates these effects. The stretch out of the CV response is due to the filling or emptying of the interface defects with the slowly varying dc bias on the gate and the charge state depending on whether the defects are donor or acceptor in nature. Depending on the ac signal frequency and the device temperature, some of the interface states may respond with the measurement period of the ac signal. This results in dispersion of the CV profile as a function of the ac frequency, displaying frequency dependent peaks in the CV profile where the effect of the interface states is to act as a parallel capacitance to the semiconductor differential capacitance as the interface defects contribute a rate of change of surface charge with respect to the surface potential.
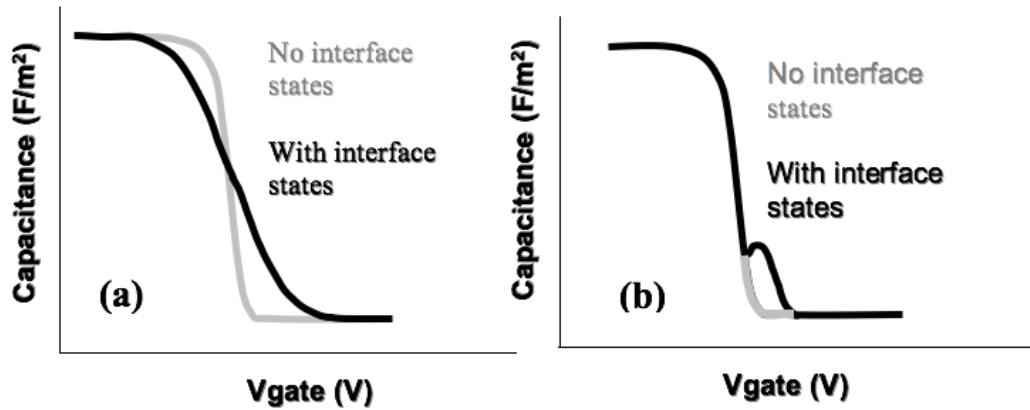
Figure 1.14: Effect of an interface state density on the ideal CV curve (a) stretch out (b) frequency dependent 'bumps' where the storage of the interface charge adds to the measured capacitance.

1.5 Thin Film Characterisation

ALD grown films are usually characterised by ex-situ techniques. For example, transmission electron microscopy (TEM), x-ray reflectometry (XRR), x-ray diffraction (XRD) and x-ray photoelectron spectroscopy (XPS), among others.

These techniques can provide information on the films properties such as thickness, microstructure, electrical resistivity and atomic composition.

Recently a number of techniques for in-situ monitoring have become available. One such technique is in-situ spectroscopic ellipsometry (SE), which can be used to monitor film thickness and growth rate per cycle, which are two of the most relevant parameters during an ALD process.

1.5.1 Spectroscopic Ellipsometry

In general growth rate is determined by growing a thickness series, measuring the thickness of each film with a technique such as TEM, and dividing each thickness by the number of ALD cycles used. The reason for the multiple samples of different thickness is due to the fact that the growth rate is not necessarily constant, nucleation effects can either inhibit or accelerate film growth [102, 103]. It can take a considerable number of cycles before the growth per cycle is constant giving a linear growth rate. The nucleation growth of ultrathin films can obviously have a large effect on the final thickness film.

Spectroscopic ellipsometry (SE) enables the ex-situ or in-situ characterisation of thickness and refractive constant of thin films. SE measures the change in polarization of light after interacting with a material. SE monitors the electric field behaviours in space and time, a known polarization (usually linearly polarized light) is incident on a sample, when reflected the sample changes the polarization to elliptical as shown in figure 1.15

This change in polarization is represented as a phase shift, Δ and amplitude ratio, Ψ and the change is dependent on the materials thickness and optical constants. SE is a technique that has been widely used in literature [24, 28, 102, 105–110]

In situ SE during ALD

Principle Of Ellipsometry

Φ_0 : angle of incidence
Δ: relative phase change
Ψ: relative amplitude change

s-plane stands perpendicularly to the plane of incidence
p-plane stands parallel to the plane of incidence
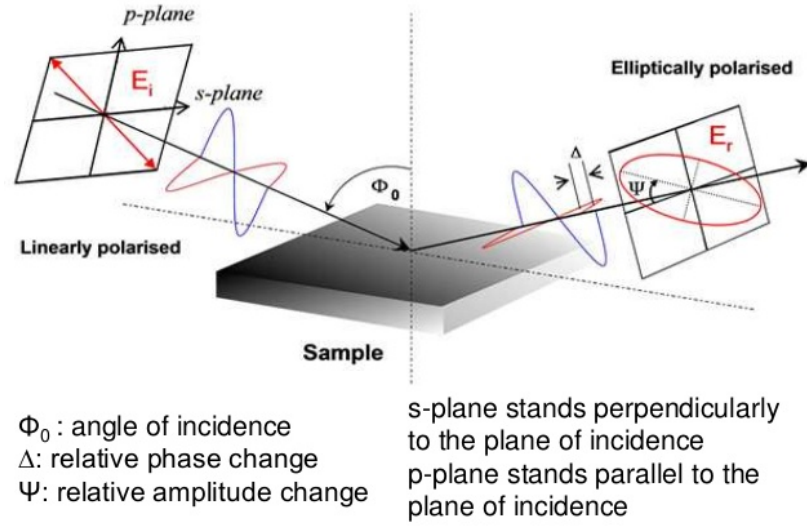
Figure 1.15: Simplified SE operation. The linear polarized incident light, reflects and changes polarization, where it is then will be collected by the detector for analysis [104].

As the nucleation of the films plays such a large role in the growth, it is important to understand this regime. The process of understanding this portion of the film growth process, is obviously easier when in-situ methods are used during this period of the ALD process. In-situ techniques can be used for the determination of ALD saturation curves, investigation of the half-cycles and the measurement of optical, structural and even electrical properties.

The high sensitivity, and non-destructive nature of SE makes it well suited to ALD growth studies of ultra-thin films, with sub-monolayer growth per cycle.

There are a number of factors to be considered when employing in-situ SE during ALD. One of which is optical access on the reactor for the light source and detector. This is achieved by having the reactor equipped with optical access ports. Windows, generally made of fused silica, which have a transparency range of 180-2000 nm, are well suited for these ports. Also, the angle of incidence of the light beam is generally restricted to a fixed angle for in-situ measurements in contrast to multi-angled ex-situ systems [24].

49

1.5.2 Transmission Electron Microscopy

Transmission electron microscopy is a technique that transmits a beam of electrons through an ultra-thin sample. An image is formed based on the interaction of the electrons with the different parts of the sample. For example, if two materials are present, more electrons will transmit through one material, than the other. The resulting image will have a distinct contrast showing the two different materials. An example is shown in figure 5.1
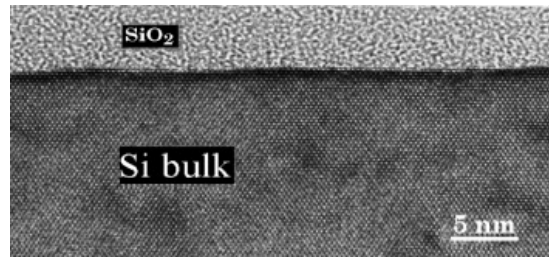
Figure 1.16: An example TEM image.

A conventional TEM system consists of an electron beam source, the sample stage, an objective lends, and an optical detector, as illustrated in figure 1.17. All TEM measurements and analysis presented in this thesis was carried out internally by collaborators.
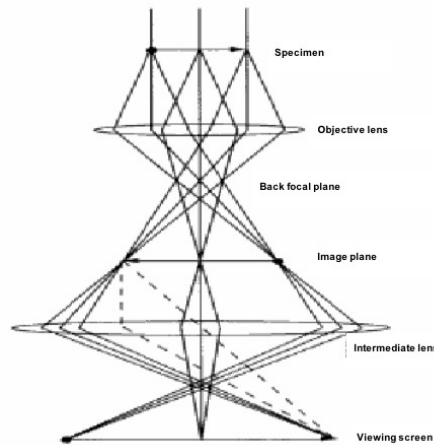
Figure 1.17: Schematic of a TEM system. Adapted from [111].

1.5.3 X-Ray Photoelectron Spectroscopy

X-ray photoelectron spectroscopy (XPS), is a technique used to investigate the chemical composition of surfaces. The technique is based on the photoelectric effect, demonstrated in figure 1.18. The surface of the sample is irradiated with a beam of x-rays. The detector then measures the kinetic energy (KE) and number of photoelectrons, which have a kinetic energy of:

$$KE = hv - BE - \Phi_{spec} \tag{1.39}$$

where hv is the photon energy of the x-rays, BE is the electron binding energy and Φ_{Spec} is the spectrometer work function. Peaks in the XPS spectra show the electrons from the different orbital shells and can be used to obtain the elemental and chemical state of the material by comparing to known binding energy values. All XPS measurements and analysis presented in this thesis was carried out externally by collaborators, Fathima Laffir (University of Limerick), Conor McGeough (Dublin City University) and Olivia Hendricks (Stanford University)

1.5.4 Cyclic Voltammetry - Ferri/Ferrocyanide

Cyclic voltammetry is a very useful electroanalytical measurement used to study electroactive species. Cyclic voltammetry monitors the redox behaviour of a chemical species. For this thesis the chemical redox couple used is ferri/ferrocyanide. This experiment measures the redox behaviour of the chemical species within a wide potential range. For this measurement there are three electrodes. The working electrode, used in this thesis is the photoanode of the PEC. In addition, there is a counter electrode and a reference electrode (usually Ag/AgCl). The potential is applied across the working and reference electrode and the current measured between the working and counter electrode.
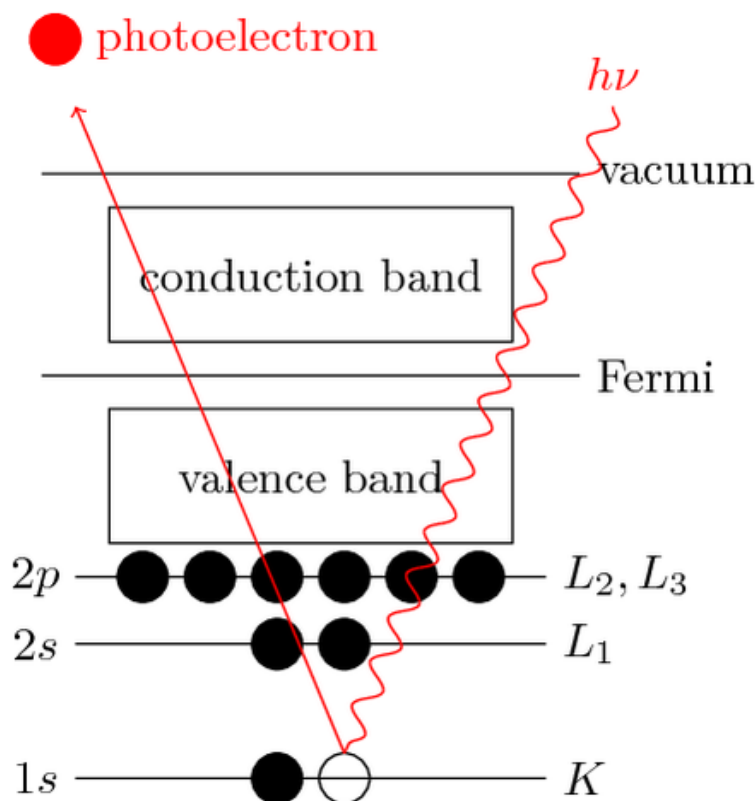
Figure 1.18: Basic principle of XPS.

The voltage is scanned from 0 to a positive value, to a negative value and back to 0. When the potential is scanned in the positive direction, and is sufficiently positive to oxidize $Fe(CN)_6^{-4}$, the anodic current is due to the electrode process

$$Fe(CN)_6^{-4} \longrightarrow Fe(CN)_6^{-3} + e^- \tag{1.40}$$
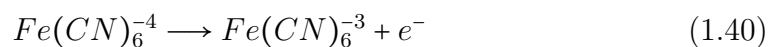
The electrode acts as an oxidant and the oxidation current increases to a maximum, before dropping off as the concentration of $Fe(CN)_6^{-4}$ at the electrode surface depletes. When the potential reverses, the current is still anodic until it is sufficiently strongly reductant, then the $Fe(CN)_6^{-3}$ which has been forming will be reduced by:

$$Fe(CN)_6^{-3} + e^- \longrightarrow Fe(CN)_6^{-4} \tag{1.41}$$
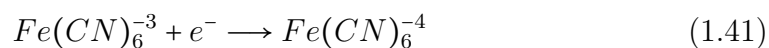
resulting in a cathodic current, which also reaches a maximum before dropping

off as the $Fe(CN)_6^{-3}$ is consumed.

For this thesis, as the cyclic voltammetry measurements are used as an initial test before more comprehensive PEC tests are done, the value of interest is the potential between the anodic and cathodic peaks, which indicates series resistance in the photoanode, which in this case is related to the series resistance of the TiO_2 layer.

Bibliography

[1] Lewis, N. S. *Science* **2007,** *315,* 798-801.

[2] Allen, J. *Acc. Chem. Res* **1995,** *28,* 141–145.

[3] Turner, J. A. *Science* **1999,** *285,* 687-689.

[4] Fujishima, A.; Honda, K. *Nature* **1972,** *238,* 37-38.

[5] Walter, M. G.; Warren, E. L.; McKone, J. R.; Boettcher, S. W.; Mi, Q.; Santori, E. A.; Lewis, N. S. *Chemical Reviews* **2010,** *110,* 6446–6473.

[6] Ni, M.; Leung, M. K.; Leung, D. Y.; Sumathy, K. *Renewable and Sustainable Energy Reviews* **2007,** *11,* 401–425.

[7] Grätzel, M. *Nature* **2001,** *414,* 338–344.

[8] Lewis, N. S. *Nature* **2001,** *414,* 589–590.

[9] Lewis, N. S.; Nocera, D. G. *Proceedings of the National Academy of Sciences* **2006,** *103,* 15729–15735.

[10] Scheuermann, A. G.; Prange, J. D.; Gunji, M.; Chidsey, C. E.; McIntyre, P. C. *Energy & Environmental Science* **2013,** *6,* 2487–2496.

[11] Lewis, N. S.; Crabtree, G. "Basic research needs for solar energy utilization: report of the basic energy sciences workshop on solar energy utilization", 2005.

[12] Kenney, M. J.; Gong, M.; Li, Y.; Wu, J. Z.; Feng, J.; Lanza, M.; Dai, H. *Science* **2013,** *342,* 836–840.

[13] Mei, B.; Seger, B.; Pedersen, T.; Malizia, M.; Hansen, O.; Chorkendorff, I.; Vesborg, P. C. *The Journal of Physical Chemistry Letters* **2014,** *5,* 1948–1952.

[14] Chen, Y. W.; Prange, J. D.; Dühnen, S.; Park, Y.; Gunji, M.; Chidsey, C. E.; McIntyre, P. C. *Nature Materials* **2011,** *10,* 539–544.

[15] Hu, S.; Shaner, M. R.; Beardslee, J. A.; Lichterman, M.; Brunschwig, B. S.; Lewis, N. S. *Science* **2014,** *344,* 1005–1009.

[16] Mei, B. *et al. The Journal of Physical Chemistry Letters* **2014,** *5,* 3456–3461.

[17] Scheuermann, A.; Lawrence, J.; Kemp, K.; Ito, T.; Walsh, A.; Chidsey, C.; Hurley, P.; McIntyre, P. *Nature Materials* **2015,** *15,* 1.

[18] Kohl, P. A.; Frank, S. N.; Bard, A. J. *Journal of the Electrochemical Society* **1977,** *124,* 225–229.

[19] Howe, A. T.; Hawkins, R. T.; Fleisch, T. H. *Journal of The Electrochemical Society* **1986,** *133,* 1369–1375.

[20] Fan, F. R. F.; Keil, R. G.; Bard, A. J. *Journal of the American Chemical Society* **1983,** *105,* 220–224.

[21] Leskela, M.; Ritala, M. *Thin Solid Films* **2002,** *409,* 138 - 146.

[22] Ritala, M.; Leskelä, M. Chapter 2 - Atomic layer deposition. In *Handbook of Thin Films*; Nalwa, H. S., Ed.; Academic Press: Burlington, 2002.

[23] George, S. M.; Ott, A. W.; Klaus, J. W. *The Journal of Physical Chemistry* **1996,** *100,* 13121-13131.

[24] Langereis, E.; Heil, S. B. S.; Knoops, H. C. M.; Keuning, W.; van de Sanden, M. C. M.; Kessels, W. M. M. *Journal of Physics D: Applied Physics* **2009,** *42,* 073001.

[25] George, S. M. *Chemical Reviews* **2010,** *110,* 111-131.

[26] Van Hemmen, J.; Heil, S.; Klootwijk, J.; Roozeboom, F.; Hodson, C.; Van de Sanden, M.; Kessels, W. *Journal of The Electrochemical Society* **2007,** *154,* G165–G169.

[27] Heil, S.; Kudlacek, P.; Langereis, E.; Engeln, R.; van de Sanden, M.; Kessels, W. *Applied Physics Letters* **2006,** *89,* 131505.

[28] Profijt, H.; Potts, S.; Van de Sanden, M.; Kessels, W. *Journal of Vacuum Science & Technology A* **2011,** *29,* 050801.

[29] Puurunen, R. *Chemical Vapor Deposition* **2003,** *9,* 249–257.

[30] Puurunen, R. L. *Journal of Applied Physics* **2005,** *97,* 121301.

[31] Ritala, M.; Leskela, M.; Niinisto, L.; Haussalo, P. *Chemistry of Materials* **1993,** *5,* 1174-1181.

[32] Ponraj, J. S.; Attolini, G.; Bosi, M. *Critical Reviews in Solid State and Materials Sciences* **2013,** *38,* 203–233.

[33] Saleem, M. R.; Ali, R.; Khan, M. B.; Honkanen, S.; Turunen, J. *Frontiers in Materials* **2014,** *1,* 18.

[34] Higashi, G.; Fleming, C. *Applied Physics Letters* **1989,** *55,* 1963–1965.

[35] Soto, C.; Tysoe, W. *Journal of Vacuum Science & Technology A* **1991,** *9,* 2686–2695.

[36] Goldstein, D. N.; McCormick, J. A.; George, S. M. *The Journal of Physical Chemistry C* **2008,** *112,* 19530–19539.

[37] Kim, J.; Kwon, D.; Chakrabarti, K.; Lee, C.; Oh, K.; Lee, J. *Journal of Applied Physics* **2002,** *92,* 6739–6742.

[38] Groner, M.; Fabreguette, F.; Elam, J.; George, S. *Chemistry of Materials* **2004,** *16,* 639–645.

[39] Ott, A.; Klaus, J.; Johnson, J.; George, S. *Thin Solid Films* **1997,** *292,* 135–144.

[40] Dillon, A.; Ott, A.; Way, J.; George, S. *Surface Science* **1995,** *322,* 230–242.

[41] Ye, P. *et al. Applied Physics Letters* **2003,** *83,* 180–182.

[42] Huang, M.; Chang, Y.; Chang, C.; Lee, Y.; Chang, P.; Kwo, J.; Wu, T.; Hong, M. *Applied Physics Letters* **2005,** *87,* 252104.

[43] Hinkle, C. *et al. Applied Physics Letters* **2008,** *92,* 071901.

[44] Hou, C.; Chen, M.; Chang, C.; Wu, T.; Chiang, C. *Electrochemical and Solid-State Letters* **2008,** *11,* D60–D63.

[45] Shahrjerdi, D.; Garcia-Gutierrez, D.; Tutuc, E.; Banerjee, S. *Applied Physics Letters* **2008,** *92,* 223501.

[46] Hou, C.; Chen, M.; Chang, C.; Wu, T.; Chiang, C.; Luo, J. *Journal of The Electrochemical Society* **2008,** *155,* G180–G183.

[47] Cheng, C.-W.; Hennessy, J.; Antoniadis, D.; Fitzgerald, E. A. *Applied Physics Letters* **2009,** *95,* 082106.

[48] Chen, Y. W.; Prange, J. D.; Dühnen, S.; Park, Y.; Gunji, M.; Chidsey, C. E.; McIntyre, P. C. *Nature Materials* **2011,** *10,* 539–544.

[49] Lakomaa, E.-L.; Haukka, S.; Suntola, T. *Applied Surface Science* **1992,** *60,* 742–748.

[50] Ritala, M.; Leskelä, M.; Nykänen, E.; Soininen, P.; Niinistö, L. *Thin Solid Films* **1993,** *225,* 288–295.

[51] Mathieu, M. V.; Primet, M.; Pichat, P. *The Journal of Physical Chemistry* **1971,** *75,* 1221–1226.

[52] Parfitt, G. *Progress in Surface and Membrane Science* **1976,** *11,* 181–226.

[53] Parfitt, G.; Ramsbotham, J.; Rochester, C. *Transactions of the Faraday Society* **1971,** *67,* 3100–3109.

[54] Kumagai, H.; Matsumoto, M.; Toyoda, K.; Obara, M.; Suzuki, M. *Thin Solid Films* **1995,** *263,* 47–53.

[55] Aarik, J.; Aidla, A.; Uustare, T.; Sammelselg, V. *Journal of Crystal Growth* **1995,** *148,* 268–275.

[56] Aarik, J.; Aidla, A.; Uustare, T.; Kukli, K.; Sammelselg, V.; Ritala, M.; Leskelä, M. *Applied Surface Science* **2002,** *193,* 277–286.

[57] Kukli, K.; Ritala, M.; Schuisky, M.; Leskelä, M.; Sajavaara, T.; Keinonen, J.; Uustare, T.; Hårsta, A. *Chemical Vapor Deposition* **2000,** *6,* 303–310.

[58] Kukli, K.; Aidla, A.; Aarik, J.; Schuisky, M.; Hårsta, A.; Ritala, M.; Leskelä, M. *Langmuir* **2000,** *16,* 8122–8128.

[59] Schuisky, M.; Hårsta, A.; Aidla, A.; Kukli, K.; Kiisler, A.-A.; Aarik, J. *Journal of the Electrochemical Society* **2000,** *147,* 3319–3325.

[60] Schuisky, M.; Kukli, K.; Aarik, J.; Lu, J.; Hårsta, A. *Journal of Crystal Growth* **2002,** *235,* 293–299.

[61] Schuisky, M.; Aarik, J.; Kukli, K.; Aidla, A.; Hårsta, A. *Langmuir* **2001,** *17,* 5508–5512.

[62] Pore, V.; Rahtu, A.; Leskelä, M.; Ritala, M.; Sajavaara, T.; Keinonen, J. *Chemical Vapor Deposition* **2004,** *10,* 143–148.

[63] Aarik, J.; Aidla, A.; Sammelselg, V.; Uustare, T.; Ritala, M.; Leskelä, M. *Thin Solid Films* **2000,** *370,* 163–172.

[64] Aarik, J.; Karlis, J.; Mändar, H.; Uustare, T.; Sammelselg, V. *Applied Surface Science* **2001,** *181,* 339–348.

[65] Rahtu, A.; Kukli, K.; Ritala, M. *Chemistry of Materials* **2001,** *13,* 817–823.

[66] Kim, I.-D.; Tuller, H. L.; Kim, H.-S.; Park, J.-S. *Applied Physics Letters* **2004,** *85,* 4705–4707.

[67] Ritala, M.; Leskela, M.; Rauhala, E. *Chemistry of Materials* **1994,** *6,* 556–561.

[68] Döring, H.; Hashimoto, K.; Fujishima, A. *Berichte der Bunsengesellschaft für Physikalische Chemie* **1992,** *96,* 620–622.

[69] Aarik, J.; Aidla, A.; Uustare, T.; Ritala, M.; Leskelä, M. *Applied Surface Science* **2000,** *161,* 385–395.

[70] Rahtu, A.; Ritala, M. *Chemical Vapor Deposition* **2002,** *8,* 21–28.

[71] Shin, H.; Jeong, D.-K.; Lee, J.; Sung, M. M.; Kim, J. *Advanced Materials* **2004,** *16,* 1197–1200.

[72] Jeong, D.; Park, N.; Jung, S.-H.; Jung, W. G.; Shin, H.; Lee, J.; Kim, J. *Materials Science Forum* **2004,** *449,* 1165–1168.

[73] Jeong, D.; Lee, J.; Shin, H.; Lee, J.; Kim, J.; Sung, M. *Journal of the Korean Physical Society* **2004,** *45,* 1249–1252.

[74] Reiners, M.; Xu, K.; Aslam, N.; Devi, A.; Waser, R.; Hoffmann-Eifert, S. *Chemistry of Materials* **2013,** *25,* 2934–2943.

[75] Maeng, W.; Kim, H. *Electrochemical and Solid-State Letters* **2006,** *9,* G191–G194.

[76] Pheamhom, R.; Sunwoo, C.; Kim, D.-H. *Journal of Vacuum Science and Technology A: Vacuum, Surfaces and Films* **2006,** *24,* 1535-1539.

[77] Xie, Q.; Jiang, Y.-L.; Detavernier, C.; Deduytsche, D.; Van Meirhaeghe, R. L.; Ru, G.-P.; Li, B.-Z.; Qu, X.-P. *Journal of Applied Physics* **2007,** *102,* 8.

[78] Xie, Q.; Musschoot, J.; Deduytsche, D.; Van Meirhaeghe, R.; Detavernier, C.; Van Den Berghe, S.; Jiang, Y.-L.; Ru, G.-P.; Li, B.-Z.; Qu, X.-P. *Journal of the Electrochemical Society* **2008,** *155,* H688-H692.

[79] Lim, J. W.; Yun, S. J.; Lee, J. H. *Electrochemical and Solid-State Letters* **2004,** *7,* F73–F76.

[80] Zhuiykov, S.; Akbari, M. K.; Hai, Z.; Xue, C.; Xu, H.; Hyde, L. *Materials & Design* **2017,** *120,* 99–108.

[81] Roose, B.; Pathak, S.; Steiner, U. *Chem. Soc. Rev.* **2015,** *44,* 8326-8349.

[82] Pinna, N.; Knez, M. *Atomic Layer Deposition of Nanostructured Materials;* John Wiley & Sons: 2012.

[83] Dahl, M.; Liu, Y.; Yin, Y. *Chemical Reviews* **2014,** *114,* 9853–9889.

[84] Wong, W.; Malati, M. *Solar Energy* **1986,** *36,* 163–168.

[85] Pore, V.; Heikkilä, M.; Ritala, M.; Leskelä, M.; Areva, S. *Journal of Photochemistry and Photobiology A: Chemistry* **2006,** *177,* 68–75.

[86] Kim, S. K.; Choi, G. J.; Kim, J. H.; Hwang, C. S. *Chemistry of Materials* **2008,** *20,* 3723–3727.

[87] Kim, S.; Hwang, S.-J.; Choi, W. *The Journal of Physical Chemistry B* **2005,** *109,* 24260–24267.

[88] Liang, Y.-C.; Wang, C.-C.; Kei, C.-C.; Hsueh, Y.-C.; Cho, W.-H.; Perng, T.-P. *The Journal of Physical Chemistry C* **2011,** *115,* 9498–9502.

[89] Kim, S. K.; Choi, G.-J.; Lee, S. Y.; Seo, M.; Lee, S. W.; Han, J. H.; Ahn, H.-S.; Han, S.; Hwang, C. S. *Advanced Materials* **2008,** *20,* 1429–1435.

[90] Mikhelashvili, V.; Eisenstein, G.; Thangadurai, P.; Kaplan, W.; Brener, R.; Saguy, C. *Journal of Applied Physics* **2008,** *103,* 114106.

[91] Triyoso, D.; Hegde, R.; Wang, X.-D.; Stoker, M.; Rai, R.; Ramon, M.; White, B.; Tobin, P. *Journal of the Electrochemical Society* **2006,** *153,* G834–G839.

[92] Popovici, M. *et al. Journal of The Electrochemical Society* **2009,** *156,* G145–G151.

[93] Rashid, S.; Gondal, M.; Hameed, A.; Aslam, M.; Dastageer, M.; Yamani, Z.; Anjum, D. *RSC Advances* **2015,** *5,* 32323-32332.

[94] Sze, S. M.; Ng, K. K. *Physics of semiconductor devices;* John Wiley & Sons: 2006.

[95] Kim, N. S.; Austin, T.; Baauw, D.; Mudge, T.; Flautner, K.; Hu, J. S.; Irwin, M. J.; Kandemir, M.; Narayanan, V. *Computer* **2003,** *36,* 68–75.

[96] Robertson, J. *The European Physical Journal Applied Physics* **2004,** *28,* 265–291.

[97] Wong, H.; Iwai, H. *Microelectronic Engineering* **2006,** *83,* 1867–1904.

[98] Bentarzi, H. Review of Transport Mechanism in Thin Oxides of MOS Devices. In *Transport in Metal-Oxide-Semiconductor Structures: Mobile Ions Effects on the Oxide Properties*; Springer Berlin Heidelberg: Berlin, Heidelberg, 2011.

[99] Chiu, F.-C. "A review on conduction mechanisms in dielectric films", 2014.

[100] Tinoco, J.; Estrada, M.; Iñiguez, B.; Cerdeira, A. *Microelectronics Reliability* **2008,** *48,* 370–381.

[101] Long, R. D. *A Study of the Electronic and Structural Properties of the High-kIn0. 53Ga0. 47As System,* Thesis, NUI, 2011.

[102] Knoops, H.; Mackus, A.; Donders, M.; Van De Sanden, M.; Notten, P.; Kessels, W. *Electrochemical and Solid-State Letters* **2009,** *12,* G34–G36.

[103] Kirsch, P. *et al. Journal of Applied Physics* **2006,** *99,* 023508.

[104] http://www.tcd.ie/Physics/Surfaces/ellipsometry2.php, "Principals of Ellipsometry", 2012.

[105] Tompkins, H.; Irene, E. A. *Handbook of ellipsometry;* William Andrew: 2005.

[106] Fujiwara, H. *Spectroscopic ellipsometry: principles and applications;* John Wiley & Sons: 2007.

[107] Van Bui, H.; Groenland, A.; Aarnink, A.; Wolters, R.; Schmitz, J.; Kovalgin, A. *Journal of the Electrochemical Society* **2011,** *158,* H214–H220.

[108] Langereis, E.; Knoops, H.; Mackus, A.; Roozeboom, F.; Van de Sanden, M.; Kessels, W. *Journal of Applied Physics* **2007,** *102,* 083517.

[109] Heil, S.; Langereis, E.; Kemmeren, A.; Roozeboom, F.; Van De Sanden, M.; Kessels, W. *Journal of Vacuum Science & Technology A: Vacuum, Surfaces, and Films* **2005,** *23,* L5–L8.

[110] Isidorsson, J.; Giebels, I.; Arwin, H.; Griessen, R. *Physical Review B* **2003,** *68,* 115112.

[111] Fultz, B.; Howe, J. M. *Transmission electron microscopy and diffractometry of materials;* Springer Science & Business Media: 2012.

Chapter 2

An investigation of barrier heights for Indium-Tin-Oxide/Silicon Contacts over n and p type silicon

2.1 Introduction

Indium doped tin oxide (ITO) is a transparent conducting oxide (TCO), that currently has a range of applications in solar energy devices. As silicon is one of the most widely used materials for solar applications [1, 2] the ITO on Si contact is important to characterise and understand. One specific case where the ITO on silicon can have applications is as the anode structure in photoelectrochemical cells for water splitting [3], where photons generate electron-holes at the Si anode which is immersed in water, and the surfaces holes recombine with electrons from the catalyst/silicon interface to drive the oxidation of the water [4]. In photoelectrochemical cells, oxidation of the silicon surface occurs if the silicon surface is unprotected which in turn reduces the hole transport and the photovoltage generated by the cell. Without surface protection the cells typically fail in less than half an hour due to oxidation [5]. There are a number of potential protective layers such as TiO_2 [5], ITO [6, 7], among others such as Ni, Ru, NiO_x and etc. [8]. These protective layers also need to be transparent to the wavelengths of light that are absorbed by the silicon and also be able to conduct holes to the interface with the water. As ITO is transparent and conducting, thick ITO layers can be deposited without compromising the hole transport and this could potentially improve long term stability of the cell when compared to insulating protective layers such as TiO_2. However, stability issues have been reported for ITO under values of pH that are not close to neutral [9].

It has also recently been discussed that the use of a shallow (0.45 μm) p+ region in a p+n Si anode with a TiO_2 protection layer results in an enhanced cell performance for water splitting applications [10]. The p+ surface layer maintains a high concentration of holes at the silicon/oxide surface of the anode structure, which yields high values of photo-voltage (>600 mV) as well as removing the dependence of the photo-voltage on the thickness of the TiO_2 layer used to protect

the silicon anode. The protective layer needs to minimize the resistance to hole transport, therefore an ohmic contact between ITO and p+ silicon would be ideal.

According to the Schottky–Mott model, the barrier height equals the difference between metal work function and electron affinity of semiconductor χ (for Si $\chi = 4.05$ eV). The work function of ITO has been reported in the range of 4.4 to 5.53 eV, when deposited by electron beam evaporation and measured experimentally by ultraviolet and x-ray photoelectron spectroscopy (UPS) and (XPS) techniques [3, 11]. The objective of this work is to experimentally investigate the Schottky barrier heights of ITO formed by electron beam evaporation on moderately doped n and p type silicon (100), as well as ITO on degenerately doped p type silicon using current-voltage (I-V), and capacitance-voltage (C-V) techniques. The stoichiometry of the ITO films was also investigated using XPS.

2.2   Experimental

The resistivity of the n-type (phosphorus doped) Si(100)wafers used in this study is 1-2 ohm.cm (4.9×10^{15} cm^{-3} - 2.4×10^{15} cm^{-3}), the p-type (boron doped) resistivity is 10-20 ohm.cm (1.4×10^{15} cm^{-3} – 6.7×10^{14} cm^{-3}) and the p++-type (degenerately doped p-type, boron doping) resistivity is 0.001 - 0.005 ohm.cm (9×10^{19} cm^{-3} - 1.3×10^{19} cm^{-3}). The silicon wafers had an initial surface clean in a Semitool Spray Acid tool. Ozone, hot deionised water, NH_4OH and HF were used to remove particles, organic contaminants and metals from the wafer surface before oxidation. Using the HF and ozone together simultaneously etches and regenerates the oxide on the surface. This treatment removes a thin layer of silicon around 0.8-1.0 nm and leaves a chemical passivation oxide around 1 nm thick on the wafer surface. The ITO layers were deposited by electron-beam evaporation in a Leybold SYRUS pro710 system. The layers

thicknesses were nominally 75 nm to 85 nm. The chamber was pumped down to $< 5 \times 10^{-6}$ mbar. The evaporation was ion-assisted (argon) using Leybold's APS5000 plasma source with a discharge current of 50 A, a bias voltage of 125 V and a coil current set at 1.4 A. The APS shutter thickness trigger was set so that the first 3 nm of ITO was deposited with the shutter closed to protect the silicon surface from the plasma. The evaporation rate was set at 0.2 nm/sec requiring an e-beam gun emission current of 77 mA. The ITO Schottky diodes were defined using photolithography and lift off processing (the area ranges from 40×40 μm^2 up to 1000×1000 μm^2). Blanket layers of ITO were also formed by e-beam evaporation for the XPS analysis. The sheet resistance of the ITO films was determined as 139 $\Omega/\square$, and if the thickness is between 75 and 85 nm the resistivity is therefore 1 - 1.2 mΩ.cm.

X-ray photoelectron spectroscopy analysis was carried out on a PHI Model 500 XPS system in order to obtain the elemental composition of the ITO films. The photoelectrons were excited using a monochromated Al Kα source (hu = 1486.6 eV) at a power of 49.9 W with a spot size diameter of 200 μm. Peak fitting analysis was carried out using analyser peak fitting software. Relative sensitivity factors (O 1s = 0.71, In 3d5/2 = 4.36 and Sn 3d5/2 = 4.73) for the calculation of the elemental composition percentages from the acquired spectra were taken from published values [12].

Finally, some ferri/ferrocyanide (FFC) measurements were completed to determine preliminary photoelectrochemical cell performance. To enable this experiment 5 nm of Ir was deposited as an oxidation catalyst. The p+ Si samples were measured in the dark while the p+n Si sample were measured under AM 1.5. The Air Mass is the path length which light takes through the atmosphere normalised to the shortest possible path length (that is, when the sun is directly overhead). The Air Mass quantifies the reduction in the power of light as it passes through the atmosphere and is absorbed by air and dust. The air mass coefficient is commonly used to characterise the performance of solar

cells under standardised conditions.

2.3   Results and Discussion

Figure 2.1 shows the O 1s (a), Sn 3d (b) and In 3d (c) core level XPS spectra
for a deposited ITO film. The areas associated with the O 1s, Sn 3d5/2 and In
3d5/2 peaks were used in conjunction with the relative sensitivity factors [12] for
each core level in order to calculate the relative elemental composition of the film
giving a film composition of ~47% O, ~47% In and ~6% Sn within the sampling
depth of XPS.
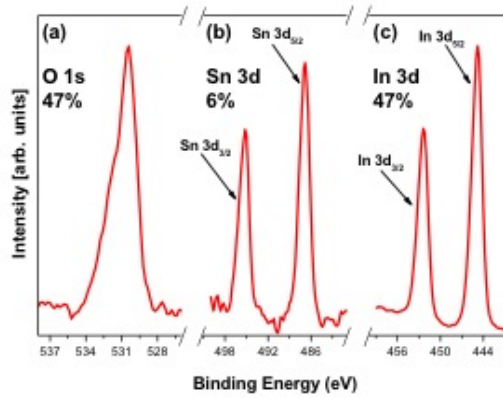
Figure 2.1: XPS results for the ITO film with A) O 1s, B) Sn 3d, and C) In 3d
core level spectra showing the relative elemental composition of the film.

The Schottky barrier heights were measured using two methods:
current-voltage (I-V) and capacitance-voltage (C-V). I-V characteristics of
ITO/n-type Si, ITO/p-type Si and ITO/p++-type Si are shown in figures 2.2A,
2.2B and 2.2C respectively. These measurements were performed on diodes of
different areas across different sites on the sample. The I-V characteristics
showed excellent uniformity across the sample area measured.   The I-V
responses show in figure 2.2 are a representative plot of the current measured
from multiple sites. The current in figure 2.2A for the ITO/n-Si sample exhibits
typical Schottky behaviour. Figure 2.2B for the ITO/p-Si sample shows some
asymmetry between the 'on' and 'off' currents, which is typical of a low

Schottky barrier. This is more prominent for is even the ITO/p+ Si in figure 2.2C where the response is almost linear.
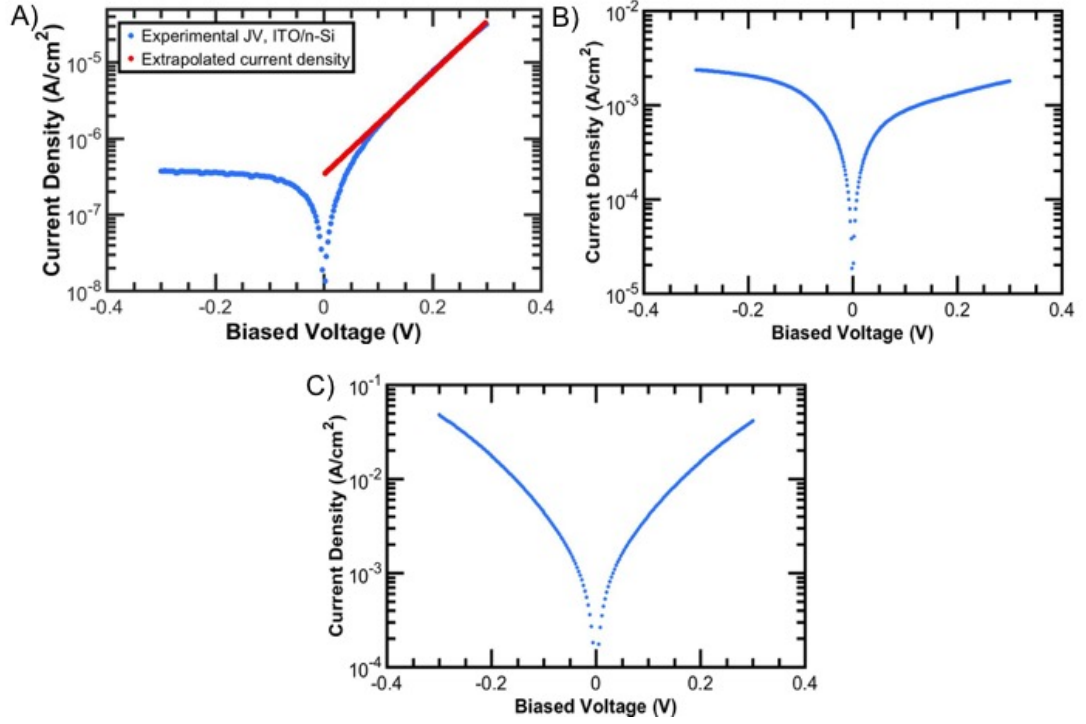
Figure 2.2: A) I-V results of ITO/n-type Si (1-2 ohm.cm) on a log scale showing the experimental results and the extrapolation to acquire J_o. Sample was measured at room temperature on a 50 μm square pad. The sample shows a strong asymmetry, giving a good ratio of 'on' current to 'off' current.

For thermionic emission and V>3kT/q, the general diode equations are:

$$J = J_0 exp\left(\frac{qV}{nkT}\right) \tag{2.1}$$

$$\phi_{Bn} = \frac{kT}{q}ln\left(\frac{A^{\star\star}T^2}{J_0}\right) \tag{2.2}$$

where ϕ_{Bn} is the barrier height, J_0 is the saturation current density, k is Boltzmann's constant, n is the ideality factor and $A^{\star\star}$ (=110 Acm^{-2} K^{-2}) is the effective Richardson coefficient [13]. J_0 for the ITO/n-type Si Schottky diode is obtained from figure 2.2 as the extrapolated current density, giving a value of 3.53 x 10^{-7} A/cm^2. Using this saturation current in Equation 2.2 yields a barrier

of 0.8 eV for the ITO/n-type Si Schottky. In addition, the ideality factor (1.93) was extracted from the same curve fit. This indicates that the current is mostly dominated by the recombination of minority carriers in the space charge region. C-V measurements were performed at multiple frequencies for the ITO/n-type Si sample (figure 2.3 A). In the case of the ITO/p-type Si samples the leakage was too high to measure accurate capacitance values.
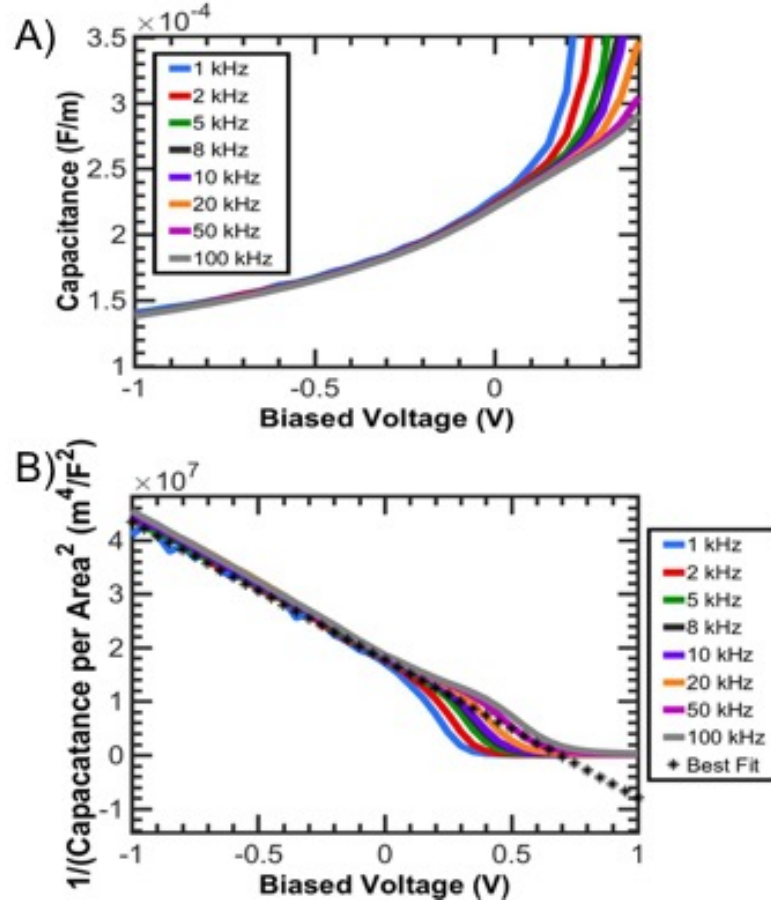
Figure 2.3: CV and $1/C^2$ plot for n-type Si. This was measured at multiple frequencies as shown at room temperature on a 50 μm square pad.

The C-V relationship for a Schottky diode is

$$\left(\frac{1}{C^2}\right) = \left(\frac{2}{\epsilon_s q N_D}\right)\left(V_{bi} - V - \frac{kT}{q}\right) \tag{2.3}$$

where ϵ_s is the permittivity of silicon, N_D is the doping, V_{bi} is the in-built voltage, which can be extracted from the intercept on the voltage axis of the $1/C^2$ plot, figure 2.3 B). From this the barrier height can be calculated using

69

equation 2.4:

$$\phi_{Bn} = V_{Bi} + V_n + \frac{kT}{q} - \Delta\phi \qquad (2.4)$$

where $V_n = kT/qln(N_c/N_D)$, where N_c is the effective density of states given by $N_c \equiv 2\left[\frac{2\pi m_n kT}{h^2}\right]^{3/2}$, and $\Delta\phi$ is the image force lowering. Figure 2.4 shows these values on an energy diagram.

ϕ_m = Work function of metal
ϕ_{Bn0} = Barrier height (without image-force lowering)
ϕ_0 = Neutral level (above E_V) of interface states
Δ = Potential across interfacial layer
χ = Electron affinity of semiconductor
ψ_{bi} = Built-in potential
δ = Thickness of interfacial layer
Q_{sc} = Space-charge density in semiconductor
Q_{ss} = Interface-trap charge
Q_M = Surface-charge density on metal
D_{it} = Interface-trap density
ε_i = Permittivity of interfacial layer (vacuum)
ε_s = Permittivity of semiconductor

Figure 2.4: Energy band diagram of metal semiconductor contact. Adapted from [13].

The slope of $1/C^2$ vs. V yields $N_D \approx 3.8\times10^{15}$ cm^{-3} (this equates to a resistivity of 1.3 Ω.cm, which is within the quoted value of the resistivity from the supplier), $V_{bi} = 0.63$ eV, and $\phi_{Bn} = 0.87$ eV. This is in good agreement with the value of 0.8 eV obtained from the analysis of the diode I-V response. Taking these two results for the barrier height for the ITO/n-type Si Schottky sample, and using

the formula below the work function of the ITO can be calculated.

$$q\phi_{Bn} = q(\phi_{ITO} - \chi) \tag{2.5}$$

i.e. the barrier height for a n-type Schottky is equal to the difference between the metal work function and the electron affinity of the semiconductor (4.05 eV for silicon [13]), however this formula does not take into account things like interface states, or surface contamination, etc. The calculated barrier height gives the ITO a work function of 4.85 – 4.92 eV, which is within the range of values given by other published approaches [3,11]. Figure 2.5 shows the energy band diagram of the system, showing the calculated barrier height and work function.
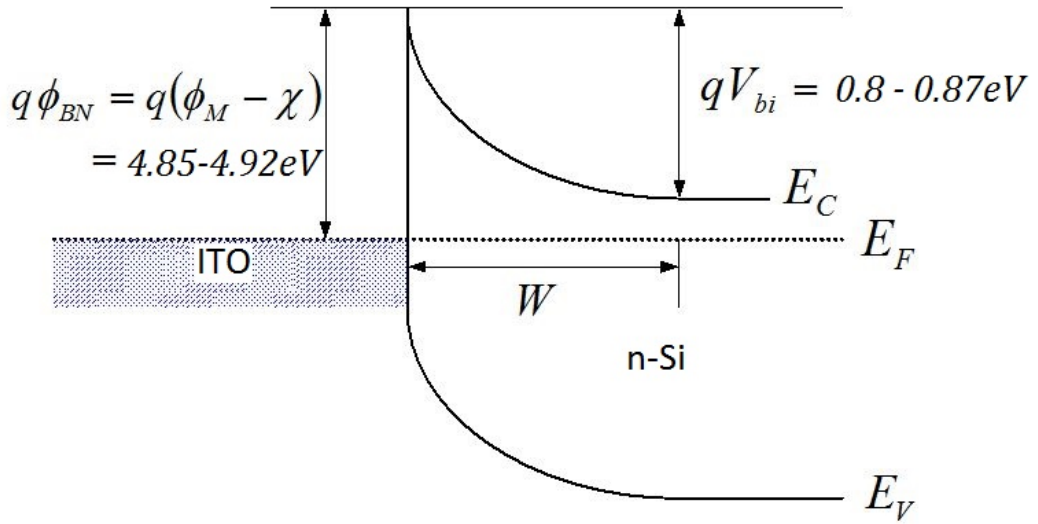
Figure 2.5: Band diagram of a Schottky diode, with band bending to illustrate the barrier. This sample is ITO on n-Si which shows a relatively large barrier.

The leakage current from the ITO/p-type Si is too high and therefore a saturation current density cannot be accurately extracted from figure 2.3. The CV measurements of the ITO/p-type Si are affected by the high current levels, even at a reduced temperature of -50°C, ruling out barrier height extraction using C-V analysis.

In an ideal system, the sum of the Schottky barrier heights of junctions

prepared on n- and p-type semiconductors equals the bandgap. This is never realised experimentally. The main deviations are due to a thin interface oxide which is typically present between the metal and the semiconductor and the presence of interface states at the metal/semiconductor interface. However, this assumption can be used to give an approximation of the barrier over p-type Si. For these experiments (taking into consideration the differences in doping concentrations) the barrier height of the ITO/p-type Si should be around 0.3 eV [3, 11]. The IV on p++-Si shown in figure 2.2 shows a diode with almost symmetrical forward and reverse currents, therefore the barrier provides very little rectifying behaviour. This could be due to high doping reducing the tunnelling distance.
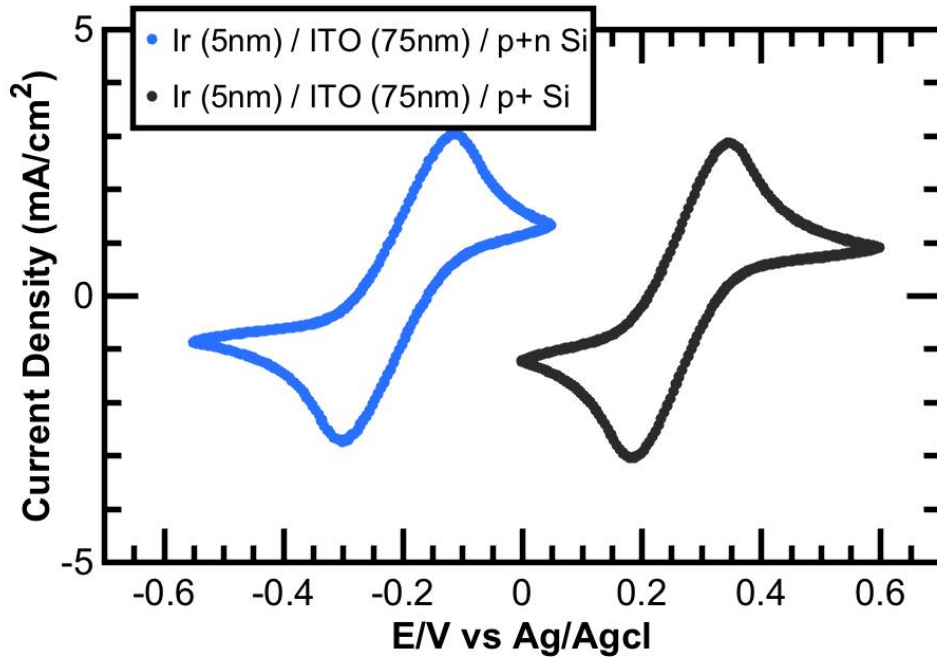
Figure 2.6: Cyclic voltammetry responses for the Ir (5 nm) / ITO (75nm) / p+n Si and Ir (5 nm) / ITO (75nm) / p+ Si structures. The photovoltage can be inferred by a comparison of the centre points of the p+ Si anode in the dark and the p+n Si anode in the light.

2.4 Cyclic Voltammetry

Ferri/ferrocyanide (FFC) cyclic voltammetry measurements are used as a benchmark test to characterise the efficiency of electronic transport across the interface of the sample to the solution. The electron transfer between the ferri/ferrocyanide solution and the metal electrodes is fast, allowing for the electronic transport across the ITO layer to be characterised [14]. Figure 2.6 shows the cyclic voltammetry response of ITO on p+ Si and on a p+n Si, measured in the photoelectrochemical cell. In the p+n structure, the peak hole surface concentration is $5 \times 10^{19} cm^{-3}$ with a junction depth of 430 nm. The n Si substrate doping is $4.9 \times 10^{15} cm^{-3}$. p+n Si has been shown to be a very strong candidate for a photoanode for water splitting cells [10] The samples have 5 nm of Ir on the ITO surface, to act as an oxygen evolution catalyst. The p+ Si sample is measured in the dark, while the p+n Si sample is measured under 1.5 AM.
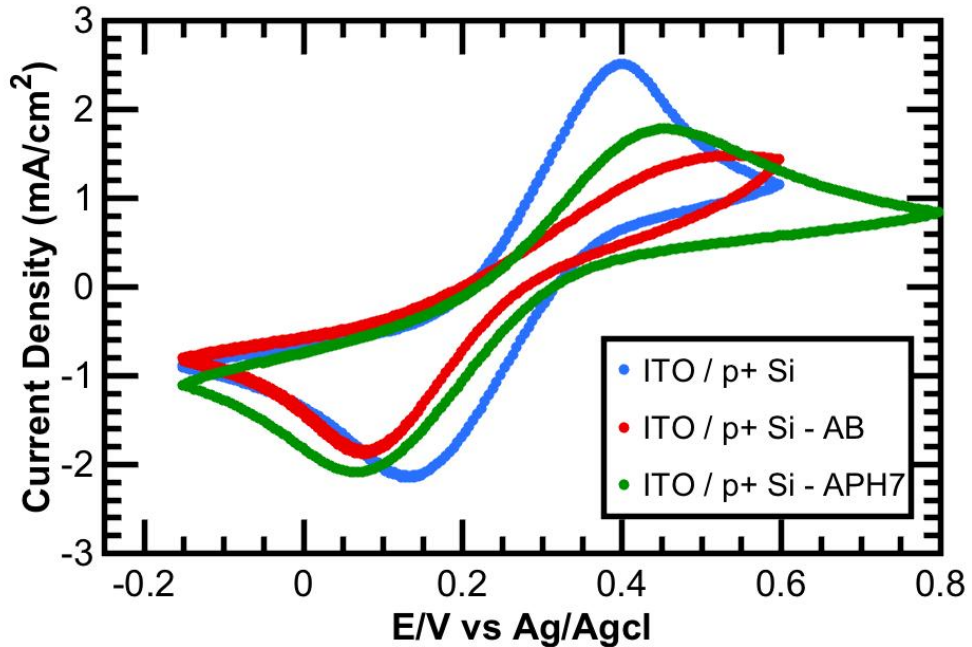
Figure 2.7: Cyclic voltammetry responses for the ITO (75nm) / p+ Si (blue line) and ITO (75nm) / p+ Si (red line - AB = After Base) after exposure to a basic solution (1M NaOH), and ITO (75nm) / p+ Si (green line - APH7 = After pH7)). There is a spreading out of the peak-to-peak responses indicating that the ITO has degraded under the different pHs.

The photovoltage can be inferred by a comparison of the centre points of the p+ Si anode in the dark and the p+n Si anode in the light and yields a value of 0.49 V which is comparable to the TiO_2 based photoanodes of 0.55 V (see chapter 4)

Figure 2.7 shows the FFC response of ITO on p+ Si without the iridium catalyst. Also shown are the FFC responses after the ITO had been exposed to a base (1M NaOH) and after the ITO had been exposed to a neutral solution (1 M phosphate-buffered, pH 7). As can be seen there is a spreading out of the peak-to-peak responses indicating that the ITO has degraded under the different pHs, TiO_2 does not suffer from this issue, as a consequence a significant amount of research was focused on using TiO_2 as a protective oxide for the water splitting cells.

2.5   Conclusions

ITO layers were deposited on Si by ion-assisted ebeam evaporation. Chemical analysis of the films (75 nm - 85 nm) by XPS determined the elemental composition of the ITO films (In 47%, Sn 6%, and O 47%). I-V and C-V measurements were carried out on ITO/n-Si, ITO/p-Si and ITO/p++Si Schottky structures. The Schottky barrier height values extracted by I-V and C-V methods on the ITO/n-Si were in agreement: 0.8 eV and 0.87 eV, respectively. The resulting ITO work function (4.85 eV- 4.92 eV) is within the range of previously published data. The high barrier height on n-Si implies lower barrier height on p-Si which was confirmed by the high current levels measured on the ITO/p-Si Schottky devices. This is a useful property for water splitting solar cells which use a p+n Si configuration in the anode.

ITO suffers from instability under different pHs, an issue which does not affect TiO_2 which can be seen in the cyclic voltammetry response shown in

figure 3.16, therefore, TiO_2 is more widely used for water splitting applications. The remainder of this thesis will discuss the properties of TiO_2 photoanodes.

Bibliography

[1] Kobayashi, H.; Tachibana, S.; Yamanaka, K.; Nakato, Y.; Yoneda, K. *Journal of Applied Physics* **1997,** *81,* 7630–7634.

[2] Kobayashi, H.; Ishida, T.; Nakamura, K.; Nakato, Y.; Tsubomura, H. *Journal of Applied Physics* **1992,** *72,* 5288–5293.

[3] Reece, S. Y.; Hamel, J. A.; Sung, K.; Jarvi, T. D.; Esswein, A. J.; Pijpers, J. J.; Nocera, D. G. *Science* **2011,** *334,* 645–648.

[4] Krol, R. *Photoelectrochemical Hydrogen Production* **2012,** 13–67.

[5] Chen, Y. W.; Prange, J. D.; Duhnen, S.; Park, Y.; Gunji, M.; Chidsey, C. E.; McIntyre, P. C. *Nature Materials* **2011,** *10,* 539.

[6] Ishida, T.; Kobayashi, H.; Nakato, Y. *Journal of Applied Physics* **1993,** *73,* 4344–4350.

[7] Nocera, D. G. *Accounts of Chemical Research* **2012,** *45,* 767–776.

[8] Xia, Z.; Zhou, X.; Li, J.; Qu, Y. *Science Bulletin* **2015,** *60,* 1395–1402.

[9] Senthilkumar, M.; Mathiyarasu, J.; Joseph, J.; Phani, K.; Yegnaraman, V. *Materials Chemistry and Physics* **2008,** *108,* 403–407.

[10] Scheuermann, A. G.; Lawrence, J. P.; Kemp, K. W.; Ito, T.; Walsh, A.; Chidsey, C. E.; Hurley, P. K.; McIntyre, P. C. *Nature Materials* **2016,** *15,* 99.

[11] Park, Y.; Choong, V.; Gao, Y.; Hsieh, B. R.; Tang, C. W. *Applied Physics Letters* **1996,** *68,* 2699–2701.

[12] Wagner, C. D. *Handbook of X-ray photoelectron spectroscopy;* Perkin-Elmer: 1979.

[13] Sze, S. M.; Ng, K. K. *Physics of semiconductor devices;* John Wiley & Sons: 2006.

[14] Dehnicke, K. *Angewandte Chemie* **1976,** *88,* 774–774.

77

Chapter 3

Investigation into the hole conduction mechanism of ALD grown TiO_2

3.1 Introduction

Titanium dioxide (TiO_2) has been investigated for a number of applications due to its physiochemical properties [1–3]. TiO_2 is a wide band-gap semiconductor (~3 eV), that exists in an amorphous state and three (anatase, rutile, and brookite) crystalline phases. Due to its large bandgap it is transparent to visible light but absorbs in the UV. It has a high refractive index (at λ=550 nm, n=2.54 for anatase or 2.75 for rutile [4,5]) and has been investigated as a high k dielectric for gate oxides [6] and for photoactive layers in solar cells [7] as it can absorb in the UV. TiO_2 is an effective photocatalyst for water and air purification and for self-cleaning surfaces due to strong oxidation and reduction power of photoexcited TiO_2 [8, 9]. More recently it has been shown that very thin TiO_2 deposited by atomic layer deposition (ALD), can be used to protect silicon photoactive layers in photoelectrochemical cells (PEC's) for water splitting [10]. In these cells photons generate electron-hole pairs at the Si anode which is immersed in water. The holes conduct through the protective oxide to a catalyst where they recombine with electrons from the water, driving the oxygen evolution reaction in the water. The electrons generated by the photons conduct to the cathode where they react with hydrogen ions in the water to form H_2. For water splitting to be economically viable, it is necessary that the corrosion-resistant layer is inexpensive and easily grown. In 2011 Chen *et al.* [10] showed that Si substrate with a native oxide layer could be coated with a pinhole-free 2 nm TiO_2 layer grown by ALD. This layer was able to prevent oxidation of the Si substrate while being thin enough to allow the tunnelling of holes from the Si substrate to the catalyst top layer. It has also recently been discussed that the use of a shallow (0.45 μm) p+ region in a p+n Si anode with a TiO_2 protection layer results in an enhanced cell performance for water splitting applications [11]. The p+ surface layer maintains a high concentration of holes at the silicon/oxide surface of the anode structure, which yields high values of photo-voltage (> 600 mV) as well

as removing the dependence of the photo-voltage on the thickness of the TiO_2 layer used to protect the silicon anode. The protective layer needs to minimize the resistance to hole transport, therefore studying the properties of the TiO_2 in relation to hole transport is of high importance.

Other potential layers such as TiO_2 grown by chemical vapour deposition [12], noble metal [13] and noble metal silicide [14] layers, were unsuccessful at obtaining a high performance, long lasting PEC.

The object of this work is to grow TiO_2 by ALD under different ALD conditions and determine how the TiO_2 composition correlates to the leakage current.

3.2   Experimental

TiO_2 thin films were deposited on p-Si(100) (10-20 Ω.cm) wafers by ALD. The silicon wafers had an initial surface clean in a Semitool Spray Acid tool. Ozone, hot deionised water, NH_4OH and HF were used to remove particles, organic contaminants and metals from the wafer surface before oxidation. Using the HF and ozone together simultaneously etches and regenerates the oxide on the surface. This treatment removes a thin layer of silicon around 0.8-1.0 nm and leaves a chemical passivation oxide around 1.5 nm thick on the wafer surface. The TiO_2 films were deposited at 200^oC in a Picosun R200 ALD system using either a thermal or plasma reaction. The titanium precursor used for the deposition is Tetrakis(dimethylamido titanium (TDMAT)($Ti(N(CH_3)_2)_4$), and either an oxygen plasma or H_2O depending on the sample. The deposition thickness target for all 5 films was 4.5 nm +/- 0.5 nm. The precursor vessel for the TDMAT was maintained at 65^oC, the H_2O was left at room temperature as sufficient vapour pressure is achieved, and the O_2 plasma characteristics are listed with the other growth parameters in table 3.1. The carrier gas flows are also listed in table 3.1. The aim of the growths was to produce films with

different amounts of oxygen incorporated into the film. For this there were two thermal growths, one where the water is overpulsed, and one where the water is underpulsed, not allowing a full layer of growth to occur. Similarly, there were three plasma growths, one in which the oxygen is in excess and two where it is underpulsed. The Picosun R200 ALD system uses a boost function for heated precursors, whereby the precursor vessel is filled with the carrier gas (N_2) to maintain a constant pressure for each pulse. The TDMAT precursor vessel had a flow of 600 sccm of N_2 to fill the precursor vessel after every pulse. For the sample ST5, the oxygen back-pressure was also reduced to 0.8 kPa, from 144 hPa, in order to achieve an oxygen deficient plasma.

Table 3.1: Sample Table

Sample Name	Oxygen Source	TDMAT Pulse	TDMAT Carrier Flow	TDMAT Purge	Oxygen Pulse	Oxygen Carrier flow	Oxygen Purge
ST1	3kW O_2 plasma	1.6s	80sccm	12.0s	28.0s	50sccm	8.0s
ST2	3kW O_2 plasma	1.6s	80sccm	12.0s	7.0s	50sccm	8.0s
ST3	H_20	1.6s	80sccm	12.0s	0.01s	150sccm	8.0s
ST4	H_20	1.6s	80sccm	12.0s	0.1s	150sccm	8.0s
ST5	1kW O_2 plasma	1.6s	80sccm	12.0s	14.6s	40sccm	12.0s

The film growth was monitored by in-situ SE using a Woollam M2000D system with a spectral range of 193 nm to 998.9 nm operating in a dynamic capture mode. All SE analysis was performed using Woollam's CompleteEASE software. A Cauchy model was used to describe the TiO_2 films deposited by ALD in this study. The sample was given a stabilisation time of 40 minutes in the chamber, as it had been observed through the in-situ SE that this was required for the sample to reach thermal equilibrium. The measurement time was set to capture data every 1.6 seconds, which allowed for measurements to be taken during the titanium and oxygen purge times. For the electrical measurements, a metal-oxide-semiconductor (MOS) device was formed by evaporating 70 nm of Ni and 150 nm of Au, onto the TiO_2 through a resist and mask with various capacitor areas, followed by a lift off process. The gate metals are deposited using a Temescal

FC200 e-beam evaporation system which is evacuated to < 5x10^{-7} Torr. The Ni is evaporated at 0.3 nm/second and the Au at 0.5 nm/second. The evaporation takes place in an unheated chamber. The samples were measured using an Agilent HP4156C analyser and an Agilent E4980 for IV and CV analysis respectively, in a Cascade semi-automatic microchamber. X-ray photoelectron spectroscopy (XPS) analysis was performed in order to obtain the elemental composition of the TiO$_2$ films. First the samples were sputtered with an Argon Gas Cluster source (10 keV, Ar1000+ clusters) for 3 seconds in order to remove the carbon over layer. Then high-resolution X-ray photoelectron spectra were recorded by using a Kratos AXIS instrument with a monochromatic Al Kα radiation of 1486.6 eV energy as the excitation source (10 mA, 15 kV). All the spectra were acquired with analyser pass energy of 20 eV and 0.1 seconds dwell time per step. Binding energy values were calibrated by employing the C 1s 284.80 eV. Mixed Gaussian-Lorentzian functions and Shirley-type backgrounds were used for reconstruction and fitting of the high-resolution spectra. Finally, some ferri/ferrocyanide (FFC) measurements were completed to determine preliminary photoelectrochemical cell performance. To do this 5 nm of Ni was deposited as an oxidation catalyst, and 20 nm of Pt was deposited on the back as an ohmic contact.

3.3   Results and Discussion

3.3.1   Film Growth and Properties

In Situ SE

ALD of TiO$_2$ has been shown to grow good quality, pin-hole free films, with good saturation and linearity [15]. The surface chemistry and chemical composition in both amorphous and crystalline phases were also studied [16]. In this work TiO$_2$ was deliberately grown with different oxygen sources, to affect the stoichiometry of the film, and to determine whether oxygen vacancies, caused by the non-

stoichiometric of the films, or impurities such as N or C, play the largest role in determining the leakage current. The thickness of the films was determined by SE. Figures 3.1 - 3.5, show the time resolved data for the 5 samples. They show the step wise nature of the ALD TiO_2 film evolution during the growth process. Figures 3.1 and ST2-In-Situ show two of plasma growths, and figures 3.3 and ST4-In-Situ show the thermal growths. Figure 3.5 shows the step-wise growth of the ST5 film when the oxygen plasma has a reduced oxygen back-pressure (down to 0.8 kPa) resulting in an under-dosed oxygen pulse. As can be seen from the figure, the GPC falls dramatically down to 0.076 nm/cycle (taken from the SE data), as for each O_2 pulse, the reaction is not surface limited but limited by the available oxygen. When the next Ti pulse comes, there are fewer available surface sites to bond to. In this way the GPC reduces, due to reactions no longer being surface limited. The lack of a complete monolayer coverage of the O_2 pulse contributes to the higher level of oxygen vacancies.
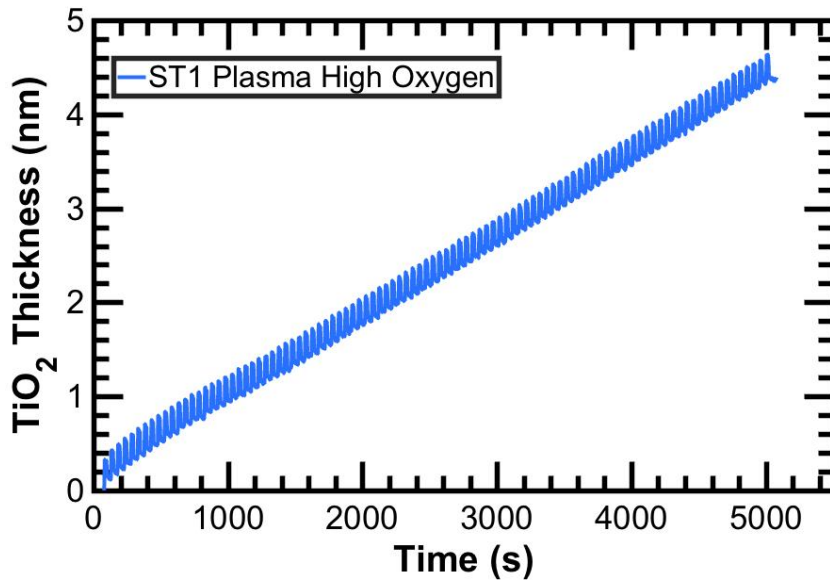
Figure 3.1: In-situ SE data from ST1, showing the step-wise nature of ALD, during the plasma growth.

The SiO_2 appears to be very chemically reactive and readily reacts with the titanium amine precursor, as there does not appear to be any nucleation delay present. The nucleation sites where the initial reaction occurs are most likely hydroxyl (OH) groups, and possibly surface defects [3]. This is evident from
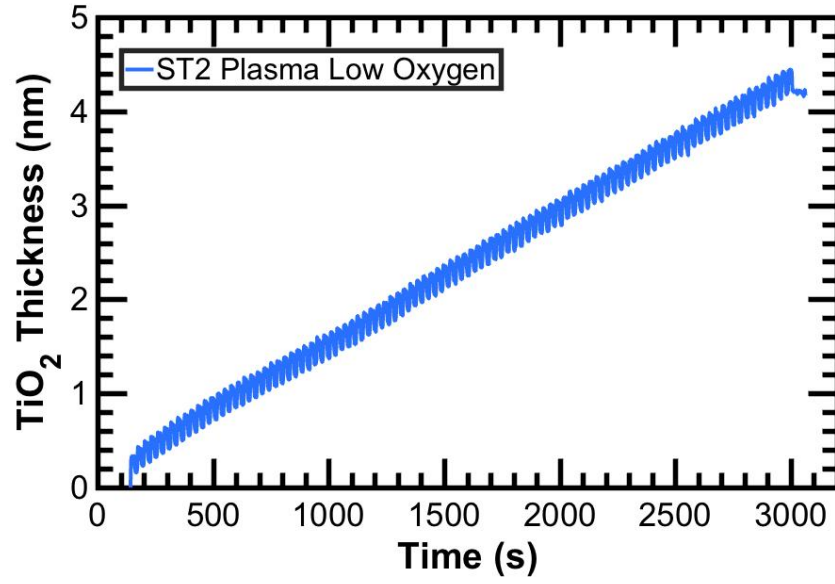
Figure 3.2: In-situ SE data from ST2. The growth uses a shorter oxygen pulse, to achieve a higher Ti^{3+} concentration.
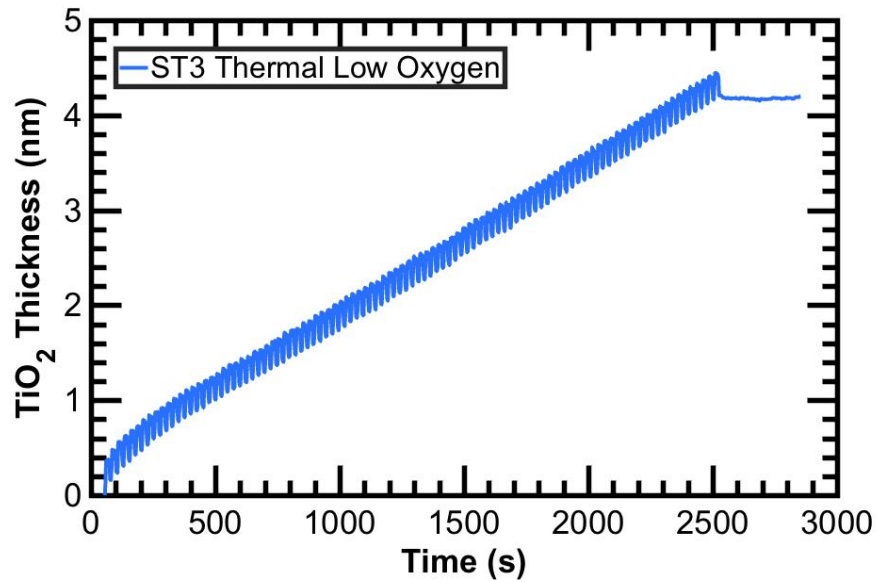
Figure 3.3: In-situ SE data from ST3. The thermal growth, has shorter oxygen pulses and purges to the plasma growths.
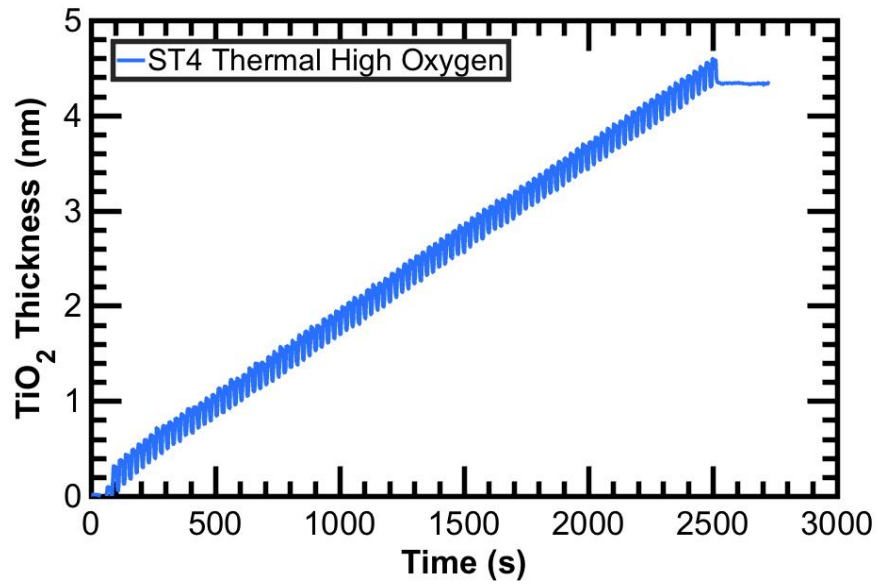
Figure 3.4: In-situ SE data from ST4. This is the standard thermal TiO_2 growth.
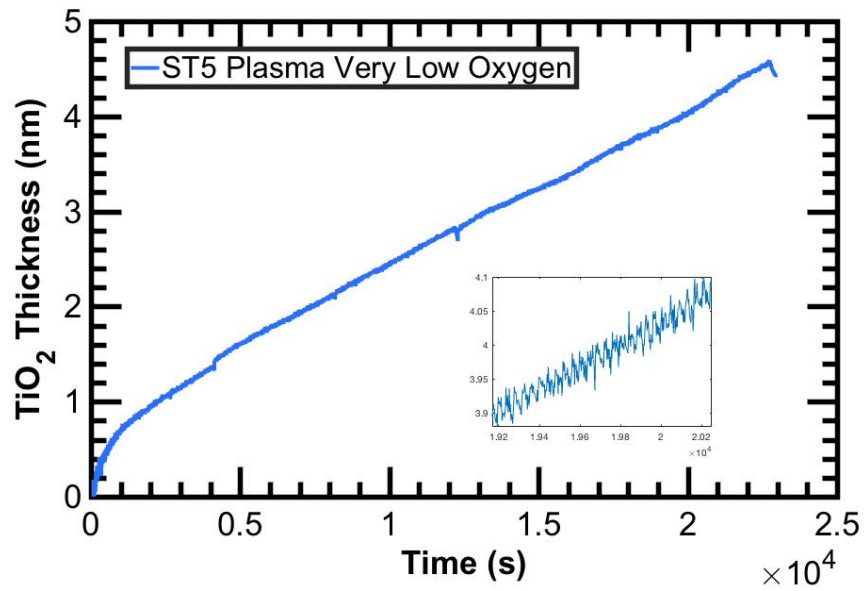
Figure 3.5: In-situ SE data from ST5. The GPC is much smaller for this growth with the reduced oxygen flow, therefore the number of cycles had to be modified.

the short nucleation regime, as can be seen from the first 6 cycles. After this the growth tends towards a linear growth per cycle (GPC). The thickness of the films was 4.39 nm, 4.17 nm (GPC = 0.044 nm/cycle), 4.20 nm (GPC = 0.042 nm/cycle), 4.33 nm (GPC = 0.043 nm/cycle) and 4.41 nm (GPC = 0.0078 nm/cycle) for ST1, ST2, ST3, ST4, ST5 respectively, with the number of cycles of ST5 altered to 560 cycles (as opposed to 100 cycles) in order to achieve the desired thickness. It is evident that the growth rate drops when the oxygen is reduced, for ST1 to ST2 and for ST4 to ST3.

X-Ray Photoelectron Spectroscopy

The film composition was determined using X-ray photoelectron spectroscopy shown in figure 4.2. Peak fitting software used the areas associated with the O 1s, Ti $2p_{3/2}$ peaks in conjunction with the relative sensitivity factors [17] for each core level in order to calculate the relative elemental composition of the film. Table 3.2 lists the residual carbon and nitrogen contents of the films. Also listed is the ratio of Ti^{3+} to Ti^{4+}. The films with the shorter oxygen pulses, especially the film grown with plasma with reduced oxygen flow, show a much higher Ti^{3+} to Ti^{4+} ratio, hence making a less stoichiometric film. This means that there is a higher density of oxygen vacancies, which is believed to be the dominating factor controlling the TiO_2 leakage current. Also evident is that the O_2 plasma tends towards a more stoichiometric film. The thermally grown sample with over-dosed H_2O compared to the O_2 plasma sample that has over-dosed oxygen pulse, shows that the plasma creates a sample with lower Ti^{3+} to Ti^{4+} ratio. However, it does also incorporate more carbon. ST3 has a lower oxygen vacancy count than ST4 despite ST3 having a reduced oxygen pulse.

3.3.2 Electrical Properties

Electrical conductivity was measured by applying a voltage sweep to the gate electrode of the $Au/Ni/TiO_2/SiO_2/Si$ MOS structure. The voltage was swept
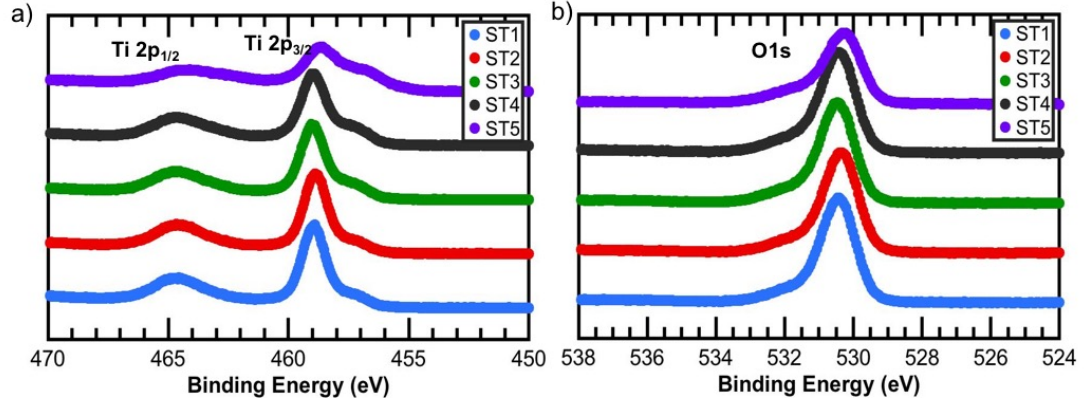
Figure 3.6: XPS analysis from TiO_2 growth. The Ti^{3+} to Ti4+ ratio can be determined from the XPS responses.

Table 3.2: XPS results detailing the percentage concentration of the Ti^{3+}, the Ti^{4+}, also the nitrogen and carbon contents.

Sample	C1s %conc	N1s %conc	Ti3+ %conc	Ti4+ %conc	Ti3+/Ti4+	O %conc
ST1	6.5	-	4.5	22.8	0.197	56.3
ST2	8.0	-	4.6	22.7	0.203	54.2
ST3	4.1	-	6.2	22.2	0.279	56.3
ST4	3.7	-	7.1	21.4	0.332	56.2
ST5	6.0	7.6	11.7	16.8	0.696	46

from 0 to +/-1.5 V, in 0.015 V steps, and measured across the wafer and on different areas. Figure 3.7 shows the leakage current density against gate voltage for the different samples detailed in table 3.1.

For the negative voltage range there is hole accumulation at the interface. Comparing first of all, the two samples grown thermally (ST3 and ST4), the sample with the shorter water pulse has a higher leakage than the sample with the water overdosed on the negative voltage side, with very little difference on the positive voltage side. Comparing the thermally grown sample with the over-dosed water pulse (ST4) to the plasma grown sample with the over-dosed plasma pulse (ST1), the plasma grown sample has a much-reduced leakage current, indicating that the plasma grown sample forms a more stoichiometric sample. This is expected as the plasma grown sample would have more energy during the reaction, prompting a more complete reaction. Then, as the plasma conditions are varied (the oxygen pulse time, oxygen flow and plasma power), it is possible to increase this leakage current, and as expected, the samples seem
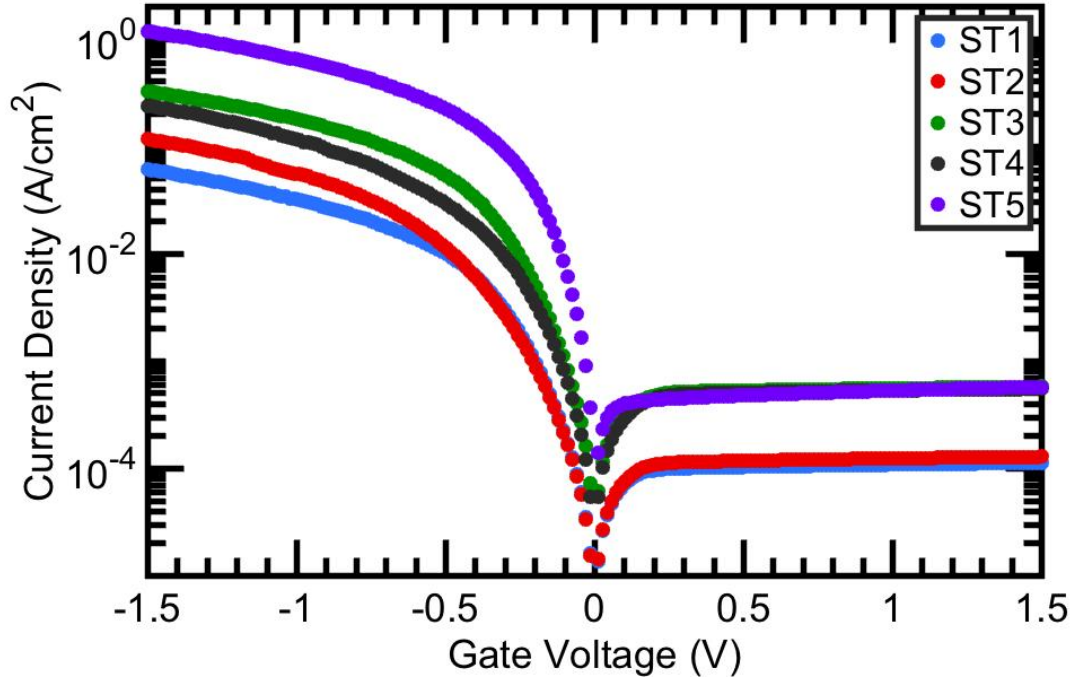
Figure 3.7: JV Sweeps of all 5 samples. The leakage current trend corresponds to the chemical composition of the films, with the main factor being the ratio of Ti^{3+} to Ti^{4+}.

to follow a trend on increased leakage with increased Ti^3+ to Ti^4+ ratio. This can be seen more clearly in figure 3.8, which shows the current density at -0.5 V, -1 V, and -1.5 V vs the ratio of Ti^{3+} to Ti^{4+}. As can be seen there is a trend of increased leaked with a higher ratio, i.e. as the films get less stoichiometric the leakage current increases.

Two samples do not follow the trend. However, this could be explained based on their carbon content. ST4 should have a slightly higher leakage than ST3 but ST4 has a higher carbon content which acts as a dopant [18,19]. ST5 has a higher leakage, although this sample has a high nitrogen incorporation, which may be adding to this current. This determines that the main factor in determining the leakage current of a TiO_2 is the ratio of Ti^{3+} to Ti^{4+}, but with the carbon content also playing a role.

CV measurements were used to determine the k values which were then used to determine the conduction mechanism from the IVs for each of the different TiO_2 layers. The voltage was swept from +1 V (depletion) to -1 V (accumulation) in
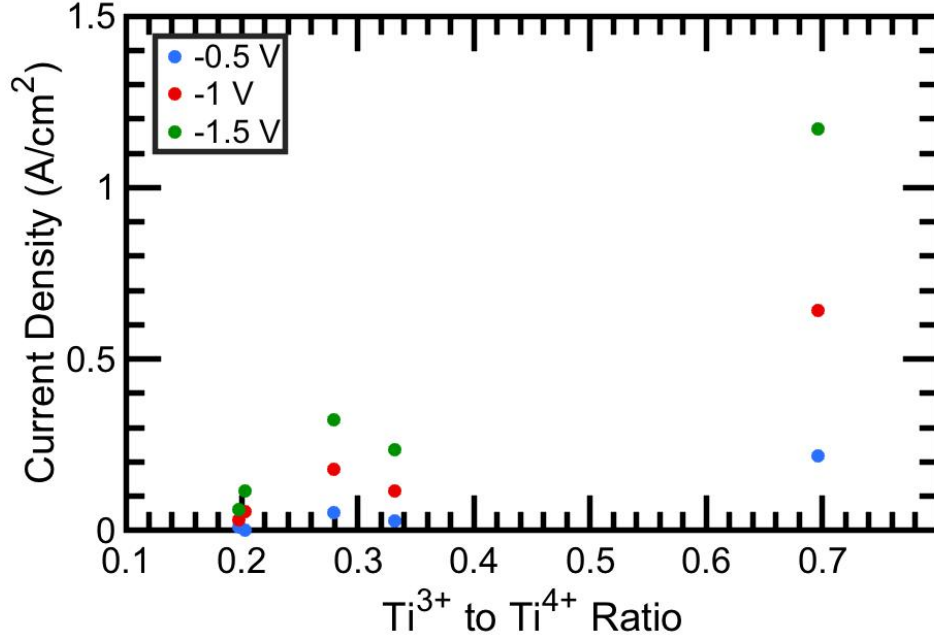
Figure 3.8: The leakage current at multiple voltage points vs the ratio of Ti^{3+} to Ti^{4+}.

the parallel circuit mode (referred to as CP-G mode). A number of checks were completed to ensure that the device was not being stressed, such as measuring the same device repeatedly to check if there was any shift in the flatband voltage (V_{fb}) and measuring multiple devices again to note any variation across the wafer. It was also noted from the room temperature CVs that the leakage current was very high and therefore difficult to determine accurately the maximum capacitance C_{max}. In order to avoid this issue, measurements were performed at -50°C, and on the 30 μm × 30 μm MOS capacitors. Although this increased the impedance, the reduced oxide leakage at -50°C and with the 30 μm × 30 μm allowed C_{max} to be determined. Figure 5.5 shows the CV measurements of the five samples. The C_{max} was determined for all samples except for ST5, where the leakage was too high to measure an accurate CV. Taking the thicknesses measured from the SE, the dielectric constant k was calculated as 13.1 ± 2.2, 13.3 ± 0.72, 20.8 ± 2.7 and 13 ± 0.72 for samples ST1, ST2, ST3, and ST4 respectively. When calculated as part of a multi-layer system where the SiO_2 layer is assumed to have a dielectric constant of 3.9 and thickness of 1.5 nm determined by the S.E.. It is not clear as to why ST3 has a higher k value to the other samples. There is a distortion in

the multifrequency CV response around 0 V, this is due to silicon dangling bond defects. There is also a change in the interface state density (D_{it}) from sample to sample, seen as the shoulder around 0 V in particular on samples ST1 and ST2. This can be explained from the growth conditions, where the plasma affects the interlayer, oxygen radicals pass through the SiO_2 and partially oxidize the Si layer, increasing the D_{it} density [20–22]. Figure 5.5 f) shows the normalised 1 MHz sweep for each of the 5 samples plotted against theoretical plots for a sample with a k value of 13 (Th. CV 1) and with a k value of 21 (Th. CV 2). The shift in flat band voltage from the theoretical CV is indicative of positive oxide charges in the film. This is expected due to an oxygen vacancy having a positive charge in TiO_2 [23]. However, the trend shows that it is likely that there is a second charge contribution, as higher levels of oxygen vacancies should result in a larger negative shift. This is contrary to what is seen, indicating that there is more than one charge contributor.

Another issue to consider is the reliability of the films based on their stoichiometry. For example, ST5 had already degraded to a lower current roughly one month after the first measurement. Further investigation into the control of the Ti^{3+} to Ti^{4+} ratio should be undertaken, to determine the correlation between this ratio and the reliability of the samples, by performing a number of reliability measurements using different accelerating factors, most relevant of which is probably temperature.

3.3.3 Conduction Mechanism

In order to calculate the hole conduction mechanism through the TiO_2, knowledge of the electric field in each of the dielectric films is required. If we consider that a negative voltage is applied at the gate, it will produce a band bending that will
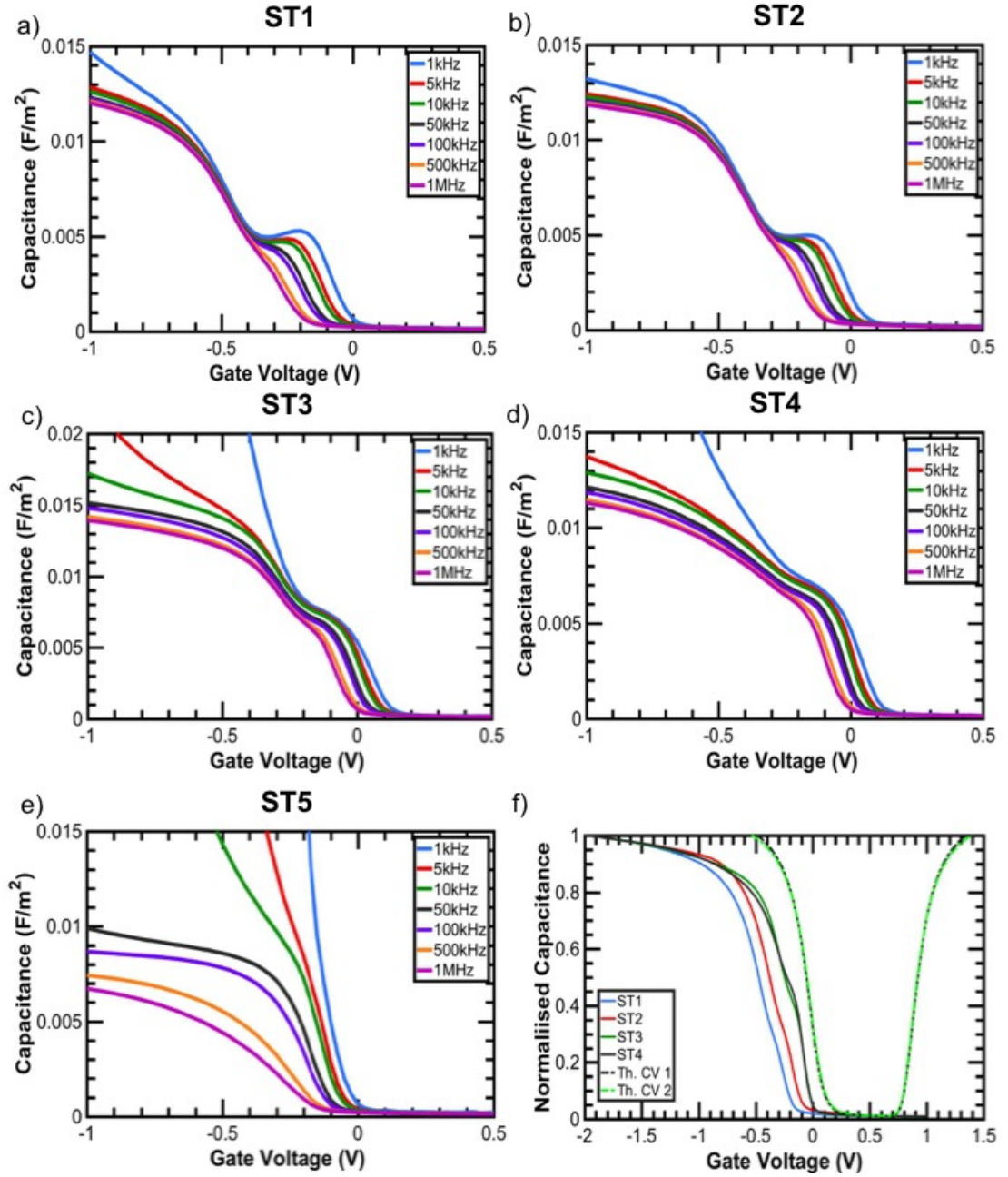
Figure 3.9: CV Sweeps of all 5 samples measured at -50ºC. The CV is used to calculate the k values of the samples. Also plotted are the normalised 1MHz sweep for each sample, with theoretical CVs for a sample with a k value of 12 (Th. CV 1) and with a k value of 21 (Th. CV 2). This shows shift in flat band voltage.

tend the device to accumulation. The gate voltage is expressed as

$$V_G = V_{SiO_2} + V_{TiO_2} + \phi_S + \Phi_{MS} \qquad (3.1)$$

where V_{SiO_2} and V_{TiO_2} are the voltage drops across the silicon oxide film and titanium oxide film respectively, ϕ_S is the silicon surface potential and Φ_{MS} is the difference is work functions of the metal and semiconductor [24]. By having two oxides, they can be considered as two capacitors in series, therefore it is possible to calculate V_{TiO_2}, using

$$V_{TiO_2} = V_{ox} \times \frac{C_{SiO_2}}{C_{TiO_2} + C_{SiO_2}} \qquad (3.2)$$

where V_{ox} is the voltage across the whole oxide and C_{SiO_2} and C_{TiO_2} are the capacitances of the SiO_2 and TiO_2 layers respectively. Knowing the voltage, the electric field can be calculated with the thickness. There are a number of different conduction mechanisms that contribute to the current density, such as direct tunnelling (J_{DT}), Fowler-Nordheim (FN) tunnelling (J_{FN}), thermionic emission (J_{TE}) and Poole-Frenkel (J_{PF}). Direct tunnelling is expected to dominate if the overall thickness is below 5 nm, however in thicker films other mechanisms tend to dominate. It is possible for more than one current conduction mechanism to be present, so in the thin oxide samples that are used for protective layers the high leakage may be due to multiple mechanisms, such as J_{TE} and J_{PF}. However, FN tunnelling only occurs at high electric fields, larger than about 6MV/cm [25]. The current density behaviour of each mechanism can be expressed as

$$\begin{aligned} J_{DT} = & \frac{A \cdot E_d^2}{[1 - (\Phi_b - q \cdot V_d)^{0.5}]^2} \cdot \exp\left[-\frac{B}{E_d} \cdot \frac{\Phi_b^{3/2} - (\Phi_b - q \cdot V_d)^{3/2}}{\Phi_b^{3/2}} \right] \\ & \times (1 - \exp[-\frac{3}{2} \cdot \frac{B}{E_d} \cdot \frac{\Phi_b^{1/2} - (\Phi_b - q \cdot V_d)^{1/2}}{\Phi_b^{3/2}} \cdot E_{FS}]) \end{aligned} \qquad (3.3)$$

$$J_{FN} = A \cdot E_d^2 \cdot \exp\left[-\frac{B}{E_d}\right] \tag{3.4}$$

$$J_{PF} = E_d \cdot \exp\left[-\frac{q}{kT}\left(\Phi_t - \sqrt{\frac{qE_d}{\pi\varepsilon_0 k_d}}\right)\right] \tag{3.5}$$

$$J_{TE} = A^* T^2 \cdot \exp\left[-\frac{q}{kT}\left(\Phi_b - \sqrt{\frac{qE_d}{4\pi\varepsilon_0 k_d}}\right)\right] \tag{3.6}$$

where: $A = \frac{q^3 m_0}{8\pi h m_{ox} \Phi_t}$; $B = \frac{4\sqrt{2m_{ox}\Phi_b^3}}{3\hbar q}$; $A^* = 120[Am^{-2}K^{-2}]$. m_0 is the free election mass, m_{ox} is the effective mass in the dielectric film, Φ_b is the barrier height, Φ_b is the trap height V_d, E_d, and k_d are the voltage drop, the electric field and the dynamic dielectric constant of the dielectric film respectively.

Thermionic emission and Poole-Frenkel conduction mechanisms have been observed in TiO_2 [24]. Thermionic Emission is the emission of a carrier from the conduction (or valence) band of the semiconductor into the conduction (or valence) band of the semiconductor. The equation 3.6 can be linearised to

$$ln(J_{TE}/T^2 = \frac{\sqrt{q/4\pi\varepsilon_0 k_d}}{kT/q}\sqrt{E} - \frac{q\Phi_B}{kT} + ln(A) \tag{3.7}$$

the slope (m) and y intercept (y_0) are:

$$m = \frac{\sqrt{q/4\pi\varepsilon_0 k_d}}{kT/q} \tag{3.8}$$

$$y_0 = -\frac{q\Phi_B}{kT} + ln(A) \tag{3.9}$$

The IV data for ST1, ST2, ST3, ST4 at multiple temperatures was plotted according to 3.7 in figure 3.10

All the samples show linear regions. The barrier height and the dynamic

93
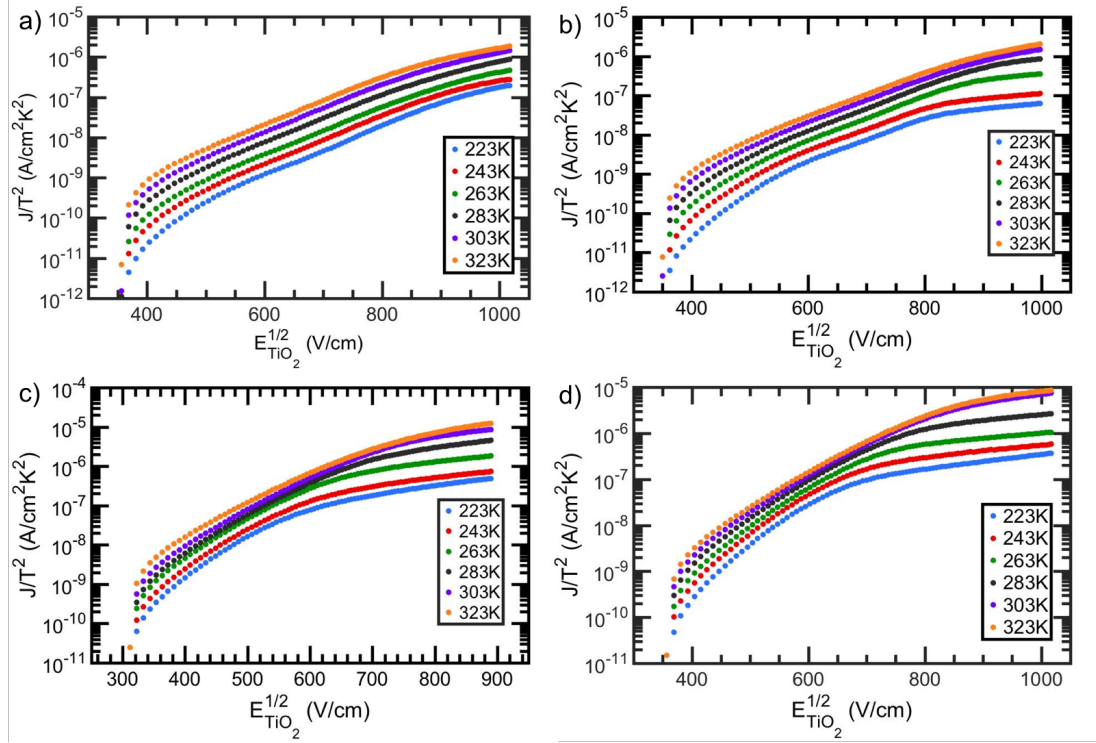
Figure 3.10: Semi logarithmic plot of J/T^2 vs $E_d^{1/2}$, the presence of a straight line can indicate the presence of thermionic emission mechanism. a) ST1, b) ST2, c) ST3, d) ST4.

dielectric constant was calculated from the slope and the y intercept for the different temperature plots, with these values being used from the mid-field region giving unrealistic values. Using the mid-field, all the samples gave similar results as the barrier height should be similar for the samples and the results agree with this. This observation is further evidence that the mid-field region displays thermionic emission. The results are summarized in table 3.3.

Table 3.3: The Schottky barrier heights and dynamic dielectric constant, calculated from the thermionic emission plots over the different temperatures.

Sample	Dynamic dielectric constant	Barrier height
ST1	1.2 - 2.5	0.62 - 0.84 eV
ST2	1.2 - 2	0.65 - 0.86 eV
ST3	0.77 - 0.82	0.65 - 0.79 eV
ST4	0.81 - 0.83	0.65 - 0.84 eV

These values for the dynamic dielectric constant are very low, indicating that this is not the main current mechanism.

Poole-Frenkle has been observed as the dominant conduction mechanism in
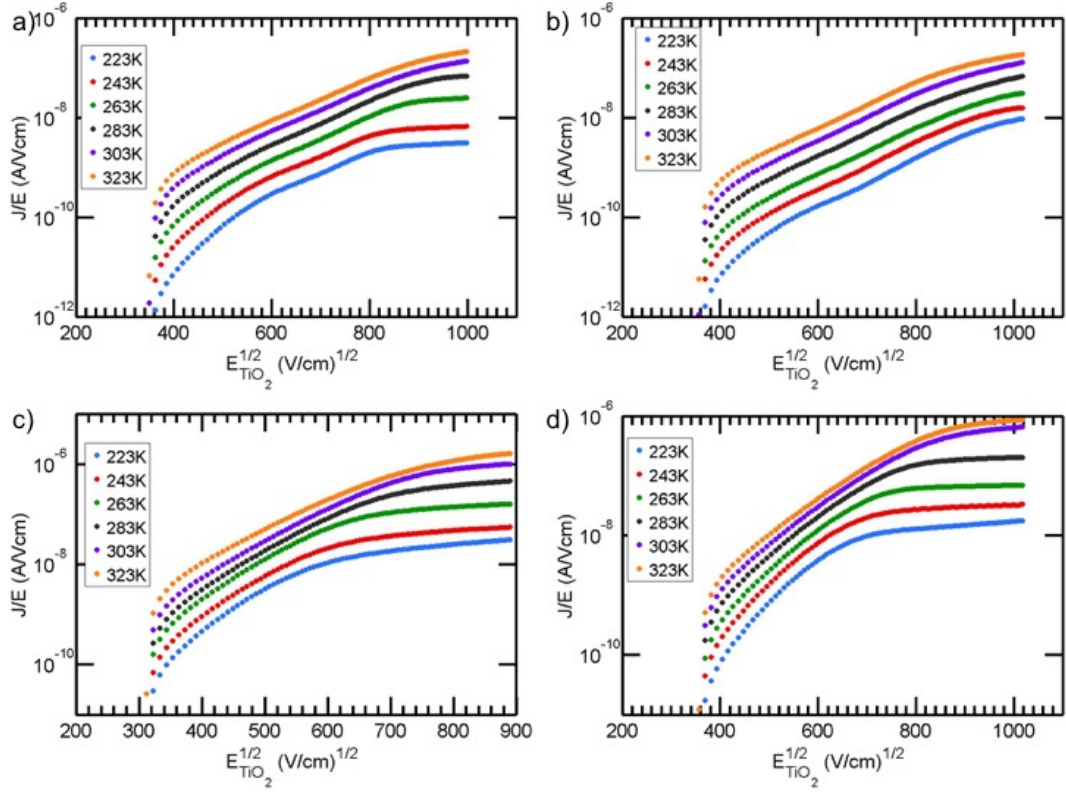
Figure 3.11: Semi logarithmic plot of J vs $E_d^{1/2}$, at different temperatures. The presence of a straight line can indicate the presence of Poole-Frenkel mechanism. a) ST1, b) ST2, c) ST3, d) ST4.

oxides with a large trap density. Electrons from the conduction band (or holes from the valence band) hop in and out of the traps and in this way conduct through the oxide. The equation 3.5 can be linearised to:

$$ln(J_{PF}/E) = \left[-\frac{q}{kT}\left(\Phi_t - \sqrt{\frac{qE_d}{\pi\varepsilon_0 k_d}} \right) \right] + ln(C) \qquad (3.10)$$

the slope (m) and y intercept (y_0) are:

$$m = \frac{q}{kT}\sqrt{\frac{q}{\pi\varepsilon_0 k_d}} \qquad (3.11)$$

$$y_0 = -\frac{q\Phi_T}{kT} + ln(C) \qquad (3.12)$$

Similar analysis to the thermionic emission above was performed. Figure 3.11

shows the plot of $\ln(\mathrm{J_{PF}}/\mathrm{E})$ verses $\sqrt{E}$. The values for the dynamic dielectric constant and the trap heights are summarized in table 3.4. The dynamic dielectric constant values calculated for ST1 and ST2 match the refractive index used in the ellipsometry data. However, ST3 and ST4 start to fall out of this range.
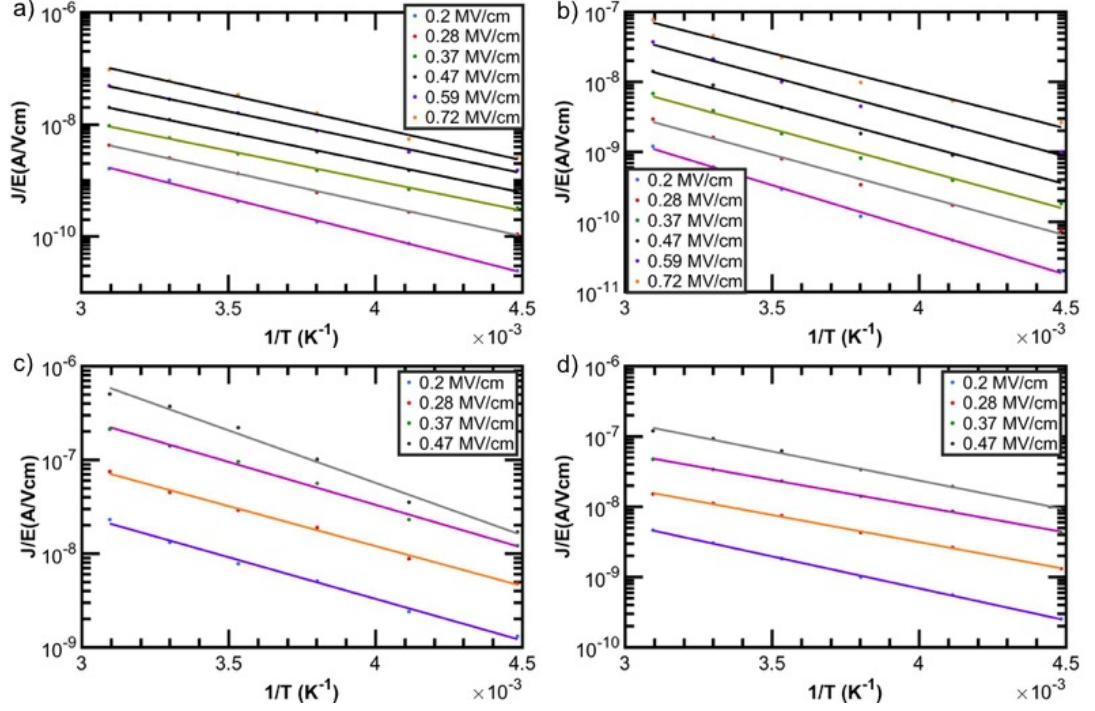
Figure 3.12: Poole-Frenkel Arrhenius plot of leakage current measured at different electric fields. a) ST1, b) ST2, c) ST3, d) ST4.

Table 3.4: The trap heights and dynamic dielectric constant, calculated from the Poole-Frenkle plots over the different temperatures.

Sample	Dynamic dielectric constant	Barrier height
ST1	7.6 - 13.8	0.55 - 0.68 eV
ST2	6.8 - 11.7	0.57 - 0.7 eV
ST3	5 - 5.1	0.55 - 0.64 eV
ST4	5.1 - 6	5.1 - 6 eV

It has not been possible to differentiate between thermionic emission and Poole-Frenkel emission as the conduction mechanism, and it is not clear what the second linear region in the samples ST4 and ST5 indicates. Therefore, additional analysis is required to try to differentiate between them. Thermionic emission and Poole-Frenkle mechanisms follow an Arrhenius type relationship between leakage current density and temperature. From this the energy barrier

to conduction can be extracted and may permit the identification of the dominant conduction mechanism.

Figure 3.12 shows the Poole-Frenkle emission plotted as $\mathrm{Ln}(J_{PF}/E)$ versus $1/T$, which predicts Arrhenius behaviour [25]. The slope:
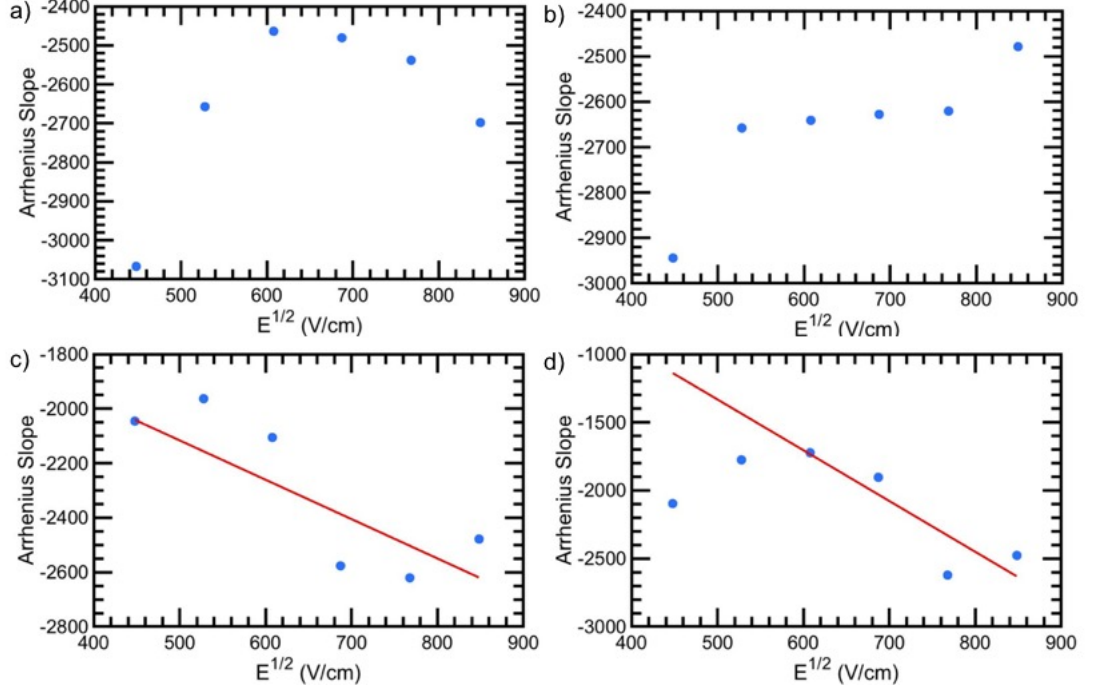
Figure 3.13: The slopes of the Arrhenius plots in figure 3.12 plotted versus $\sqrt{E}$. a) ST1, b) ST2, c) ST3, d) ST4.

$$m = \frac{q\Phi_T - \sqrt{q^3 E/\pi\varepsilon_0 k)_d}}{k} \tag{3.13}$$

is proportional to the reduced trap barrier, which reduces with increasing electric field. The plot of this slope m, versus $\sqrt{E}$ for a number of electric field values, see figure 3.13, allows for the extraction of Φ_T from the y intercept at $\sqrt{E} = 0$.

$$y_0 = \frac{-q\Phi_T}{k} \tag{3.14}$$

Figure 3.13 shows the slopes from the Arrhenius plot for various electric fields, to verify the suitability of Poole-Frenkel emission as the dominant leakage current mechanism. According to equation 3.13 the value of the slopes should
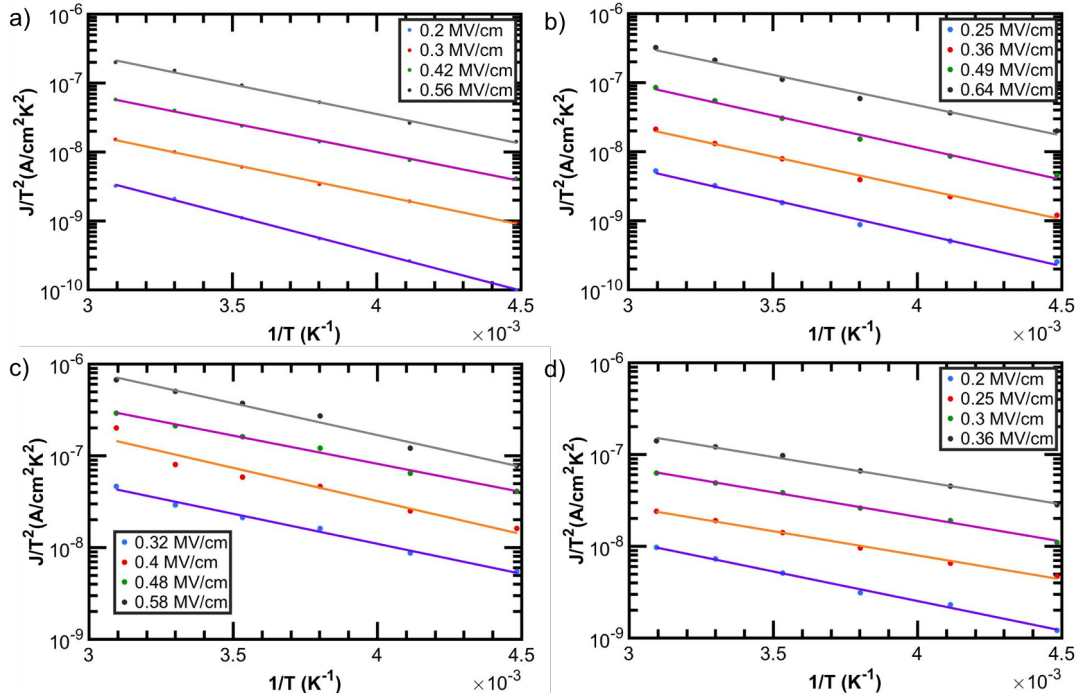
Figure 3.14: Thermionic Emission Arrhenius plot of leakage current measured at different electric fields.

decrease with increasing electric field, however the values do not strictly show this behaviour. Although there is a general trend in that direction, for ST3 and ST4. A linear fit was applied to the data for ST3 and ST4 and a trap energy height was calculated from the y intercept of 0.25, 0.29 eV. However, it is clear that Poole-Frenkel is not the dominant conduction mechanism, but that the two samples with the higher oxygen vacancies have a larger element of Poole-Frenkel.

To observe the Arrhenius behaviour using the thermionic emission equation, a plot of $\ln(J_{SE}/T^2)$ versus $1/T$ as shown in figure 3.14, the slope of this plot being:

$$m = \frac{q\Phi_B - \sqrt{qE/4\pi\varepsilon_0 k_d}}{k} \tag{3.15}$$

Similar analysis to Poole-Frenkel was undertaken with m versus $\sqrt{E}$ was plotted for a number of different electric field values and Φ_B can be calculated at $\sqrt{E} = 0$, as seen in figure 3.15. Again, the slopes should decrease with increasing electric field. However, the results do not show this behaviour and it

is hard to see a trend in this case.

$$y_0 = \frac{q\Phi_B}{k} \tag{3.16}$$
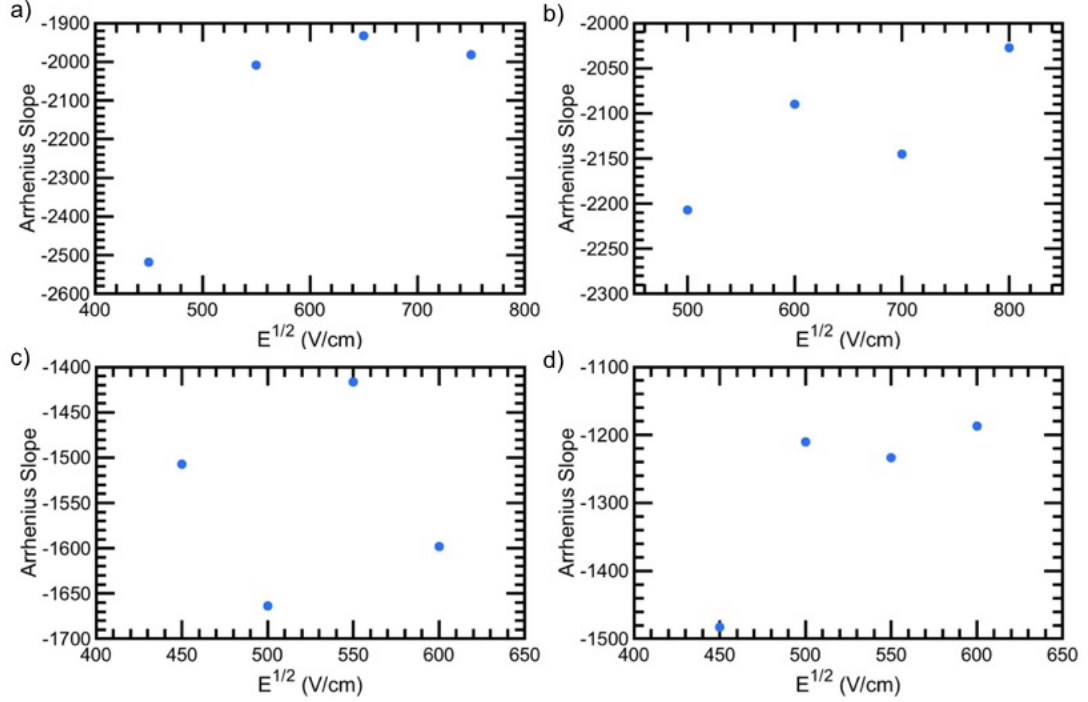
Figure 3.15: The slopes of the Arrhenius plots (thermionic emission) in Figure 3.14 plotted versus $\sqrt{E}$.

For samples ST3 and ST4 the indication of Poole-Frenkel as the dominant mechanism for the current is stronger than the indication of thermionic emission, however it is evident that both mechanisms are present from the Arrhenius data. Ultimately it can be determined that there is no clear dominant current mechanism but the increased presence of oxygen vacancies increases the trap density and therefore Poole-Frenkel becomes more prominent.

3.3.4   Cyclic Voltammetry

Ferri/ferrocyanide cyclic voltammetry measurements are used as a benchmark test to characterise the efficiency of electronic transport across the interface of the sample to the solution. The electron transfer between the ferri/ferrocyanide

solution and the metal electrodes are fast, allowing for the electronic transport across the TiO$_2$ layer to be characterised [26]. Figure 3.16 shows the cyclic voltammetry response of the samples measured in the photoelectrochemical cell. The samples have 2 nm of Ni on the TiO$_2$ surface, to form the MOS anode and to also act as an oxygen evolution catalyst. The samples are measured in the dark. As can be seen, there is a difference of the peak-to-peak voltage depending on the sample. The larger the peak-to-peak voltage the greater the resistance of the sample. This trend also corresponds to the JVs of figure 3.7. Hence the current through the device for photoelectrochemical cell measurements has a large dependence on the conduction through the TiO$_2$. Being able to improve this conduction would be beneficial to the performance of the cell.
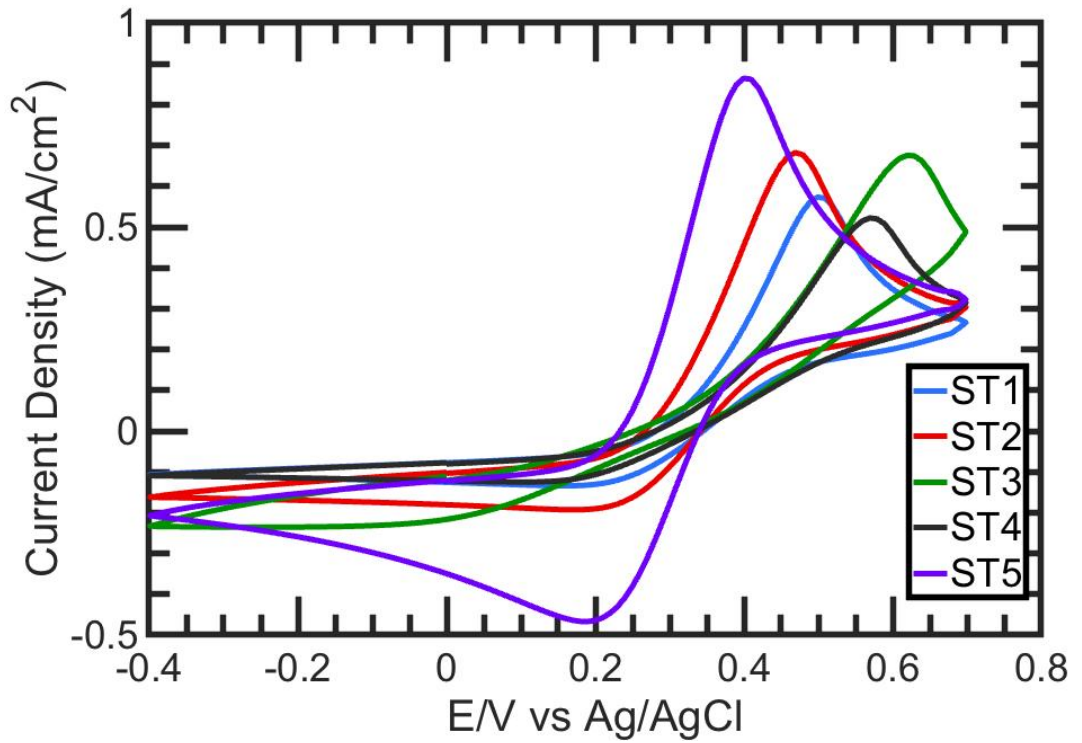
Figure 3.16: Cyclic voltammetry responses for the Ni/TiO$_2$/SiO$_x$/p Si structures in the dark. Note the spread in peak to peak voltage is due to the resistance of the sample.

3.4   Conclusions and Future work

In this work we investigated how the chemical composition of ALD grown TiO_2 from TDMAT affected the leakage current. It has been shown that the main factor which determines the leakage current is the ratio of Ti^{3+} to Ti^{4+} and therefore the oxygen vacancies. However, there are other factors that determine the leakage current, as shown the carbon content plays a role as well. It has been shown that it is possible to control this Ti^{3+} to Ti^{4+} ratio by controlling the oxygen precursor, whether it is an O_2 plasma or the H_2O. However, a high Ti^{3+} to Ti^{4+} ratio does result in N being left in the film from the precursor.

Further study into the role that carbon plays in the leakage current would be beneficial, possibly by repeating this experiment and preparing samples with a number of different carbon contents.

The current mechanism for the different samples were investigated by multiple temperature I-V sweeps. Thermionic emission and Poole-Frenkel emission were considered likely candidates. Thermionic emission was fitted to the data; however, the dynamic dielectric constant was not consistent with values used for ellipsometry. Poole-Frenkel data fit closer to the ellipsometry data, however not perfectly.

An Arrhenius analysis was performed to further investigate the two different conduction mechanisms. From this, Poole-Frenkel was considered a better fit for samples ST3 and ST4, however, it could not successfully describe the current flow through the sample. Further investigation is required to fully identify the dominant conduction mechanism.

Bibliography

[1] Chen, X.; Mao, S. S. *Chem. Rev* **2007,** *107,* 2891–2959.

[2] Khataee, A. *Nanostructured Titanium Dioxide Materials: Properties, Preparation and Applications;* World Scientific: 2012.

[3] Puurunen, R. L. *Journal of Applied Physics* **2005,** *97,* 12.

[4] Wang, Z.; Helmersson, U.; Käll, P.-O. *Thin Solid Films* **2002,** *405,* 50–54.

[5] Reyes-Coronado, D.; Rodríguez-Gattorno, G.; Espinosa-Pesqueira, M.; Cab, C.; de Coss, R. d.; Oskam, G. *Nanotechnology* **2008,** *19,* 145605.

[6] Wang, C.-W.; Chen, S.-F.; Chen, G.-T. *Journal of Applied Physics* **2002,** *91,* 9198-9203.

[7] Carp, O.; Huisman, C.; Reller, A. *Progress in Solid State Chemistry* **2004,** *32,* 33 - 177.

[8] Fujishima, A.; Honda, K. *Nature* **1972,** *238,* 37–38.

[9] Zaleska, A. *Recent Patents on Engineering* **2008,** *2,* 157–164.

[10] Chen, Y. W.; Prange, J. D.; Dühnen, S.; Park, Y.; Gunji, M.; Chidsey, C. E.; McIntyre, P. C. *Nature Materials* **2011,** *10,* 539–544.

[11] Scheuermann, A. G.; Lawrence, J. P.; Kemp, K. W.; Ito, T.; Walsh, A.; Chidsey, C. E.; Hurley, P. K.; McIntyre, P. C. *Nature Materials* **2015,** *15,* 1.

[12] Kohl, P. A.; Frank, S. N.; Bard, A. J. *Journal of The Electrochemical Society* **1977,** *124,* 225–229.

[13] Howe, A. T.; Hawkins, R. T.; Fleisch, T. H. *Journal of The Electrochemical Society* **1986,** *133,* 1369–1375.

[14] Fan, F. R. F.; Keil, R. G.; Bard, A. J. *Journal of the American Chemical Society* **1983,** *105,* 220–224.

[15] Xie, Q.; Jiang, Y.-L.; Detavernier, C.; Deduytsche, D.; Van Meirhaeghe, R. L.; Ru, G.-P.; Li, B.-Z.; Qu, X.-P. *Journal of Applied Physics* **2007,** *102,* 8.

[16] Reiners, M.; Xu, K.; Aslam, N.; Devi, A.; Waser, R.; Hoffmann-Eifert, S. *Chemistry of Materials* **2013,** *25,* 2934–2943.

[17] Wagner, C. D. *Handbook of X-ray photoelectron spectroscopy;* Perkin-Elmer: 1979.

[18] Reddy, K. M.; Baruwati, B.; Jayalakshmi, M.; Rao, M. M.; Manorama, S. V. *Journal of Solid State Chemistry* **2005,** *178,* 3352–3358.

[19] Di Valentin, C.; Pacchioni, G.; Selloni, A. *Chemistry of Materials* **2005,** *17,* 6656–6665.

[20] Lim, J. W.; Yun, S. J.; Lee, J. H. *Electrochemical and Solid-State Letters* **2004,** *7,* F73–F76.

[21] Lim, J. W.; Yun, S. J. *Electrochemical and Solid-State Letters* **2004,** *7,* F45–F48.

[22] Song, H.-J.; Lee, C.-S.; Kang, S.-W. *Electrochemical and Solid-State Letters* **2001,** *4,* F13–F14.

[23] Weibel, A.; Bouchet, R.; Knauth, P. *Solid State Ionics* **2006,** *177,* 229-236.

[24] Tinoco, J.; Estrada, M.; Iñiguez, B.; Cerdeira, A. *Microelectronics Reliability* **2008,** *48,* 370–381.

[25] Bentarzi, H. Review of Transport Mechanism in Thin Oxides of MOS Devices. In *Transport in Metal-Oxide-Semiconductor Structures: Mobile Ions Effects on the Oxide Properties*; Springer Berlin Heidelberg: Berlin, Heidelberg, 2011.

[26] Dehnicke, K. *Angewandte Chemie* **1976,** *88,* 774–774.

Chapter 4

Investigating the effect of TiO_2 thickness on the electrical conductivity and photoelectrochemical response of metal/TiO_2/SiO_x/Si photoanodes

4.1 Introduction

The solar splitting of water into hydrogen and oxygen is a central component in the creation of clean fuels from a renewable energy source. Recently it has been shown that the metal-oxide-semiconductor (MOS) structure, which is a key element of insulating gate transistor devices [1], is also a promising candidate as a photoanode in electrochemical cells for the production of hydrogen. One of the principal challenges associated with photoanodes/photocathodes in photoelectrochemical cells, is to engineer the structures to simultaneously achieve efficient light to oxygen/hydrogen conversion and long-term stability. In 2011, Chen et al. first used ultrathin (1-2 nm) atomic layer deposition (ALD) of TiO_2 to protect the silicon anode surface against oxidation [2]. Recently, Hu et al. [3] fabricated 100 nm ALD TiO_2 films and observed a photocurrent onset voltage during water oxidation that was essentially TiO_2 thickness-independent. As mentioned in chapter 3 the use of a p+n Si anode with a shallow junction depth combined with the TiO_2 protective oxide results in an enhanced cell performance. Both p++ Si and p+n Si anodes were used in this study to see if there is a relationship between the cell performance and the TiO_2 oxide deposited on it.

In this work we investigated the effect of oxide thickness for TiO_2 films from 2 nm to 137 nm deposited by ALD on silicon using both dark current-voltage analysis and the response of the TiO_2/SiOx/Si MOS photoanode in a photoelectrochemical cell.

4.2 Experimental

TiO_2 was grown by atomic layer deposition (ALD) on p++ Si(100) and p+n Si(100) 100 mm diameter substrates. For the p+n structure the peak hole surface concentration is $5 \times 10^{19} cm^{-3}$ with a junction depth of 430 nm. The n Si

substrate doping is $4.9 \times 10^{15} cm^{-3}$. For the p++ silicon samples the boron doping concentration is around $5 \times 10^{19} cm^{-3}$. The substrates received an initial surface clean in a Semitool Spray Acid tool. Ozone, hot deionised water, NH_4OH and HF were used to remove particles, organic contaminants and metals from the wafer surface before oxidation. Using the HF and ozone together simultaneously etches and regenerates the oxide on the surface. This treatment removes a thin layer of silicon around 0.8-1.0 nm and leaves a chemical passivation oxide around 1.5 nm thick on the wafer surface.

The TiO_2 was grown by ALD at 170°C in a Cambridge Nanotech Fiji 200 using Tetrakis (dimethylamido)titanium (TDMAT), which was heated to 65°C, as the Ti precursor and water as the oxygen source. The TiO_2 growth rate was assumed to be 0.05 nm/cycle to yield target TiO_2 thickness values of 2, 5, 10, 50, 110 nm.

Each of the films optical properties were measured by ex-situ SE using a Woollam M2000D system with a spectral range of 193 nm to 998.9 nm. All SE analysis was performed using Woollam's CompleteEASE software. A Cauchy model was used to describe the TiO_2 films deposited by ALD in this study. For the electrical measurements, a metal-oxide-semiconductor (MOS) device was formed by evaporating 70 nm of Ni and 150 nm of Au, onto the TiO_2 using a mask that gives a range of capacitor sizes. The gate metals are deposited using a Temescal FC200 e-beam evaporation system which is evacuated to $< 5x10^{-7}$ Torr. The Ni is evaporated at 0.3 nm/sec and the Au at 0.5 nm/sec. The evaporation took place in an unheated chamber. The samples were measured using an Agilent HP4156C analyser for IV analysis, in a Cascade semi-automatic microchamber. Samples were also metallized with 2 nm of Ni as an oxidation catalyst, for cyclic voltammetry measurements in ferri/ferrocyanide (FFC) to determine preliminary photoelectrochemical cell performance.

Transmission electron microscopy (TEM) specimens for cross section analysis

(XTEM) were prepared using the conventional method: gluing face to face small pieces cut from the area of interest using M-bond, followed by mechanical polishing and ion milling in a Gatan PIPS model 691 apparatus. TEM was performed using a Jeol ARM 200F electron microscope, performing TEM imaging. Optical properties were measured by ex-situ SE using a Woollam M2000D system with a spectral range of 193 nm to 998.9 nm. All SE analysis was performed using Woollam's CompleteEASE software. A Cauchy model was used to describe the TiO_2 films deposited by ALD in this study.

X-ray photoelectron spectroscopy (XPS) analysis was performed in order to obtain the elemental composition of the TiO_2 films. First the samples were sputtered with an Argon Gas Cluster source (10 keV, Ar1000+ clusters) for 3 s in order to remove the carbon over layer. Then high-resolution X-ray photoelectron spectra were recorded by using a Kratos AXIS instrument with a monochromatic Al Kα radiation of 1486.6 eV energy as the excitation source (10 mA, 15 kV). All the spectra were acquired with analyser pass energy of 20 eV and 100 ms dwell time per step. Binding energy values were calibrated by employing the C 1s 284.80 eV. Mixed Gaussian-Lorentzian functions and Shirley-type backgrounds were used for reconstruction and fitting of the high-resolution spectra. Peak fitting analysis was carried out using Analyser peak fitting software. Relative sensitivity factors for the calculation of the elemental composition percentages from the acquired spectra were taken from published values [4].

4.3   Results and Discussion

Structural Analysis Figure 5.1 shows the TEM analysis of the TiO_2 thickness series on p++ Si. The TiO_2 thickness values were 2 nm, 4.8 nm, 10 nm, 54 nm and 137 nm, consistent with an initial growth rate of 0.05 nm/cycle (2 nm -10 nm), increasing to 0.055 nm/cycle (nominal 50 nm sample) and 0.062 nm/cycle
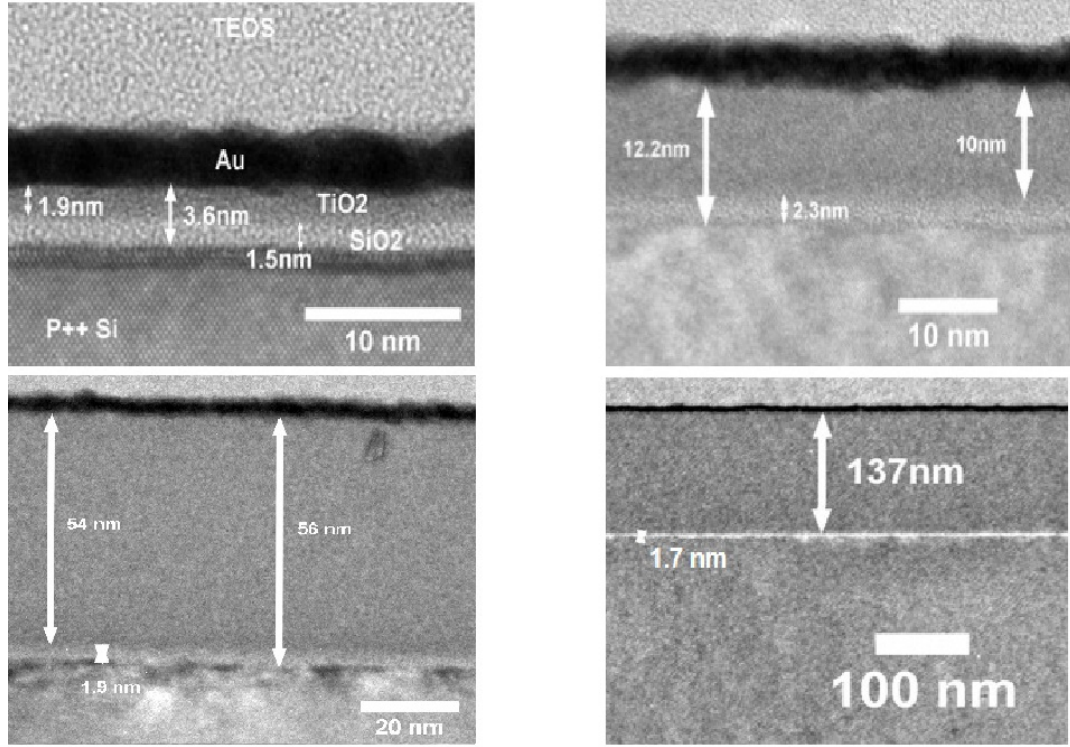
Figure 4.1: TEM analysis from TiO_2 growth. The Au/TEOS are deposited for TEM sample preparation.

(for the nominally 110 nm sample). The increase in GPC is due to growth moving out of the nucleation regime The SiO_2 interlayer thickness was in the range 1.5 to 2.5 nm.

Peak fitting analysis was carried out using Analyser peak fitting software. Relative sensitivity factors for the calculation of the elemental composition percentages from the acquired spectra were taken from published values [4]. XPS analysis shows the films becoming more stoichiometric as they get thicker. This is as expected as the nucleation regime should last around 7 nm (see chapter 5). After this the growth enters the bulk regime and shows a trend towards a more stoichiometric growth favouring the Ti^{4+} over the Ti^{3+}, as the growth progresses into the bulk regime. XPS results are summarised in figure 4.2.

Optical responses are shown in figure 4.3 showing the refractive index over the

Binding Energy	$Ti^{4+}2p_{3/2}$	$Ti^{4+}2p_{1/2}$	$Ti^{3+}2p_{3/2}$	$Ti^{3+}2p_{1/2}$
2nm	458.80	464.35	461.70	457.40
50nm	458.90	464.40	461.60	457.30
110nm	458.82	464.39	461.70	457.40

	O1s (native)	O1s - TiO_2	O1s - H
SiO_2 Ref.	529.50	NA	NA
2nm	529.15	527.45	Na
50nm	NA	527.48	529.12
110nm	NA	527.5	529.07
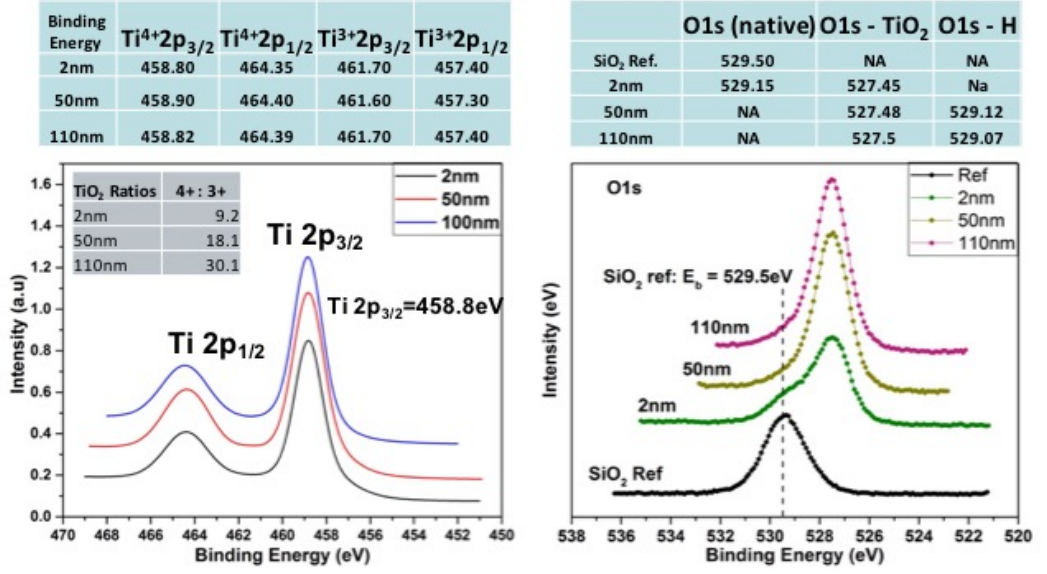
Figure 4.2: XPS analysis from TiO_2 growth. The films show a more stoichiometric growth as the sample goes more into the bulk growth regime.

spectral range, for the different samples. The SE was modelled using the Cauchy model where the thicknesses were fixed values known from the TEM. It was then possible to fit the model and extract the optical constants. The response for the thickest sample was limited as absorption in the UV had become an issue. As can be seen from the figure, the optical responses for the 2 nm and the 5 nm samples are quite similar. The 10 nm sample is the first to show a substantial change at lower wavelengths, but it is not until the 54 nm sample that large changes in the refractive index takes place. These four samples show the same trend of the refractive index dropping at lower wavelengths. However, the 137 nm sample shows a large change, with a peak now appearing at roughly 540 nm, this is indicative of a change in phase, as it is tending towards the optical response of bulk anatase TiO_2 [5].

XRD patterns did not show any peaks indicating that the films have not crystallized. However, given the response of the 137 nm sample and the diffraction patterns of the TEM, it is possible that there are crystallites forming but these are too small to be resolved by the TEM. M. M. Abd El-Raheem et al. [6] show the optical constants of amorphous TiO_2 at different thicknesses grown by a dc

sputtering technique, which show a similar trend over the thickness, which was attributed to the density of the TiO_2. Therefore, it is feasible that the change in optical response for the 2, 5 , 10 and 54 nm samples can be attributed to a change in density.
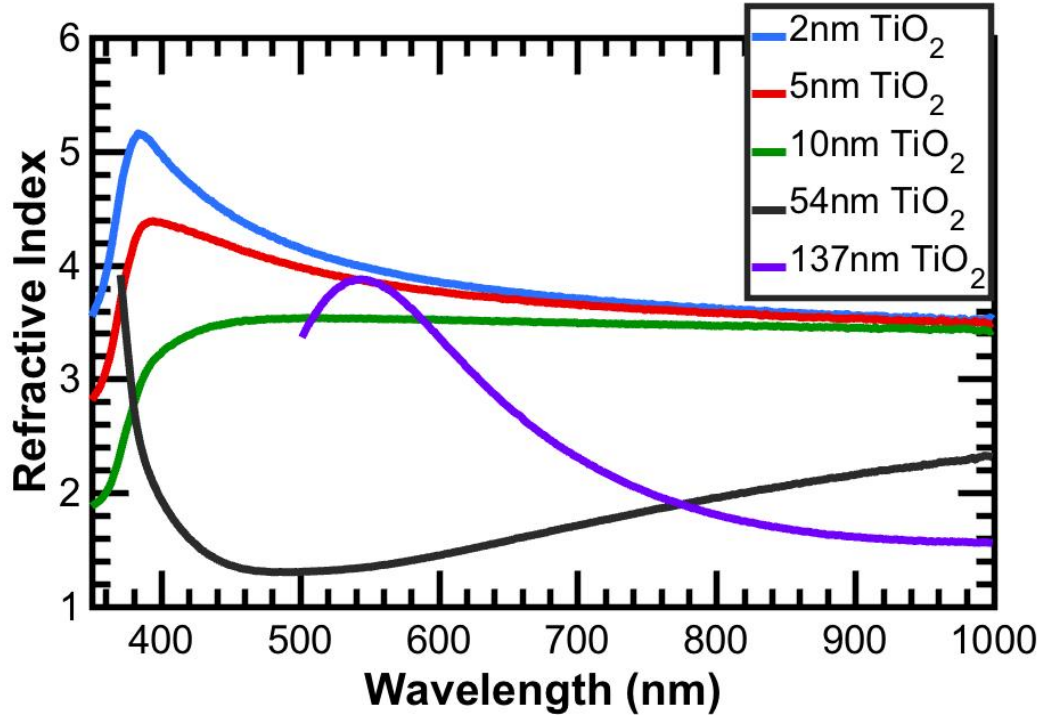
Figure 4.3: Refractive index of the samples over the spectral range, determined by SE.

Electrical Results

Figure 4.4 a) displays the current density versus voltage characteristics for the $Au/Ni/TiO_2/Si$ thickness series on p++ silicon. It exhibits an unexpected behaviour, where following an initial drop in the current density with increasing TiO_2 thickness, the thicker TiO_2 samples (10 nm) show a higher current density at a given gate voltage, for both positive and negative polarities. Figure 4.4 b) shows the current density at a gate voltage of -1V versus TiO_2 thickness. This atypical behaviour could be, in part, due to crystallites forming in the thicker TiO_2 samples, or could be due to the TiO_2 interacting with the SiO_2 as it gets thicker.

TEM diffraction patterns shown in figure 4.5 demonstrate evidence of
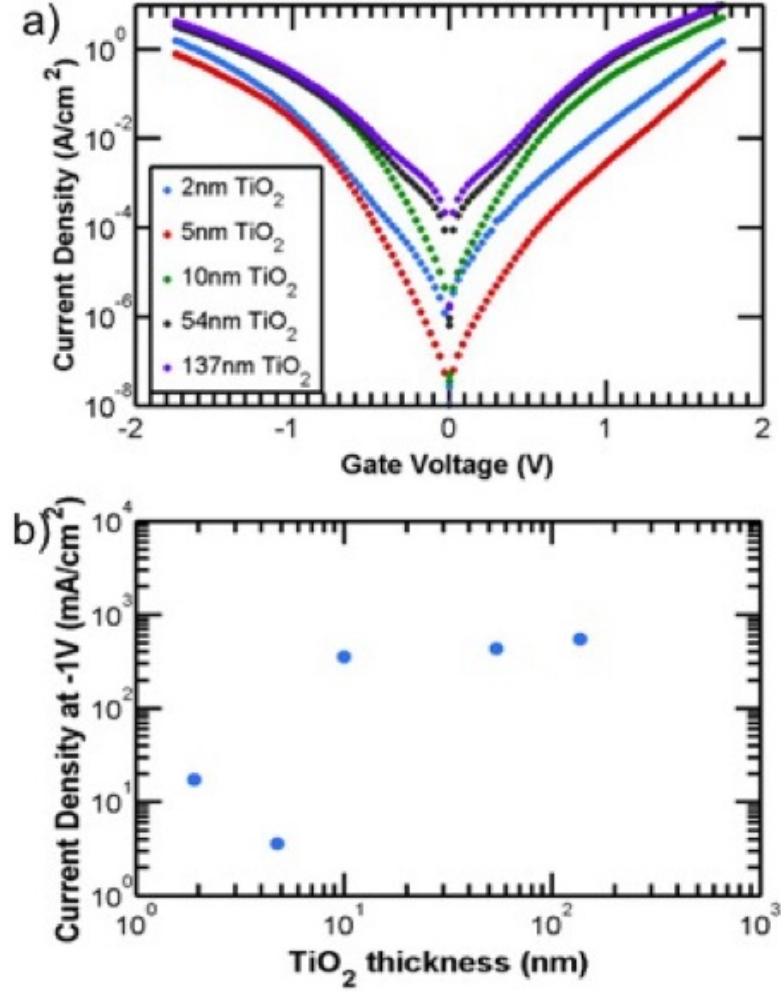
Figure 4.4: a) Current density-voltage characteristics of Au(150 nm) / Ni(70nm)/ x nm TiO$_2$ / p++ Si (in the dark). Sites of 50 μm × 50 μm up to 1000 μm × 1000 μm were measured (100 μm × 100 μm shown) and exhibited expected current scaling with gate area. b) Presents the current density at a gate voltage of -1V versus the actual TiO$_2$ thickness (TEM), illustrating the leakage current increasing with increasing TiO$_2$ thickness.

crystallinity in the samples with a TiO$_2$ thickness of 54 nm and 137 nm. Both anatase and rutile TiO$_2$ can fit the diffraction pattern albeit neither perfectly. Also seen in the diffraction pattern are spots due to the Si substrate. However, XRD (not shown), did not show any evidence of crystallinity. Within the error of TEM measurement the SiO$_2$ is the nominally the same thickness.

It has been shown in [7] that TiO$_2$, can perform oxygen scavenging from the SiO$_2$ layer. This can be deliberately done with a Ti layer, which when annealed scavenges oxygen from the SiO$_2$ layer creating TiO$_2$. However, as mentioned in
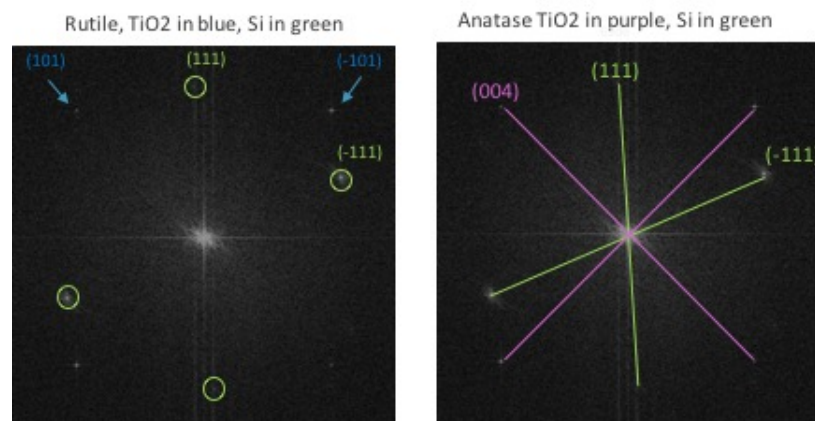
Figure 4.5: TEM diffraction patterns, from the two thickest TiO_2 growths. This gives some indication of crystallinity.

chapter 5, TiO_2 has a reasonably long nucleation regime at around 7 nm. When the TiO_2 moves into the bulk regime the TiO_2 close to the SiO_2 interface may well scavenge some oxygen from the SiO_2. It wouldn't be enough to change the thickness; however, it could change the SiO_2 layer to a SiO_x layer. This is unlikely, as although the amine-based precursor can self-clean and remove oxide, it is relatively less reactive to alkyl-based organometallics. The oxygen could also come from permeation of H_2O through the oxide whilst growing. Another possibility is a change in the film due to what is effectively a low temperature anneal while the film is growing. The thicker samples are exposed to an enhanced thermal budget by the simple fact that they are in the chamber longer.

Electrochemical Studies Figure 4.6 shows the cyclic voltammetry response of the samples in a solution of ferri/ferrocyanide (FFC), measured in the photoelectrochemical cell. The 2 nm of Ni on the TiO_2 surface acts as an oxygen evolution catalyst. The p++/Si samples are measured in the dark and the p+n Si samples are measured under AM1.5. As can be seen, there is increase of the peak-to-peak voltage as the TiO_2 gets thicker for the p++/Si reference samples in the dark, which would seem to indicate an increased resistance in the structure, contrary to the JV results.

However, when the samples are measured for the TiO_2/p+n/Si anode in the
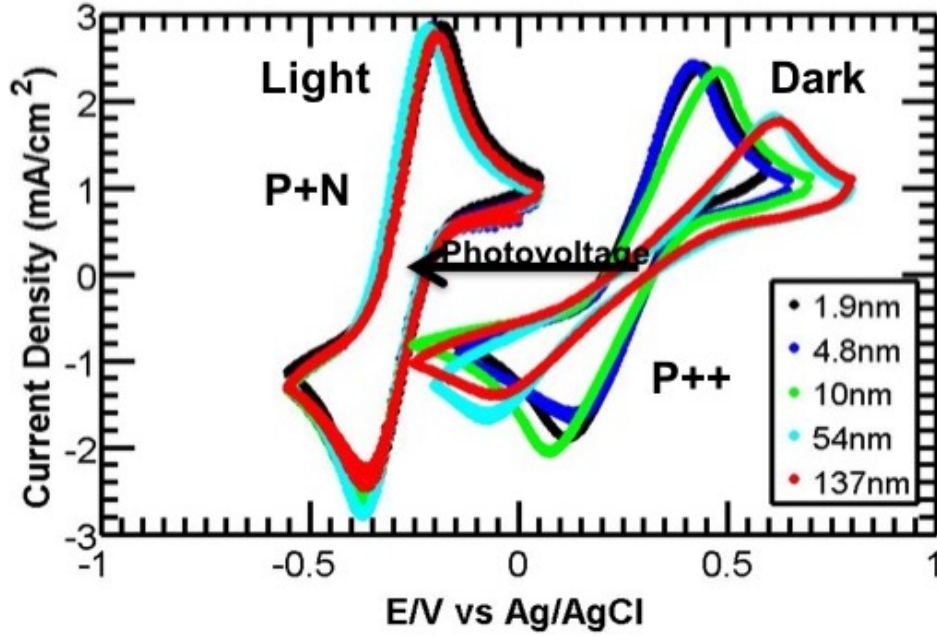
Figure 4.6: The cyclic voltammetry response for the Ni/TiO$_2$/SiO$_2$/p+n Si structures in the light (AM 1.5) and the reference Ni/TiO$_2$/SiO$_2$/p++ Si structures in the dark. Note the absence of any TiO$_2$ thickness dependence in the cyclic voltammetry responses of the p+/n structures measured in the light.

light, the FFC response does not change with the TiO$_2$ thickness, indicating that the TiO$_2$ resistance is not the limiting factor in this design of cell. One possibility was that the light was interacting with the TiO$_2$ films when they were measured under illumination. However, as can be seen in figure 4.7, when the p++ sample is measured in both with and without illumination, the result remains the same (this was tested for all thicknesses).

The photovoltage can be inferred by a comparison of the centre points of the p++/Si anode in the dark and the p+n Si MOS anodes in the light and yields a constant value of 0.55 V over the complete TiO$_2$ thickness range from 2 nm to 137 nm.

4.4   Discussion and Conclusions

In this work the thickness dependency of ALD grown TiO$_2$ was investigated in a MOS structure for water-splitting applications. Results contradictory to what
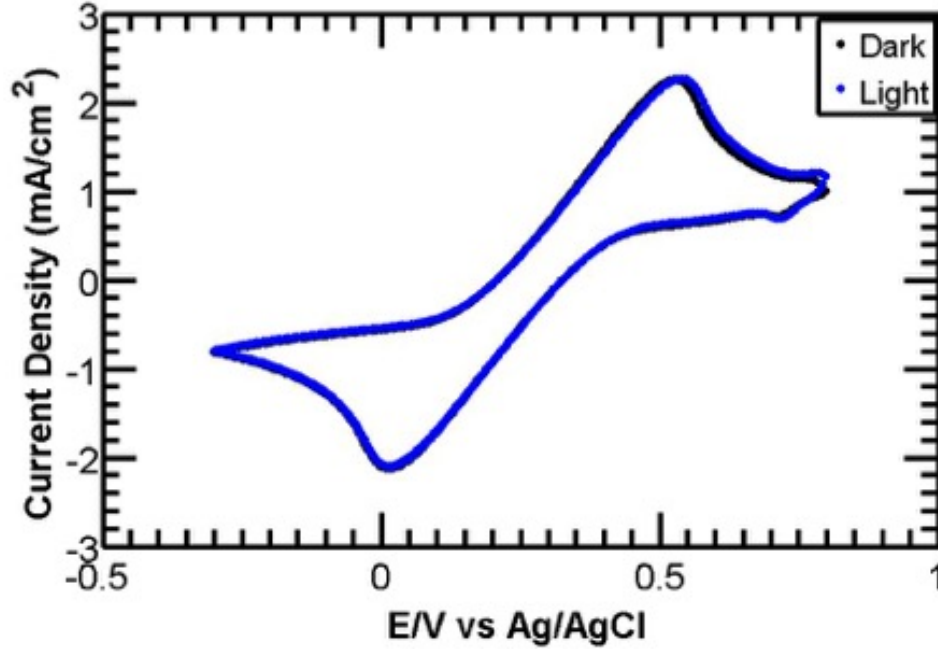
Figure 4.7: The cyclic voltammetry response for the Ni/10nm TiO_2/SiO_2/p++ Si structure in the light (AM 1.5) and in the dark, note there is no noticeable difference between the curves, indicating that the light does not affect the TiO_2 conductivity.

was expected were exhibited in the dark IV electrical experiments. As the TiO_2 thickness increased from 5 nm to 10 nm, the current density for a fixed bias increased. For a TiO_2 thickness > 10 nm the TiO_2 conductivity at a given bias is almost independent of thickness. Further investigation into the change in the film between the 5 nm and the 10 nm samples, where the current increase is the most substantial, should be performed, however there is a strong indication that the films are changing as they get thicker as indicated by the optical responses.

In the electrochemical experiments, the dark cyclic voltammetry shows a more expected result where the increased TiO_2 thickness results in an increased peak to peak voltage. However, the p+n Si anode does not see this increased peak to peak voltage. These structures exhibit a constant photovoltage of 0.55 V across the full TiO_2 thickness range. These results are technologically significant as they indicate that the TiO_2 surface protection layer can be increased in thickness to improve long term stability, without incurring a penalty of reduced photovoltage in the cell operation.

Due to the simplicity of the experiment, the dark IV electrical results should be the most accurate in determining the leakage of the TiO_2, however the difference between these results and the results from the electrochemical cell, indicate that the electrochemical results are influenced by other factors, which should be investigated further.

Bibliography

[1] Bassett, R. K. *To the digital age: Research labs, start-up companies, and the rise of MOS technology;* JHU Press: 2002.

[2] Chen, Y. W.; Prange, J. D.; Dühnen, S.; Park, Y.; Gunji, M.; Chidsey, C. E.; McIntyre, P. C. *Nature Materials* **2011,** *10,* 539–544.

[3] Hu, S.; Shaner, M. R.; Beardslee, J. A.; Lichterman, M.; Brunschwig, B. S.; Lewis, N. S. *Science* **2014,** *344,* 1005–1009.

[4] Wagner, C. D. *Handbook of X-ray photoelectron spectroscopy;* Perkin-Elmer: 1979.

[5] DeVore, J. R. *J. Opt. Soc. Am.* **1951,** *41,* 416–419.

[6] El-Raheem, M. A.; Al-Baradi, A. M. *International Journal of Physical Sciences* **2013,** *8,* 1570–1580.

[7] Satterthwaite, P. F.; Scheuermann, A. G.; Hurley, P. K.; Chidsey, C. E.; McIntyre, P. C. *ACS Applied Materials & Interfaces* **2016,** *8,* 13140–13149.

Chapter 5

A new method for ALD mixed oxide samples: A study into TiO_2 mixed oxides

5.1 Introduction

The study of improving the properties of an oxide, by adding other elements into the film to create either a mixed oxide or nanolaminate have been studied [1]. For example, a significant amount of research has been focused on improving HfO_2 device electrical properties. A number of different "additives" have been studied such as Al_2O_3, N and Si [2–8]. These additives have been incorporated using a number of different deposition methods such as metal organic chemical vapour deposition (MOCVD), physical vapour deposition (PVD), pulsed laser deposition (PLD) and atomic layer deposition (ALD) [5, 9–12]. ALD grown mixed oxides are in general grown by using alternate cycles [8, 13]. However, especially in case of a high ratio between the different cycles, the influence of the additive can be on the growth of the material rather than the incorporation of the additive into the film itself. In this study a new approach of creating a mixed oxide by ALD is shown, where each cycle contains both metal precursors. In this way the mixed oxide is created in each step of the ALD growth.

TiO_2 has been incorporated into many different composite films [1, 14], and extensively for photocatalytic and photovoltaic applications, with some electronics applications when TiO_2 has been incorporated into other oxides to improve their electrical properties.

TiO_2 exists in three crystalline forms, anatase, brookite and rutile [15, 16], with bulk rutile being the most thermodynamically stable. According to the phase diagram presented by Geraghty et al. in [17], the rutile phase is only formed above 800ºC, however both anatase and rutile have been seen in vacuum-deposited thin films [18–20], with anatase being the most prevalent for ALD grown TiO_2 [21].

Hwu et al. found that the preparation method heavily influenced the crystal structure of TiO_2 nanoparticles [22]. It has also been shown by Banfield et al. that TiO_2 with anatase and/or brookite microstructure, can be transformed to

rutile after reaching a certain particle size [23, 24].

TiO_2 can change phase by annealing. Hou et al. show that the resulting phase is dependent on the temperature, with anatase formation from amorphous, initiated at 300°C and is completed between 500°C and 700°C. Rutile TiO_2 is only formed when annealed at 900°C and above. [25].

Amorphous TiO_2 tends to have a lower dielectric constant and lower resistance than the crystalline phases [26, 27].

This study investigates the possibility of changing the TiO_2 leakage properties by creating a mixed oxide using a new ALD technique. It goes on to further investigate the influence of annealing the samples. The presence of the other metal atoms should influence how the TiO_2 crystallises, and therefore should demonstrate different electrical properties to the unannealed samples.

A number of different metals were used to try and influence the electrical properties of the TiO_2, based on their bonds strengths, ability to dope the TiO_2 and structure stresses caused by the difference in atom sizes. An assumption of larger atoms would stress the TiO_2 due to their atomic mass, and not using their effective ionic radii [28], as it is not clear how the atoms are being incorporated. Hafnium was incorporated as it is a larger atom than titanium and likely to cause structural stress when incorporated into the film. Tin was incorporated as it is a similar sized atom to titanium and bonds in the Sn^{4+} state, similar to titanium. Therefore, when tin is incorporated, the strength of the bonds should be the parameter changing. Aluminium should affect the TiO_2 in two different manners, firstly by doping the material, Al^{3+} vs. Ti^{4+} and also by being a smaller atom to titanium it should fit into the structure without much distortion. Zinc was used as it should again dope the material with Zn^{2+} vs Ti^{4+}. The range of the secondary oxides incorporated spans from wide band gap (7-8 eV) oxide Al_2O_3 to mid-range band gap oxide HfO_2 (around 5.9 eV) to semiconducting oxides ZnO and SnO_2. In this way a range of different possibilities were investigated.

119

5.2   Experimental

The substrates used were p-Si(100) (10-20 Ω.cm) wafers, which received an initial surface clean in a Semitool Spray Acid tool. Ozone, hot deionised water, NH_4OH and HF were used to remove particles, organic contaminants and metals from the wafer surface before oxidation.   Using the HF and ozone together simultaneously etches and regenerates the oxide on the surface. This treatment removes a thin layer of silicon around 0.8-1.0 nm and leaves a chemical passivation oxide around 1.5 nm thick on the wafer surface. First 350 cycles of TiO_2 films were deposited at 170^oC in a Picosun R200 ALD system using a thermal process. This was done to ensure that the TiO_2 was in the bulk growth regime and not the nucleation regime (achieving a nominal thickness of 12 nm). Therefore, any of the second metal precursor incorporated is due to the non-saturating titanium pulse and not due to non-stoichiometry effects present in the nucleation regime.   Next, 100 cycles of the mixed oxide films were deposited. To achieve this the Ti precursor was under-pulsed, leaving a number of reaction sites for the second metal precursor to react with. After the second metal precursor was pulsed, the cycle was finished off with a H_2O pulse, thereby creating a mixed oxide. The process is similar to the ALD growth of oxides such as HfSiOx, where the Hf and Si precursors are co-pulsed, i.e. both precursors are in the chamber at the same time. The difference now is that the precursors are not in the chamber at the same time, there is a purge between the metal precursors. Then the amount of the second metal precursor should be more controllable, however other mechanisms such as ligand exchange may also play a role.   The   titanium   precursor   used   for   the   deposition   is tetrakis(dimethylamidotitanium (TDMAT) $(Ti(N(CH_3)_2)_4)$ which was heated to 65^oC, the aluminium precursor was trimethylaluminium (TMA) $(Al(CH_3)_3)$ which   was   not   heated.   The   hafnium   precursor   was tetrakis(ethylmethylamino)hafnium (TEMAH) $(Hf(N(C_2H_5)(CH_3))_4)$ which was

heated to 85ºC, the zinc precursor was diethylzinc(DEZ) ($Zn(C_2H_5)_2$) which was not heated. The tin precursor was tetrakis(dimethylamido)tin (TDMASn) ($Sn(N(CH_3)_2)_4$) which was heated to 65ºC and H_2O which was not heated was used as the oxygen source for all the samples. The deposition thickness target for all the mixed oxide films was 5 nm +/- 0.5 nm. The Picosun R200 ALD system uses a boost function for precursors, whereby the precursor vessel is filled with the carrier gas (N_2) to maintain a constant pressure for each pulse. It is therefore possible to maintain the same sized pulse dose consistently. In order to under pulse the TDMAT and therefore leave reaction sites for the second metal precursor, for the first level of reduced TDMAT the pulse time was halved from 0.6 s to 0.3 s (from here referred to as SU - for small underpulse). For the second level of reduced TDMAT, the pulse time was reduced further to 0.1 s as well as reducing the carrier flow used for the boost from 600 sccm down to 300 sccm (from here referred to as LU - for large underpulse). There are a large number of settings that these values could be set to, allowing for a range of different ratios of metal precursors. These two different values were simply chosen to try and achieve a relatively high ratio and relatively low ratio of Ti to other metal. Due to the software on the ALD kit, the second metal precursor (if heated) has the same type of pulse as the TDMAT. For the SU sample this should not be an issue due to the pulse only being marginally scaled back, but in order to ensure enough of the second metal precursor had entered the chamber during the LU growth, the second metal precursor was double pulsed. The samples were split and annealed at two different temperatures, 300ºC and 500ºC, in air for 3 hours.

The film growth of the control TiO_2 sample was monitored by in-situ SE using a Woollam M2000D system with a spectral range of 193 nm to 998.9 nm operating in a dynamic capture mode. All SE analysis was performed using Woollam's CompleteEASE software. A Cauchy model was used to describe the TiO_2 films deposited by ALD in this study. The sample was given a stabilisation time of

40 minutes in the chamber, as it had been observed through the in-situ SE that this was required for the sample to reach thermal equilibrium. The measurement time was set to capture data every 1.6 seconds, which allowed for measurements to be taken during the titanium and oxygen purge times. The other samples were measured with the same system in the ex-situ set-up.

The samples are summarised in table 5.1. Samples are named as follows, Ux-y-z, where x is the other metal incorporated, y is given the value of 1 for the SU sample and 2 for the LU sample, and z is given the value of a or b, to indicate an anneal at 300°C or 500°C respectively.

For the electrical measurements, a metal-oxide-semiconductor (MOS) device was formed by evaporating 70 nm of Ni and 150 nm of Au, onto the mixed oxide using a mask that gives a range of capacitor sizes. The gate metals were deposited using a Temescal FC200 e-beam evaporation system which is evacuated to $< 5 \times 10^{-7}$ Torr. The Ni was evaporated at 0.3 nm/sec and the Au at 0.5 nm/sec. The evaporation took place in an unheated chamber. The samples were measured using an Agilent HP4156C analyser and an Agilent E4980 for IV and CV analysis respectively, in a Cascade semi-automatic microchamber. The reason for measuring the CV to determine the k value is because the k value will be important if the overall gate stack is not highly conductive. A more resistive gate structure results in a surface charge (Q_s) determined by the anode oxide capacitance. A fixed Q_s and fixed oxide field (E_{ox}) is needed for a fixed current. The DC current is proportional to the O_2 evolution rate in the photoelectrochemical cell, where $Q_s = C_{ox}V$. Therefore, an additional V needed to achieved a given Q_s is $dV = dQ_s/C_{ox} = qQ_s \cdot T_{ox}/(\varepsilon_0 \, \varepsilon_{ox})$. Therefore, a higher ε_{ox} helps to reduce the overpotentials, as described in [29]

X-ray photoelectron spectroscopy (XPS) analysis was performed in order to obtain the elemental composition of the TiO_2 films. First the samples were sputtered with an Argon Gas Cluster source (10 keV, Ar1000+ clusters) for 3 s

Table 5.1: Sample Table

Sample Name	TDMAT pulse	TDMAT Carrier Flow	TDMAT purge	Boost Flow	Other Metal	Other Metal Carrier Flow	Anneal Conditions
UTi-1	0.5	80 sccm	30s	600 sccm	NA	NA	NA
UTi-1-a	0.5	80 sccm	30s	600 sccm	NA	NA	300°C - 3 hours
UTi-1-b	0.5	80 sccm	30s	600 sccm	NA	NA	500°C - 3 hours
UAl-1	0.3	80 sccm	30s	600 sccm	Al	150 sccm	NA
UAl-1-a	0.3	80 sccm	30s	600 sccm	Al	150 sccm	300°C - 3 hours
UAl-1-b	0.3	80 sccm	30s	600 sccm	Al	150 sccm	500°C - 3 hours
UAl-2	0.1	80 sccm	30s	300 sccm	Al	150 sccm	NA
UAl-2-a	0.1	80 sccm	30s	300 sccm	Al	150 sccm	300°C - 3 hours
UAl-2-b	0.1	80 sccm	30s	300 sccm	Al	150 sccm	500°C - 3 hours
UHf-1	0.3	80 sccm	30s	600 sccm	Hf	80 sccm	NA
UHf-1-a	0.3	80 sccm	30s	600 sccm	Hf	80 sccm	300°C - 3 hours
UHf-1-b	0.3	80 sccm	30s	600 sccm	Hf	80 sccm	500°C - 3 hours
UHf-2	0.1	80 sccm	30s	300 sccm	Hf	80 sccm	NA
UHf-2-a	0.1	80 sccm	30s	300 sccm	Hf	80 sccm	300°C - 3 hours
UHf-2-b	0.1	80 sccm	30s	300 sccm	Hf	80 sccm	500°C - 3 hours
USn-1	0.3	80 sccm	30s	600 sccm	Sn	80 sccm	NA
USn-1-a	0.3	80 sccm	30s	600 sccm	Sn	80 sccm	300°C - 3 hours
USn-1-b	0.3	80 sccm	30s	600 sccm	Sn	80 sccm	500°C - 3 hours
USn-2	0.1	80 sccm	30s	300 sccm	Sn	80 sccm	NA
USn-2-a	0.1	80 sccm	30s	300 sccm	Sn	80 sccm	300°C - 3 hours
USn-2-b	0.1	80 sccm	30s	300 sccm	Sn	80 sccm	500°C - 3 hours
UZn-1	0.3	80 sccm	30s	600 sccm	Zn	150 sccm	NA
UZn-1-a	0.3	80 sccm	30s	600 sccm	Zn	150 sccm	300°C - 3 hours
UZn-1-b	0.3	80 sccm	30s	600 sccm	Zn	150 sccm	500°C - 3 hours
UZn-2	0.1	80 sccm	30s	300 sccm	Zn	150 sccm	NA
UZn-2-a	0.1	80 sccm	30s	300 sccm	Zn	150 sccm	300°C - 3 hours
UZn-2-b	0.1	80 sccm	30s	300 sccm	Zn	150 sccm	500°C - 3 hours

in order to remove the carbon over layer. Then high-resolution X-ray photoelectron spectra were recorded by using a Kratos AXIS instrument with a monochromatic Al Kα radiation of 1486.6 eV energy as the excitation source (10 mA, 15 kV). All spectra were acquired with analyser pass energy of 20 eV and 100 ms dwell time per step. Binding energy values were calibrated by employing the C 1s 284.80 eV. Mixed Gaussian-Lorentzian functions and Shirley-type backgrounds were used for reconstruction and fitting of the high-resolution spectra.

5.3   Results and Discussion

5.3.1   Film Growth and Properties

TEM

ALD of TiO_2 has been shown to grow good quality, pin-hole free films, with good saturation and linearity [21]. The surface chemistry and chemical composition in both amorphous and crystalline phases have been also studied [30]. In this work changing the electrical properties of TiO_2 by creating a $Ti_xA_{1-x}O_2$ film was investigated, where x is less than 1 and A is the second metal atom.

The thickness of the UTi-1 sample and the UTi-1-b samples were confirmed by TEM, shown in figure 5.1. After annealing at 500°C however, the thicknesses of both the SiO_2 and the TiO_2 were affected. This may be due to the film restructuring with crystallites.

Spectroscopic Ellipsometry

The thickness of the films was determined by SE. Figure 5.2, show the time resolved data for the TiO_2 control sample UTi-1. It shows two regions of the growth, the first shows the first 350 cycles of the TiO_2 growth, the second stage
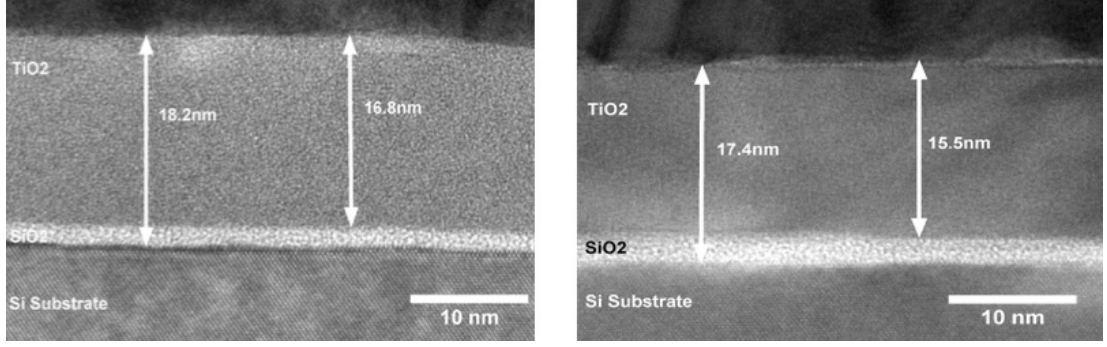
Figure 5.1: TEM Images showing the thickness of Left) UTi-1 and Right) UTi-1-b. The TiO$_2$ reduces in thickness from 16.8 nm to 15.5 nm, while the SiO$_2$ increases from 1.4 nm to 1.9 nm. This growth rate is slightly less than the nominal 17 nm (12 nm TiO$_2$ buffer + 5 nm layer).

are the next 100 cycles, this stage of the growth includes a longer purge time, this was to align with longer purge times used during the mixed oxide growths.

Figure 5.3 shows the refractive index plots of the different mixed oxide samples. The thickness of the layers was determined to be 8.14 nm, 8.18 nm, 6.13 nm, 6.54 nm, 4.15 nm, 4.10, 4.51 nm, and 4.55 nm for the samples UTAl-1, UTAl-2, UTHf-1, UTHf-2, UTZn-1, UTZn-2, UTSn-1 and UTSn-2 respectively, with all films having a TiO$_2$ buffer layer of 11.8 nm ± 0.1 nm.
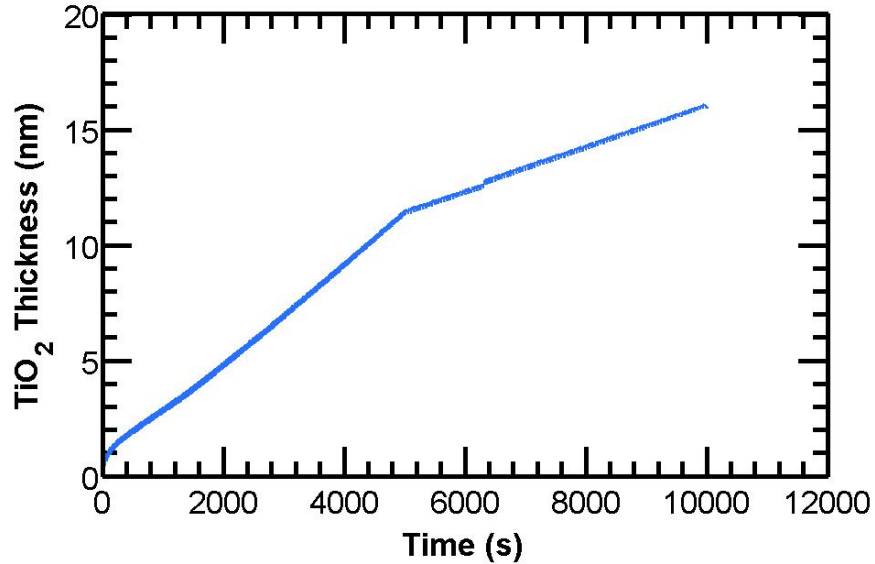
Figure 5.2: In-situ SE data from UTi-1 the TiO$_2$ control samples. Showing the step-wise nature of ALD, during the plasma growth.

The high level of incorporation of the Al seems to result in a much film than

125
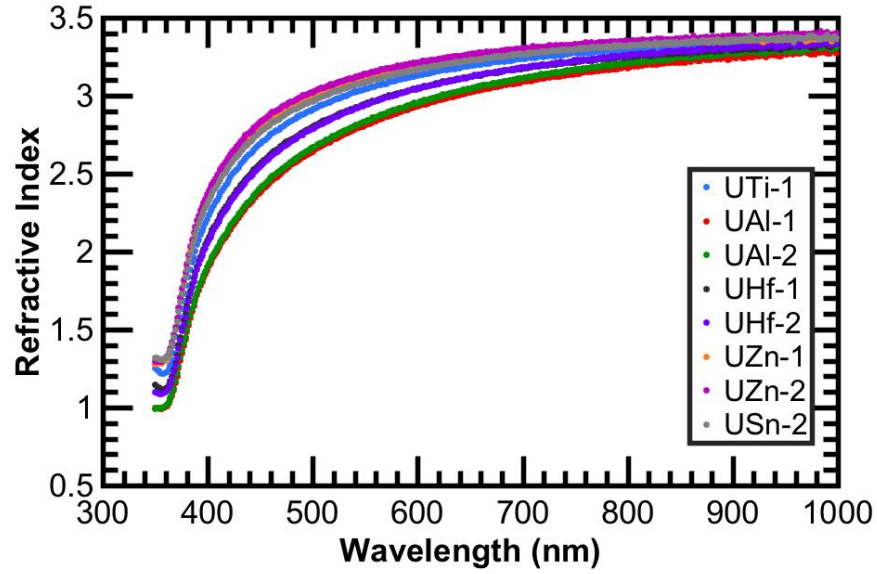
Figure 5.3: Refractive index of the samples over the spectral range, determined by SE.

the other samples. The increased thickness of the Hf mixed oxides are likely thicker due to the increased size of the Hf atom over the Ti atom.

X-ray photoelectron spectroscopy The film composition was determined using X-ray photoelectron spectroscopy. Table 3.2 lists the residual carbon and nitrogen contents of the films. Also listed is the ratio of Ti^{3+} to Ti^{4+} and the percentage incorporation of the second metal. The XPS results are discussed further below.

Table 5.2: XPS results detailing the percentage concentration of the Ti^{3+}, the Ti^{4+}, the second metal and the nitrogen and carbon contents

Sample	Ti %conc	Ti 3+	Ti 4+	Ti3+/Ti4+	O %conc	Oxide	O from Organics	Other Metal O %conc	C1s %conc	N1s %conc
UTi-1	28.3	4.4	24	0.18	61.9	55	6.9	NA	9.3	0.6
UTi-1-b	29.9	3.8	26.2	0.15	66.3	53.6	12.7	NA	3.5	0.2
UAl-1	17	3.7	13.2	0.28	60	53.4	6.7	17.9	4.9	0.3
UAl-2	18.3	5.7	12.6	0.45	60.7	52.4	8.3	18	2.8	0.3
UHf-1	25.5	5.3	20.2	0.26	62.9	56	7	5.3	6.1	0.2
UHf-2	24.2	5.7	18.4	0.31	64.2	57.5	6.7	6.9	4.6	0.1
USn-1	25	3.3	21.7	0.15	61.2	53.4	7.8	7	6.5	0.3
USn-2	25.8	3	22.9	0.13	61.4	55.1	6.3	7.3	5.2	0.3
UZn-1	25.3	5.2	20.1	0.26	62.3	55.4	6.9	7.4	4.5	0.5
UZn-2	23.8	4.3	19.5	0.22	61	54.1	6.9	8	6.8	0.4

126

5.3.2 Electrical Properties - Pre-Anneal

The electrical conductivity was measured by applying a voltage sweep to the gate electrode of the $Au/Ni/TiO_x/SiO_2/Si$ MOS structure. The voltage was swept from 0 to +/-1.5 V, in 0.015 V steps. Figure 5.4 shows the leakage current density against electric field for the different samples, against the TiO_2 control sample UTi-1. In this study the main voltage range of interest is the negative bias, therefore unless explicitly mentioned the current discussed is this current, when the device is negatively biased.
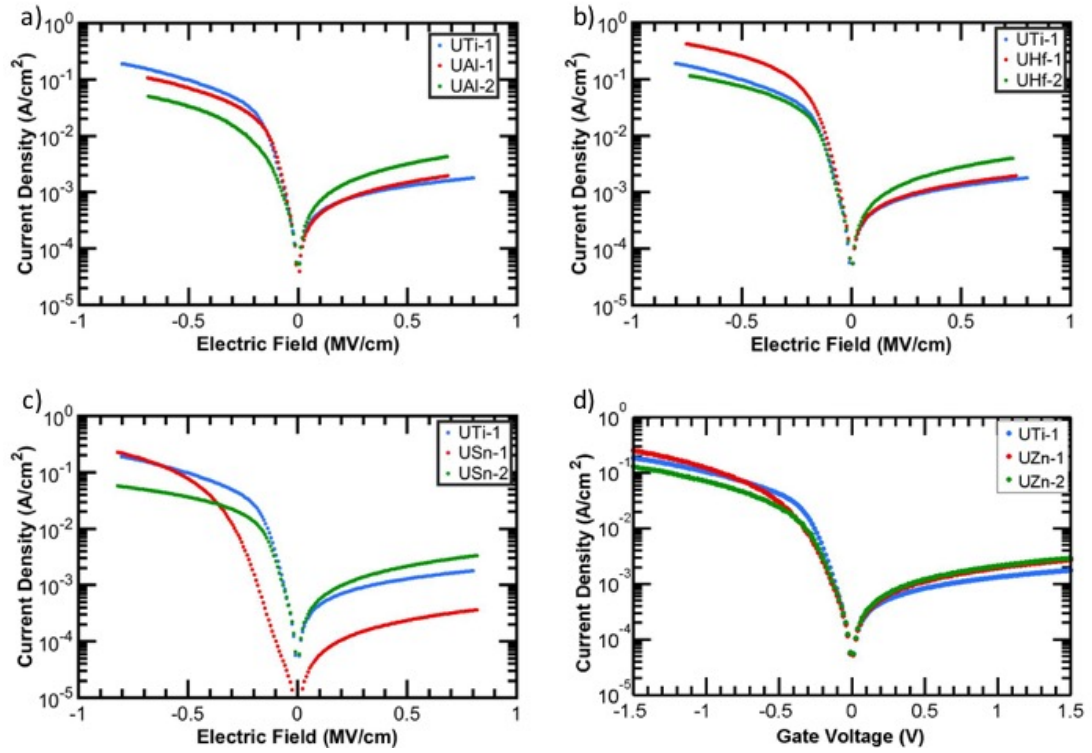
Figure 5.4: JV Sweeps of the different mixed oxide samples. Where UTi-1 is the control sample and the incorporation of the second metal is as follows: UAl-1 = 17.9%; UAl-2 = 18%; UHf-1 = 5.3%; UHf-2 = 6.9%; USn-1 = 7%; USn-2 = 7.3%; UZn-1 = 7.4%; UZn-2 = 8%.

CV measurements were undertaken to find approximate k values of the mixed oxides (see section 1.4.3) however it is difficult to determine exact k values without a full HRTEM analysis and due to the complexity of the structure. For the CV measurements, the voltage was swept from +1 V (depletion) to -4 V (accumulation) in CP-G mode. A number of checks were

completed to ensure that the device was not being stressed, such as measuring the same device multiple times to ensure there was no shift in the flatband voltage (V_{fb}), and measuring multiple devices again to note any variation across the wafer. It was also noted from the room temperature CVs that the leakage current was very high and it was therefore difficult to determine C_{max}. In order to combat this, measurements were done at -50°C, and on the 20 μm × 20 μm MOS capacitors. Although this increased the impedance, an estimated k value was determined from the C_{max}, using the lowest frequency at which the sweeps converge and by assuming the thickness to be 5 nm. Figure 5.5 shows CV measurements of the 9 samples. The approximate k values of the mixed oxide were calculated by assuming that the oxide could be modelled as three capacitors in series, i.e. the mixed oxide (5 nm), TiO_2 buffer layer (12 nm) and the SiO_2 layer (1.5 nm). The k value of the TiO_2 layer was calculated from the UTi-1, with the UTi-1 sample being the same thickness as the mixed oxide samples.

Al-TiO$_x$ Both AlTiO$_x$ oxides show a decrease in leakage current, with a large difference between the samples. This is most likely due to the resistive nature of Al_2O_3. XPS shows that there is a large incorporation of Al_2O_3 into the film at 17.9 and 18 percent, for SU and LU samples respectively. The incorporation of the Al_2O_3 has a strong influence on the state of the Ti, where the percentage concentration of the Ti^{4+} state has been reduced to 13.2% and 12.6% from 24% respectively, giving a Ti^{3+} to Ti^{4+} ratio for 0.14 and 0.45 respectively. Comparing the CV sweeps for the two samples, it can be seen that there is a difference in the C_{max} with UAl-2 having a higher C_{max} than UAl-1. This would indicate that the lattice of the UAl-2 sample is in a more stable state than the UAl-1 sample.

Hf-TiO$_x$ UHf-1 shows an increase of current over TiO_2. UHf-2 reduces again to below the UTi-1 level. Comparing the CV of the two Hf samples shows some interesting results. First the C_{max} values from 500kHz and up have increased, indicating that UHf-2 likely has a higher k value than UHf-1. Also, the shoulder
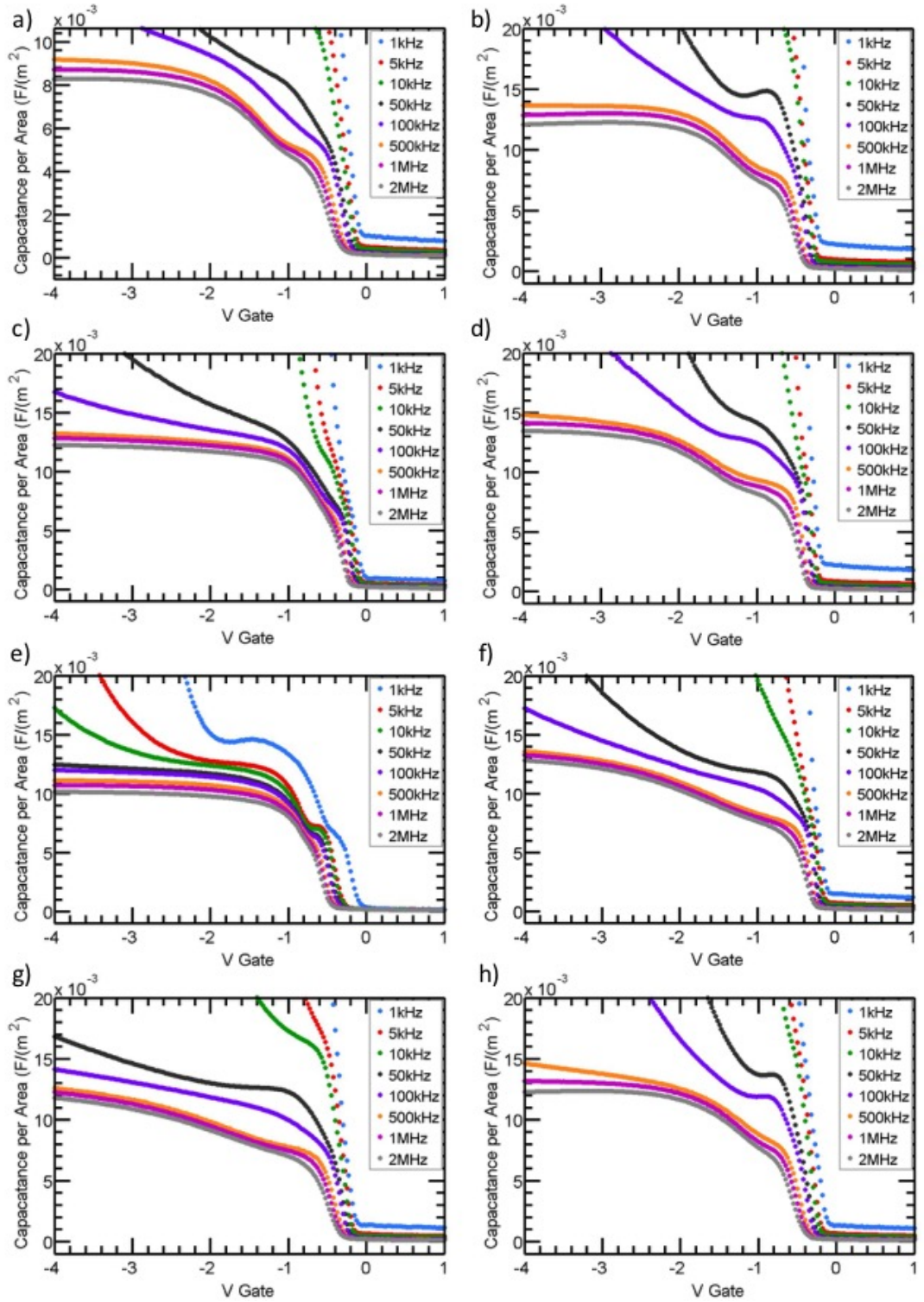
Figure 5.5: CV Sweeps of a) UAl-1, b) UAl-2, c) UHf-1, d) UHf-2, e)USn-1, f) USn-2, g) UZn-1, h) UZn-2. The k value can be calculated from C_{max}. Where UTi-1 is the control sample and the incorporation of the second metal is as follows: UAl-1 = 17.9%; UAl-2 = 18%; UHf-1 = 5.3%; UHf-2 = 6.9%; USn-1 = 7%; USn-2 = 7.3%; UZn-1 = 7.4%; UZn-2 = 8%.

at -0.5 V reduced in magnitude. One possible explanation for UHf-1 having an increased current density and reduced C_{max} is that at first the included Hf atoms are straining the TiO_2 lattice. Then, as more Hf is incorporated in UHf-2, the lattice structure moves to a more relaxed state. The k value of a material is heavily dependent on the lattice structure, in terms of crystallites and any stresses. UHf-1 has 5.3% concentration of HfO_2 while UHf-2 has 6.9%.

Sn-TiO$_x$ USn-1 shows the largest difference in the IV between 0 to -0.5 V and on the positive bias. It is difficult to draw conclusions as to why this is the case. For the CV measurements, the USn-1 sample shows some interesting effects. Firstly, there is a much broader frequency dispersion of the C_{max}. Secondly each frequency sweep reaches its C_{max} at a much lower bias, around -1.2 V, vs around -3 V for USn-2. XPS shows that the LU sample only has 0.3% more SnO_x incorporated than the SU sample and the LU sample also has a marginal larger amount of Ti.

Zn-TiO$_x$ Sample UZn-1 shows an increase in current compared to the control sample with a similar trend to the UHf samples, where the current initially increases but then drops off again as more Zn is incorporated. This is likely due to stresses in the film. Similar observations were made from data obtained from the UHf samples. Again, the XPS shows the LU sample as having a slightly higher incorporation of ZnO than the SU sample at 8% vs 7.4%. Again, it is difficult to draw much information from the CV sweeps.

5.3.3   Electrical Properties - Post Anneal

TiO$_2$ Figure 5.6 shows the JV sweeps for the control TiO_2 samples and samples unannealed, annealed at 300°C for 3 hours and annealed at 500°C for 3 hours. It is clear that annealing at 300°C has an effect on the conduction, however this could be due to oxygen scavenging making a more stoichiometric layer, or a change in the crystal structure, or a change in the SiO_2 layer.
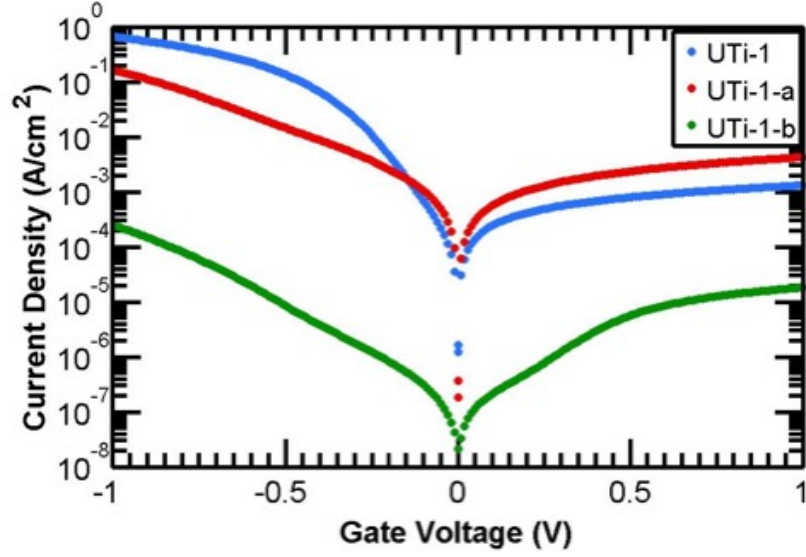
Figure 5.6: JV Sweeps of the TiO_2 control sample UTi-1, the JV of the sample when it is annealed at 300°C for 3 hours, UTi-1-a and the JV of the sample when it is annealed at 500°C for 3 hours UTi-1-b.

The sample annealed at 500°C for 3 hours shows a much larger decrease in current and is more likely due to a structural change. There is some evidence of this from the CVs, shown in figure 5.7. Unannealed TiO_2 has a k value of 75, which drops to 28.5 for UTi-1-a. It is difficult to extract a k value for UTi-1-b due to the large frequency dispersion. Comparing the XPS for the two samples, only the carbon content has significantly changed after anneal dropping from 9.3% to 3.5%. Although carbon is a known dopant for TiO_2 [31,32], the similarities of the XPS suggest that there are structural differences between the two samples.
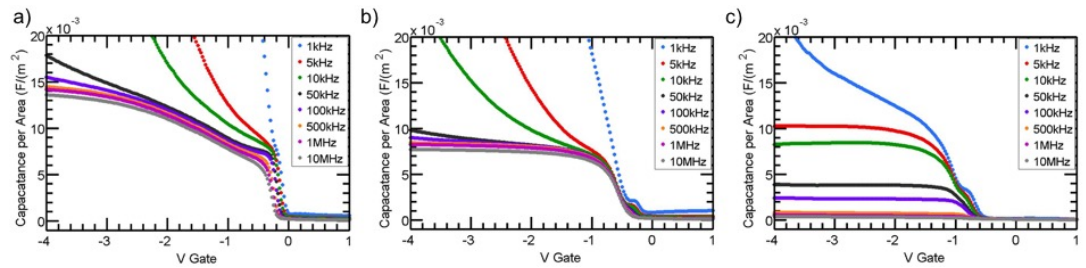
Figure 5.7: CV Sweeps of a) UTi-1, b) UTi-1-a (300°C anneal), and c) UTi-1-b (300°C anneal).

Current-voltage and capacitance-voltage measurements were also undertaken for the mixed oxide annealed samples.

Al-TiO$_2$ Figure 5.8 shows the JV sweeps for the Al-TiO_2 mixed oxide. The

samples annealed at 300°C show a marginal change on the negative bias, however on with positive bias a large increase in current is produced. This is further evidenced with the samples annealed at 500°C. This is an interesting result where the current on the positive bias is higher than on the negative. This behaviour also appears in the CV response, figure 5.8. The CV is inverted at zero volts, therefore there is an inversion region in the area around the metal gate defining the capacitor. The leads to an ac (low frequency) inversion response in the CV [33].

Figure 5.8: JV Sweeps of the Al-TiO$_2$ mixed oxide sample a) UAl-1 and b) UAl-2, with the corresponding JVs of the samples when they are annealed at 300°C for 3 hours at 500°C for 3 hours.

In this case it is difficult to obtain CVs and therefore k values, especially for the samples annealed at 300°C, as the samples are in a transition period. An example CV is shown in figure 5.9.
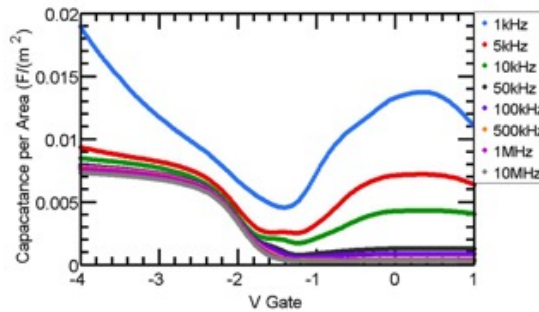
Figure 5.9: CV Sweeps of UAl-1-a, showing strange behaviour on the depletion side.

Hf-TiO$_2$ Figure 5.10 shows the leakage currents for the UHf samples. Again, the current drops after annealing, and for the UHf-1-b sample, the current for

the positive gate bias increases. This combined with the CV response shows the sample has switched to a NMOS. CVs of UHf-1-a and UHf-1-b are shown in figure 5.11. This switching from PMOS to NMOS has been seen by Castaldini et al., due to acceptor deactivation at the surface due to boron passivation by an impurity [34]

Figure 5.10: JV Sweeps of the Hf-TiO$_2$ mixed oxide sample a) UHf-1 and b) UHf-2, with the corresponding JV's of the samples when they are annealed at 300°C for 3 hours (UHf-x-a) and at 500°C for 3 hours (UHf-x-b).
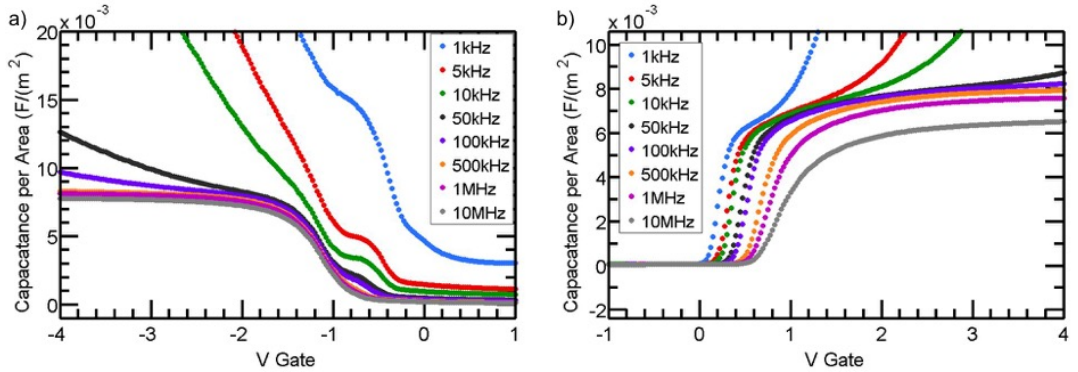
Figure 5.11: CV Sweeps of UHf-1-a and UHf-1-b. UHf-1-b showing a switch to NMOS from PMOS.

In relation to other samples annealed at 500°C UHf-2-b remains much more conductive with negative bias, being an order of magnitude higher than UHf-1-b.

Sn-TiO$_2$ Figure 5.12 shows the leakage current for the USn samples. These samples show the largest difference in terms of leakage current of all the samples. In figure 5.12 a) the blue box indicates the part of the graph that is below the resolution of the analyser. The sweep data is still smooth except for the area
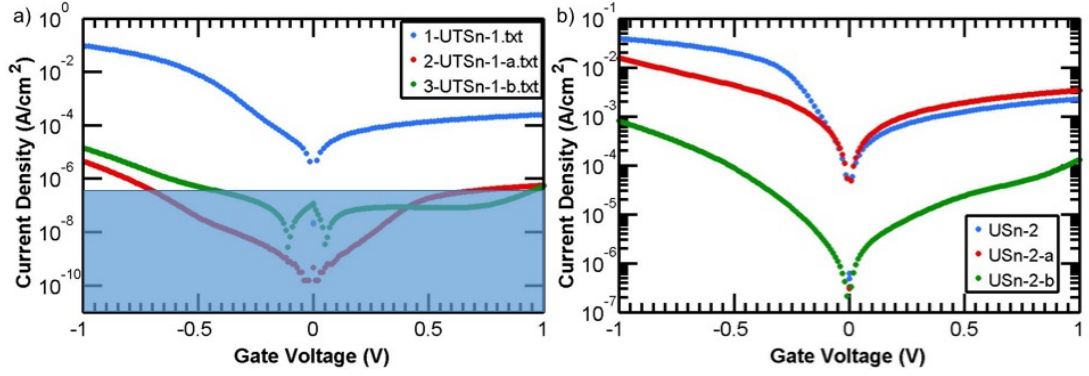
Figure 5.12: JV Sweeps of the Sn-TiO$_2$ mixed oxide sample a) USn-1 and b) USn-2, with the corresponding JVs of the samples when they are annealed at 300°C for 3 hours at 500°C for 3 hours.

around 0 V where strange behaviour is seen. It was possible however to get CV analysis on 3 of the Sn samples as shown in figure 5.13, where a) is USn-1-a, b) is USn-1-b and c) is USn-2-a.
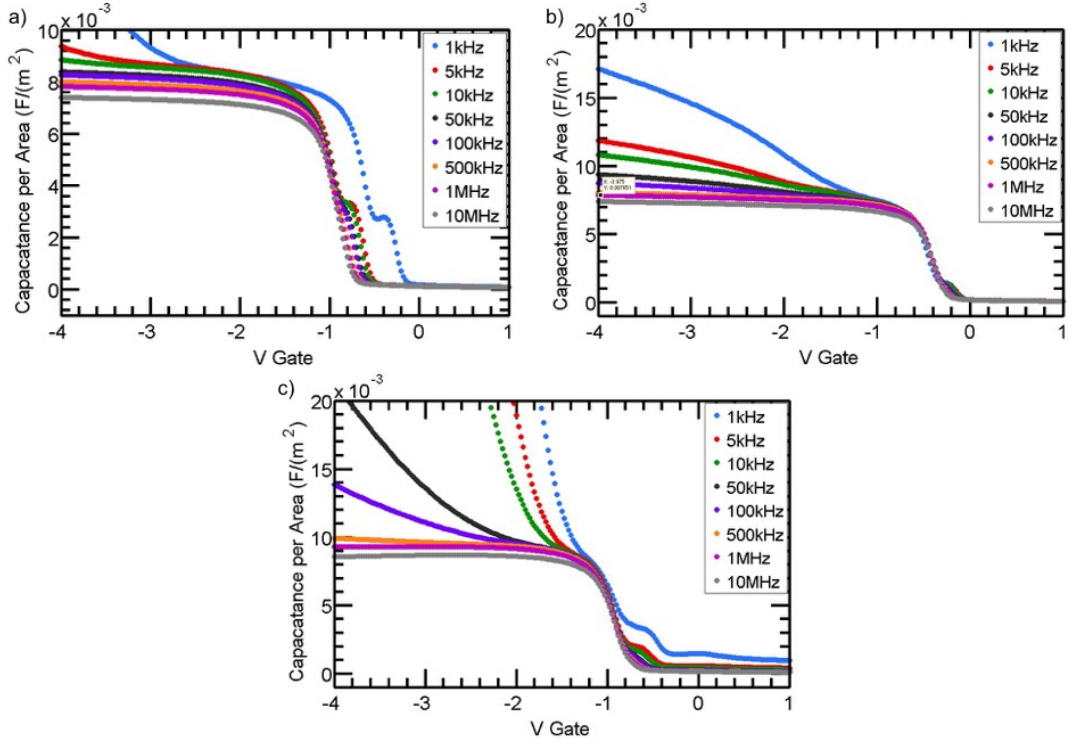
Figure 5.13: CV Sweeps of a) USn-1-a, b) USn-1-b and c) USn-2-a.

Zn-TiO$_2$ Figure 5.14 shows the leakage current for the UZn samples. Especially with UZn-2 there is very little in the difference between the two annealed samples. In comparison to the control sample, the Zn mixed oxide when annealed, resulted in a higher current than the control sample when annealed. Figure 5.15 shows

CVs for samples UZn-1-a, UZn-1-b, UZn-2-a, and UZn-2-b respectively.

5.4   Conclusions and Future work

In this work mixed oxide films were grown by ALD using a new method of underpulsing the titanium precursor, in order to leave reaction sites available for the second metal to react with. In all films the second metal was incorporated at two different concentration levels (except for the Al-TiO$_2$ films).

An investigation into how the incorporated metal changed the electrical properties was undertaken. For the current-voltage characteristics, the mixed oxides showed a changed leakage current. In particular, the Hf-TiO$_2$ sample UHf-1 showed the largest increase in leakage current. This result is of particular interest for water splitting applications, as increasing the current through the protective oxide, increases the performance of the photoelectrochemical cell. A further study optimizing the ratio of the two metals was performed to gain the greatest increase in leakage current. Subsequently the optimal film was characterised in a water splitting cell. As part of this study, an investigation into the current conduction mechanism should be undertaken in order to ascertain how the second metal aids conduction.

The electrical properties were further investigated in terms of the capacitance. It is difficult to draw strong conclusions from the capacitance voltage measurements, due to the structure of the samples.

An anneal study was then performed. Current-voltage characteristics follow a general trend of reduced leakage current with increasing annealing temperature. This result does not offer any benefit for water splitting applications but may offer some benefit for other solar applications where annealing is used in the processing.
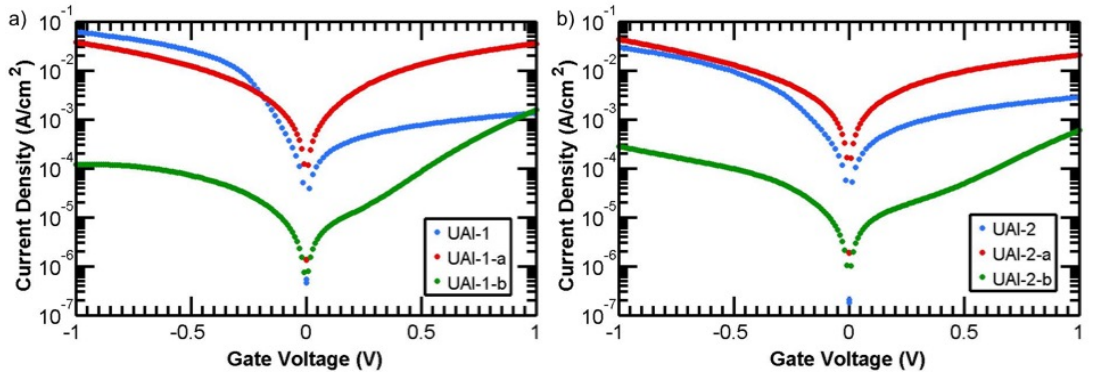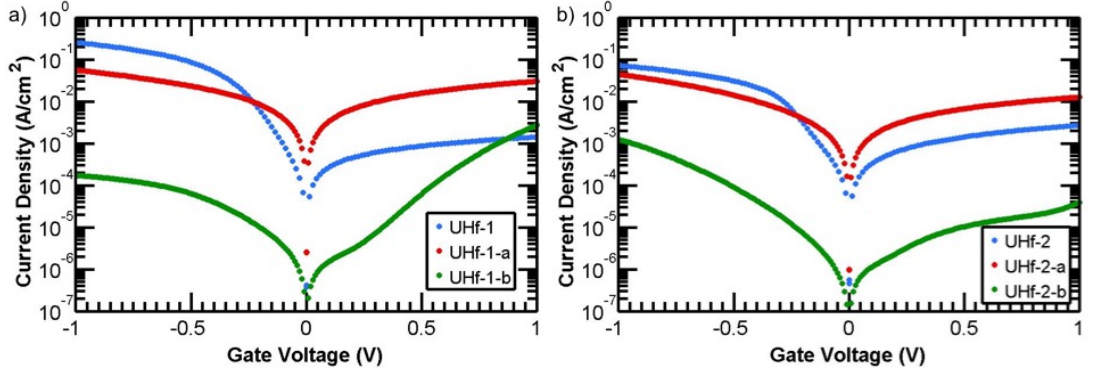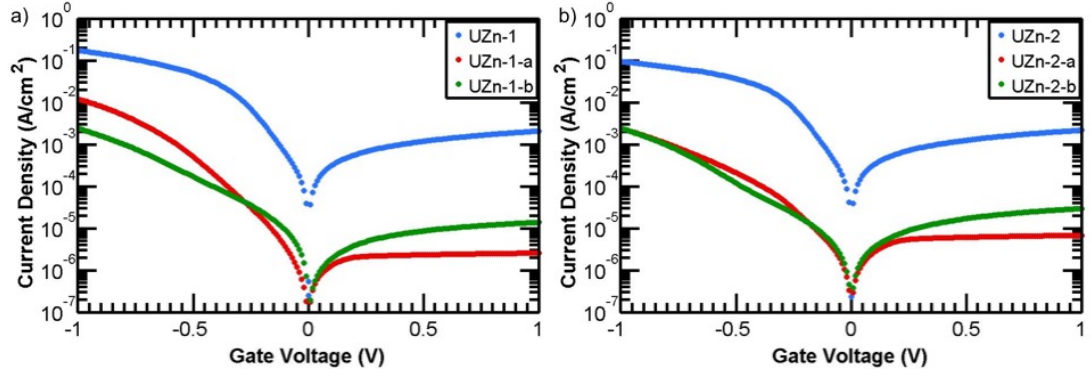
Figure 5.14: JV Sweeps of the Zn-TiO$_2$ mixed oxide sample a) UZn-1 and b) UZn-2, with the corresponding JV's of the samples when they are annealed at 300°C for 3 hours at 500°C for 3 hours.
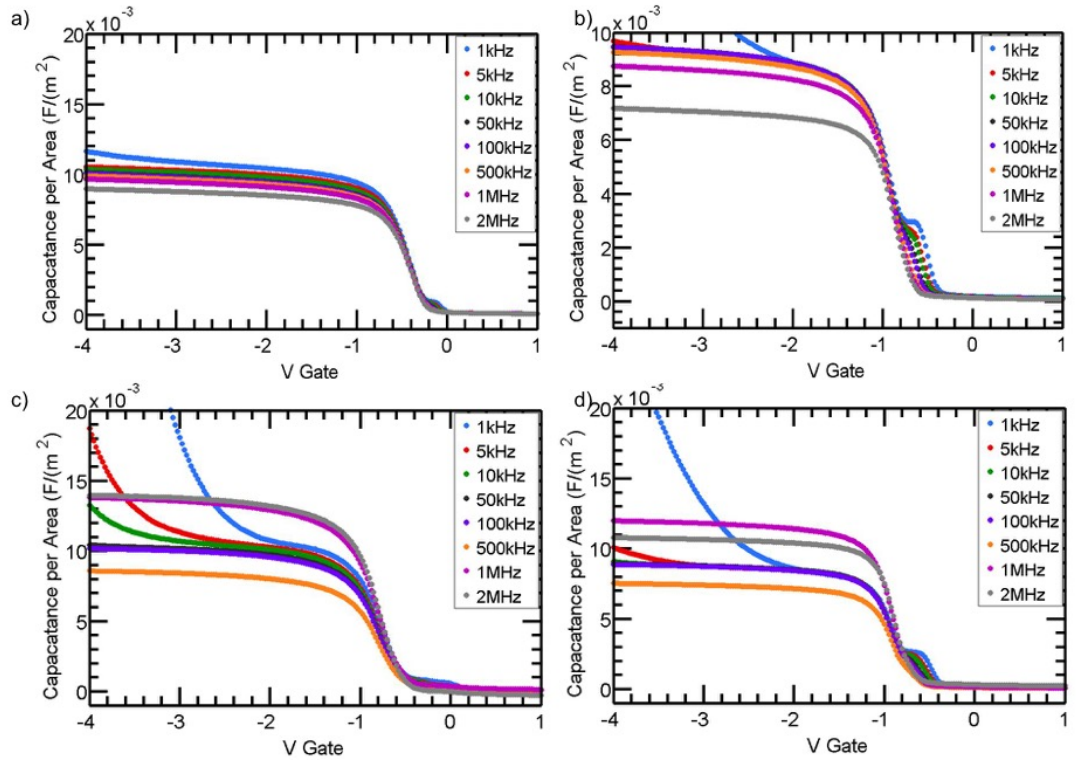

Figure 5.15: CV Sweeps of a) UZn-1-a, b) UZn-1-b, c) UZn-2-a and d) UZn-2-b.

Bibliography

[1] Dahl, M.; Liu, Y.; Yin, Y. *Chemical Reviews* **2014,** *114,* 9853–9889.

[2] Wilk, G.; Wallace, R.; Anthony, J. *Journal of Applied Physics* **2000,** *87,* 484–492.

[3] Choi, C.; Jeon, T.; Clark, R.; Kwong, D. *IEEE Electron Device Letters* **2003,** *24,* 215–217.

[4] Ho, M.-Y. *et al. Applied Physics Letters* **2002,** *81,* 4218–4220.

[5] Chen, F.; Bin, X.; Hella, C.; Shi, X.; Gladfelter, W.; Campbell, S. *Microelectronic Engineering* **2004,** *72,* 263–266.

[6] Kukli, K.; Ritala, M.; Leskelä, M.; Sajavaara, T.; Keinonen, J.; Gilmer, D. C.; Tobin, P. J. *Materials Science and Engineering: B* **2004,** *109,* 2–5.

[7] Kukli, K.; Ritala, M.; Leskelä, M.; Sundqvist, J.; Oberbeck, L.; Heitmann, J.; Schröder, U.; Aarik, J.; Aidla, A. *Thin Solid Films* **2007,** *515,* 6447–6451.

[8] Triyoso, D.; Hegde, R.; Wang, X.-D.; Stoker, M.; Rai, R.; Ramon, M.; White, B.; Tobin, P. *Journal of The Electrochemical Society* **2006,** *153,* G834–G839.

[9] Paskaleva, A.; Bauer, A.; Lemberger, M.; Zürcher, S. *Journal of Applied Physics* **2004,** *95,* 5583–5590.

[10] Honda, K.; Sakai, A.; Sakashita, M.; Ikeda, H.; Zaima, S.; Yasuda, Y. *Japanese Journal of Applied Physics* **2004,** *43,* 1571.

[11] Triyoso, D. *et al. Journal of Applied Physics* **2005,** *98,* 054104.

[12] Lu, N.; Li, H.-J.; Gardner, M.; Wickramanayaka, S.; Kwong, D.-L. *IEEE Electron Device Letters* **2005,** *26,* 298–300.

[13] Elam, J.; George, S. *Chemistry of Materials* **2003,** *15,* 1020–1028.

[14] Chen, X.; Mao, S. S. *Chem. Rev* **2007,** *107,* 2891–2959.

[15] Cronemeyer, D. C. *Physical Review* **1952,** *87,* 876.

[16] Breckenridge, R. G.; Hosler, W. R. *Physical Review* **1953,** *91,* 793.

[17] Geraghty, K.; Donaghey, L. *Thin Solid Films* **1977,** *40,* 375–383.

[18] Schiller, S.; Beister, G.; Sieber, W.; Schirmer, G.; Hacker, E. *Thin Solid Films* **1981,** *83,* 239–245.

[19] Williams, L.; Hess, D. *Journal of Vacuum Science & Technology A: Vacuum, Surfaces, and Films* **1983,** *1,* 1810–1819.

[20] Fukushima, K.; Yamada, I. *Applied Surface Science* **1989,** *43,* 32–36.

[21] Xie, Q.; Jiang, Y.-L.; Detavernier, C.; Deduytsche, D.; Van Meirhaeghe, R. L.; Ru, G.-P.; Li, B.-Z.; Qu, X.-P. *Journal of Applied Physics* **2007,** *102,* 8.

[22] Hwu, Y.; Yao, Y.; Cheng, N.; Tung, C.; Lin, H.-M. *Nanostructured Materials* **1997,** *9,* 355–358.

[23] Penn, R. L.; Banfield, J. F. *Geochimica et Cosmochimica acta* **1999,** *63,* 1549–1557.

[24] Gribb, A. A.; Banfield, J. F. *American Mineralogist* **1997,** *82,* 717–728.

[25] Hou, Y.-Q.; Zhuang, D.-M.; Zhang, G.; Zhao, M.; Wu, M.-S. *Applied Surface Science* **2003,** *218,* 98–106.

[26] Sankar, S.; Gopchandran, K. *Crystal Research and Technology* **2009,** *44,* 989–994.

[27] Busani, T.; Devine, R. *Semiconductor science and technology* **2005,** *20,* 870.

[28] D., S. R.; T., P. C. *Acta Crystallographica Section B 25,* 925-946.

[29] Scheuermann, A. G.; Lawrence, J. P.; Kemp, K. W.; Ito, T.; Walsh, A.; Chidsey, C. E.; Hurley, P. K.; McIntyre, P. C. *Nature materials* **2015,** *15,* 1.

[30] Reiners, M.; Xu, K.; Aslam, N.; Devi, A.; Waser, R.; Hoffmann-Eifert, S. *Chemistry of Materials* **2013,** *25,* 2934–2943.

[31] Reddy, K. M.; Baruwati, B.; Jayalakshmi, M.; Rao, M. M.; Manorama, S. V. *Journal of Solid State Chemistry* **2005,** *178,* 3352–3358.

[32] Di Valentin, C.; Pacchioni, G.; Selloni, A. *Chemistry of Materials* **2005,** *17,* 6656–6665.

[33] O'Connor, É.; Cherkaoui, K.; Monaghan, S.; O'Connell, D.; Povey, I.; Casey, P.; Newcomb, S. B.; Gomeniuk, Y. Y.; Provenzano, G.; Crupi, F. *Journal of Applied Physics* **2012,** *111,* 124104.

[34] Castaldini, A.; Cavalcoli, D.; Cavallini, A.; Susi, E. *Applied Physics A* **2002,** *75,* 601–605.

Chapter 6

Summary and Future Work

6.1 Summary

The primary aim of this thesis was to examine the use of nanostructured electrodes in water splitting applications, in particular the development of potential protective oxides that are able to successfully protect the photoactive silicon underneath. By studying the properties of the oxides, it was possible to better understand the electrical behaviour of the structures and aim to provide the best solution for the protective oxide. The important results are summarised below.

Indium-tin-oxide on silicon was investigated as a potential protective oxide for water splitting anodes. Although ITO on n-type silicon has a large barrier, this indicates that ITO on p-type or p++ silicon has a low barrier. This means that electrically ITO is a suitable candidate however it does suffer from degradation under different pH values.

A study was carried out to determine if the stoichiometry of TiO_2 can affect the leakage current. By growing TiO_2 using ALD and PEALD and varying the oxygen half cycle to create films with different Ti^{3+} to Ti^{4+} ratios. These films were measured electrically and showed a strong trend that increased oxygen vacancies resulted in increased leakage current on p-type silicon.

An investigation into the current conduction mechanism of the TiO_2 thin films, indicated more than one current conduction mechanism, however increased oxygen vacancies, i.e. traps in the oxide, showed a trend towards Poole-Frenkel beginning to dominate over the thermionic emission.

The dependency of the thickness of ALD grown TiO_2 was measured in a MOS structure. Results were contradictory to those expected were exhibited in the dark IV electrical experiments. As the TiO_2 thickness increased from 5 nm to 10 nm, the current density for a fixed bias increased. For a TiO_2 thickness > 10 nm the TiO_2 conductivity at a given bias was almost independent of thickness.

Ellipsometry data indicated that the density of the films changed as the films get thicker, which possibly resulted in a change in the current mechanism allowing for a higher leakage current.

The validity of comparing dark IV measurements and electrochemical experiments was investigated. Using the samples from the thickness dependency study, electrochemical measurements were undertaken, in which the dark cyclic voltammetry showed a more expected result where the increased TiO_2 thickness resulted in an increased peak to peak voltage. However, the p+n Si anode did not see this increased peak to peak voltage. These structures exhibited a constant photovoltage of 0.55 V across the full TiO_2 thickness range. However, this showed a definite mismatch between the different measurements. Due to the simplicity of the experiment, dark IV results should be used to measure the different resistances of the protective oxide being studied.

Mixed oxides films were grown by ALD using a novel method of underpulsing the titanium precursor, in order to leave reaction sites available for the second metal to react with. The results showed that the second metal precursor was incorporated due to this underpulsing. This is a new method for creating mixed oxides, in comparison to the more traditional method of using a supercycle, which results in a series of laminate films.

An investigation into how the incorporated metal changed the electrical properties was undertaken. For the current-voltage characteristics, the mixed oxides showed increased leakage current, in general with the lower level of incorporation. In particular the Zn-TiO_2 sample showed the largest increase in leakage current. This result is of particular interest to the water splitting applications, as increasing the current through the protective oxide increases the performance of the photoelectrochemical cell.

The measurement of the k values indicated an unexpected trend where the films with lower incorporation of the second metal caused the k value to drop

142

significantly. However, in the case of the films with higher incorporation, the k value increased again. In one case the k value increases to higher than the TiO_2 control sample.

An annealing study of these samples was undertaken and although results were not helpful for water splitting applications as current-voltage characteristics follow a general trend of reduced leakage current with increasing annealing temperature.

6.2   Future work

There are several areas for future investigation arising out of this work as outlined below.

- A study into the role carbon and nitrogen play in the electrical properties of TiO_2 would be desirable because if the oxygen vacancies are to be altered it is important to understand the role of the dopants.

- A reliability study of TiO_2 in terms of oxygen vacancies from both an electrical standpoint and electrochemical standpoint. If a less stoichiometric film reduces the electrical reliability it will reduce the lifetime of a potential device. From an electrochemical standpoint, it is important to understand if the stoichiometry of the films will be affected by the electrochemical reaction, and to understand if a less stoichiometric films is still able to provide the same protection level.

- A conduction mechanism study into the thickness series of TiO_2 samples should be undertaken, to further study the reason behind the unexpected electrical behaviour.

- A reliability study into the benefit of using a thicker protective oxide on the long-term cell stability.

- An investigation into all the different parameters in the electrochemical measurement that influence the result.

- A further study into finding the optimal ratio of the two metals, to gain the greatest increase in leakage current, after which testing the optimal film in a water splitting cell. As part of this study, an investigation into the current conduction mechanism should be undertaken in order to ascertain how the second metal aids conduction.

Appendix

.1   Journal Publications and Presentations

Nature Materials, 2016, 15,99

WODIM 2016 - Investigating the effect of TiO_2 thickness on the electrical conductivity and photoelectrochemical response of metal/TiO_2/SiO_x/Si photoanodes - Oral presentation.

.2 Nature Materials, 2016, 15,99

Design principles for maximizing photovoltage in metal-oxide-protected water-splitting photoanodes

Andrew G. Scheuermann[1], John P. Lawrence[1], Kyle W. Kemp[1], T. Ito[1,2], Adrian Walsh[3], Christopher E. D. Chidsey[4], Paul K. Hurley[3] and Paul C. McIntyre[1]*

Metal oxide protection layers for photoanodes may enable the development of large-scale solar fuel and solar chemical synthesis, but the poor photovoltages often reported so far will severely limit their performance. Here we report a novel observation of photovoltage loss associated with a charge extraction barrier imposed by the protection layer, and, by eliminating it, achieve photovoltages as high as 630 mV, the maximum reported so far for water-splitting silicon photoanodes. The loss mechanism is systematically probed in metal–insulator–semiconductor Schottky junction cells compared to buried junction p$^+$n cells, revealing the need to maintain a characteristic hole density at the semiconductor/insulator interface. A leaky-capacitor model related to the dielectric properties of the protective oxide explains this loss, achieving excellent agreement with the data. From these findings, we formulate design principles for simultaneous optimization of built-in field, interface quality, and hole extraction to maximize the photovoltage of oxide-protected water-splitting anodes.

Splitting water into hydrogen and oxygen is a key component of clean fuel and chemical synthesis from solar energy. Water splitting using a photoelectrochemical junction was first demonstrated by Fujishima and Honda in 1972, and has since progressed significantly[1–7]. Metal–insulator–semiconductor (MIS) technology, a key materials driver of the information age[8], and the even simpler semiconductor–liquid junction are promising candidates for these applications, but the best materials have suffered from a lack of simultaneous efficiency and stability. In 2011, Chen et al. first used ultrathin (1–2 nm) ALD-TiO$_2$ to protect silicon anodes where conduction was limited by carrier tunnelling[9]. In 2013, Scheuermann et al. studied amorphous, as-deposited ALD-TiO$_2$ films up to 12 nm in thickness, finding bulk-limited conduction with a modest Ohmic loss, $\sim$21 mV nm^{-1} of additional TiO$_2$, for p$^+$Si anodes oxidizing water in the dark[10]. A hole-conduction model was proposed involving tunnelling through the ultrathin SiO$_2$ and hopping via traps in the TiO$_2$. More recently, Hu et al.[11] fabricated ALD-TiO$_2$-protected devices under similar deposition conditions to those employed previously[9,10] and coated with a nickel catalyst. They investigated thicker TiO$_2$, including films >100 nm, and observed a photocurrent onset voltage during water oxidation that was essentially independent of TiO$_2$ thickness[11]. If the conduction mechanism is the same, then the hole conductivity must be at least four orders of magnitude higher than in ref. 10. The same group has also recently used $\sim$1 nm ALD-TiO$_2$ to protect CdTe (ref. 12) and BiVO$_4$ (ref. 13).

Despite enhanced TiO$_2$ conductivity, the silicon photovoltages achieved in refs 11–13 are $\sim$400 mV or less, far below the theoretical maximum for silicon photovoltaics of 700–800 mV (ref. 14), the 740 mV record achieved with HIT (heterojunction with intrinsic layer) solar cells[15], or the highest previously reported

MIS water-oxidation photovoltage of 550 mV (ref. 9). Silicon is considered to be nearly ideal for the bottom cell of a tandem device combined with a large bandgap ($\sim$1.8 eV) top cell[16]. However, the silicon must provide >600 mV of photovoltage to give acceptable performance. Even with a perfect fill factor, the silicon photovoltages reported so far using highly conductive TiO$_2$ (ref. 11) fall far short. Furthermore, it remains unclear if the reported influence of nickel coating is generally capable of ensuring high hole conductivity in TiO$_2$ (ref. 11).

There is a need, therefore, to understand fundamental aspects of oxide protection layers, as they pertain both to photovoltage and photocurrent, for the ultimate optimization of cell efficiency. Herein, we show why relatively insulating (capacitive), as distinct from highly conductive, oxide protection layers promote higher photovoltages, and present what we believe is the first report on oxide protection layer thickness scaling of the photovoltage. Using a buried p$^+$n silicon junction we demonstrate that this oxide thickness dependence of the photovoltage can be removed, and achieve the highest photovoltage for a water-oxidation silicon photoanode yet reported, of $\sim$630 mV, making the TiO$_2$-protected silicon cell viable for a tandem device. Finally, we show how these observations suggest general design principles for maximizing the photovoltage in any insulator-protected architecture.

Results

Photovoltage loss in ALD-TiO$_2$-protected nSi MIS photoanodes. Three junction types have been examined so far for water-splitting photoanodes: semiconductor–liquid junctions (SL, herein referred to as Type 0) requiring a stable semiconducting metal oxide in contact with water; Schottky junctions, either with a direct metal contact to the semiconductor[17,18] or with an interposed protective

[1]Department of Materials Science and Engineering, Stanford University, Stanford, California 94305, USA. [2]Tokyo Electron Limited, Technology Development Center, 650, Hosaka-cho Mitsuzawa, Nirasaki, Yamanashi 407-0192, Japan. [3]Tyndall National Institute, University College Cork, Cork, Ireland. [4]Department of Chemistry, Stanford University, Stanford, California 94305, USA. *e-mail: pcm1@stanford.edu
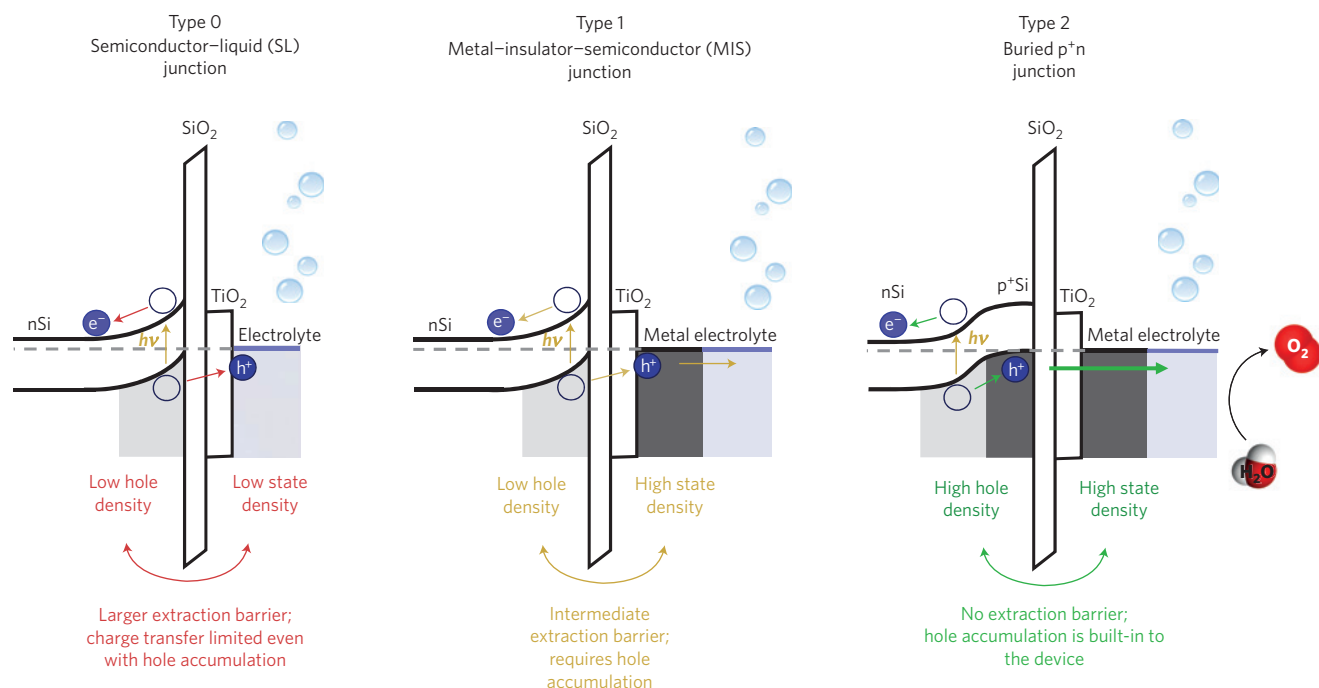
Figure 1 | Three junction types showing the extraction barrier imposed by the protection layer illustrated with silicon water-oxidation photoanodes.
Three types of photoanode junctions have been employed in the literature, the Type 0 semiconductor–liquid (SL), Type I MIS Schottky, and Type II MIS p+n junction. Here, each junction configuration is shown for a silicon cell protected by TiO_2. The insulators introduce a series resistance, which when located inside the junction constitutes an extraction barrier. Therefore, the density of holes at the interface and the density of states of the contact play a key role. In Type 0 cells, holes will be accumulated at the semiconductor/insulator interface during current flow, and charge transfer may still be significantly limited owing to a low density of states in the contact. Such a situation may arise from using electrolytes as well as non-metallic catalysts as the hole conduction mediator. In Type 1 cells, moderate hole accumulation is sufficient to efficiently extract minority carriers, but the photovoltage suffers an insulator-thickness-dependent loss. In Type 2 cells, the p+ region ensures a high hole concentration at the interface that is independent of illumination and bias, resulting in no barrier to hole extraction. As a result, these cells exhibit no dependence of photovoltage on the insulator thickness and achieve record photovoltages at all oxide thicknesses and pH values studied.

metal oxide layer, forming a MIS (or Type 1) structure[9–11]; and buried pn junctions (Type 2), which likewise may[11] or may not[19] incorporate additional protective oxides. The fabrication complexity increases, in general, from Type 0 to 1 to 2 and, as this report details, the hole extraction barrier induced by protection layers can be made to decrease accordingly for each type, for the same insulator layers.

Beginning in the 1970s, Green and co-workers discussed the utility of a surface inversion layer in so-called conductor–insulator–semiconductor (CIS) solar cells (similar to the MIS structures discussed here), where an ultrathin insulator provides defect passivation while being thin enough to allow facile tunnel conduction[20–25]. Maintaining a high charge density at the semiconductor/oxide interface is desirable for all CIS cells. These include electrolyte-gated electrolyte–insulator–semiconductor (EIS) cells (Type 0), metal-gated MIS cells (Type 1 and Type 2) and semiconductor-gated cells (SIS), in which a degenerate semiconductor acts as the contact, similar to the case of a conductive (for example, defect-doped) TiO_2-nSi junction. The photovoltage produced by such junctions is controlled by the built-in voltage, which is the difference between the contact work function (whether electrolyte, metal, or degenerate semiconductor) and the work function of the semiconductor substrate, modified by the presence of charges and interface fields[23]. The inversion layer's function in CIS cells is to screen states at the oxide/silicon interface and promote minority-carrier transport across the insulator. (By maintaining an inversion layer of minority carriers, interface traps, particularly mid-gap states, are constantly filled so that they do not act as recombination-generation centres for photogenerated carriers. See refs 20,21,23,24 in particular.) Green and colleagues specifically used minimally defective

insulators of 1 to 3 nm thickness, providing both excellent surface defect passivation and thin tunnel barriers[20–24]. In the present context, however, oxides of much greater thickness are of interest as protection layers[10], motivating further study.

The original report of Type-1 nSi ALD-TiO_2 protection achieved a good photovoltage with an MIS tunnel junction[9]. The more recent reports on more conductive TiO_2 may describe SIS junctions incorporating a Ni OER (oxidation evolution reaction) catalyst, degenerate (defective) semiconducting TiO_2, and an interfacial SiO_x layer[11]. Large insulator trap densities can reduce MIS solar cell efficiency[18]. A recent study of conductive TiO_2 with photovoltages between 150 and 350 mV (ref. 26) suggests that an nSi–TiO_2 SIS junction is formed, rather than a catalyst/oxide/silicon MIS junction. A conductive TiO_2 layer may screen the influence of the Ni catalyst work function[11], preventing it from setting the photovoltage. The Fermi level in degenerate n-type TiO_2 will lie near the TiO_2 conduction band and is therefore unlikely to form a high-photovoltage junction with nSi. Recent work[27] shows that a Ti metal layer between the TiO_2 and Si also creates a conductive structure, but the workfunction of Ti is too small to form a high-photovoltage Type 1 junction with nSi. Further, the Ti/Si interface is not stable, and may form a resistive metal silicide during anneals[28,29].

In an effort to achieve large photovoltage and stability, a series of nSi photoanodes (Type 1) were fabricated with the Ir/ALD-TiO_2/SiO_2/Si layer sequence, independently varying the TiO_2 and SiO_2 thickness. Iridium is used as the catalyst, providing a low water-oxidation overpotential, stability at all pH, a high work function for optimal built-in voltage, and high density of states for optimal charge transport. Previous work[10,11] has demonstrated
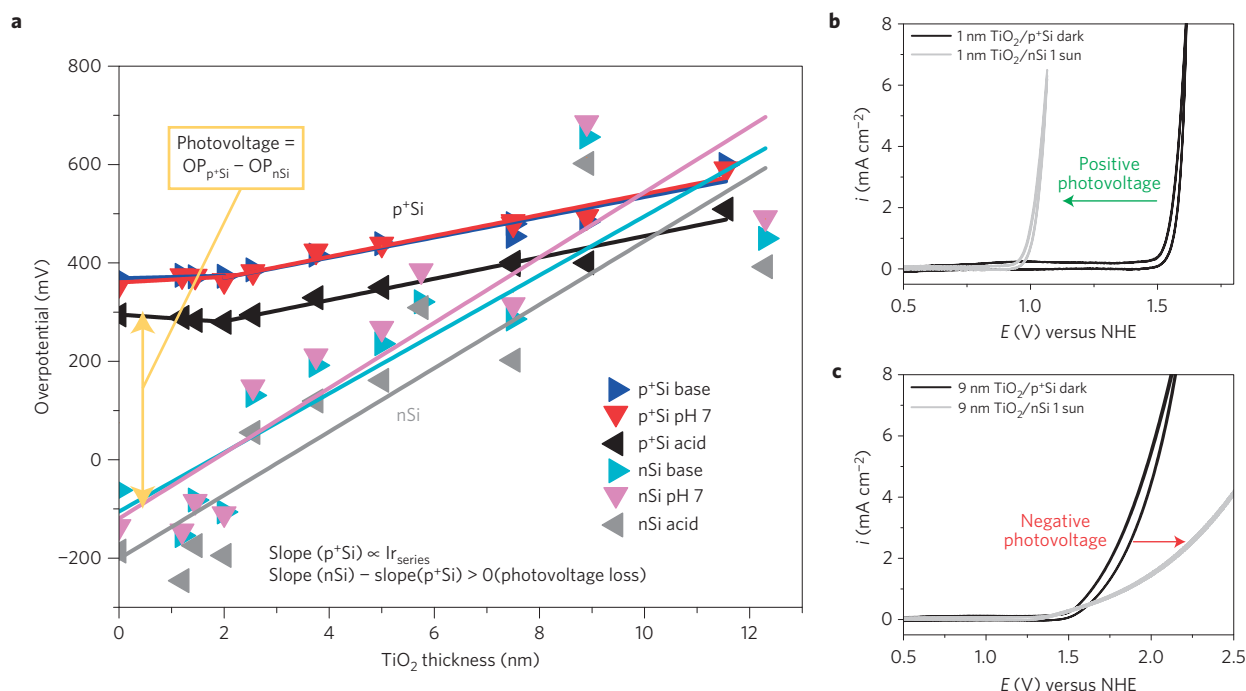
Figure 2 | Photovoltage loss in ALD-TiO$_2$-protected nSi MIS anodes. a, Water oxidation overpotential at 1 mA cm^{-2} current density—that is, the potential with respect to the thermodynamic potential E^0(H$_2$O/O$_2$), at pH values of 14, 7 and 0. Device results are plotted as a function of TiO$_2$ thickness in Ir/TiO$_2$/SiO$_2$/p$^+$Si anodes splitting water in the dark, compared to Ir/TiO$_2$/SiO$_2$/nSi photoanodes under 1 sun illumination. **b,c,** The trends converge, showing a decreasing photovoltage that starts at a value >500 mV (**b**) and ends with negative apparent photovoltages (**c**). Panels **b** and **c** are both for water oxidation in pH = 0 acid solution, where i is the current density and the voltage is reported with reference to the normal hydrogen electrode (NHE), thus the thermodynamic water oxidation potential is 1.229 V.

that numerous other OER catalysts also exhibit advantageous work functions and high densities of states for this Type 1 cell[10]. The photovoltage, herein defined as the difference between the overpotential to drive 1 mA cm^{-2} through the illuminated nSi photoanode and the dark p$^+$Si anode, is represented by the yellow, two-sided arrow in Fig. 2a. (One sun of AM 1.5 illumination is used consistently in this study). The thinnest as-deposited TiO$_2$ coatings yield photovoltages of 500–550 mV (Fig. 2b). This value is between 150 and 400 mV higher than reported for conductive TiO$_2$ protection layers on nSi (refs 11,26). However, the inferred photovoltage decreases with increasing TiO$_2$ thickness to the point where it becomes negative (Fig. 2c). By referencing the nSi (light) to the p$^+$Si (dark) overpotential for the same TiO$_2$ thickness, the oxide series resistance is removed, indicating that this component of the photovoltage loss is not due simply to Ohmic loss in the oxide.

This thickness-dependent photovoltage loss is of the order of three times higher than the Ohmic loss in the reference p$^+$Si structure. To better understand the photovoltage loss, insulator fixed charge and Shockley–Read–Hall (SRH) recombination were investigated, two common factors affecting MIS junction voltage. For fixed charge, a set of matching p-type MIS capacitors were fabricated (see Supplementary Fig. 1). Bulk positive or negative insulator charge can be observed as a parabolic shift of the flat band voltage (V_{FB}) with insulator thickness for both p-type and n-type silicon in capacitance–voltage (CV) analysis. When probing TiO$_2$, p-type silicon gives a more robust analysis of V_{FB} because of lower gate leakage currents for this substrate doping. Supplementary Fig. 1 shows that the V_{FB} has no discernible oxide thickness dependence, suggesting that fixed insulator charge is negligible and unchanging. In addition, p$^+$Si anodes were measured electrochemically in the dark and light to detect any light-induced charging. No charging under illumination is observed (Supplementary Fig. 2).

To investigate SRH recombination, the reverse dark current was measured. An increase in the density of recombination-generation (R-G) centres will increase the rate of thermal generation of minority carriers—thus increasing the reverse saturation current, I_0. The measured reverse dark currents do not, however, correlate with the low-photovoltage devices. Rather, I_0 decreases with insulator thickness, showing Ohmic behaviour with decreasing hole conductivity (Supplementary Section 3). Thus, neither of these factors, fixed charge in the oxide nor an increasing density of SRH recombination centres, is consistent with the observed decreasing photovoltage with increasing oxide thickness.

Photovoltage loss also observed with interlayer SiO$_2$. Different SiO$_2$ interlayer thicknesses were also probed for the their effect on photovoltage using slot plane antenna (SPA) plasma oxidation, previously shown to give high-quality tunnel oxide layers with precise thickness control[30–32]. Figure 3 shows the photovoltage dependence with SiO$_2$ thickness, both with and without ALD-TiO$_2$. In both cases, the photovoltage decreases with oxide thickness.

Simple metal/SiO$_2$/Si devices also exhibit decreasing photovoltage with increasing oxide thickness. The ALD-TiO$_2$ used in this study is less resistive than the tunnel oxide SiO$_2$, but more resistive than the TiO$_2$ reported in ref. 11. The fact that adding a second insulator (TiO$_2$) inside the junction increases the photovoltage loss at an equivalent SiO$_2$ thickness suggests the source of the photovoltage loss: a charge extraction barrier where greater voltage is required at greater oxide thicknesses to extract the same current from the device. This effect should be independent of any catalyst with a similar density of states, indicating that this loss is of general concern for MIS Type 1 photoelectrodes, both with and without additional protection layers.

This charge extraction barrier also leads to the observation that Type 0 TiO$_2$/SiO$_2$/nSi and SiO$_2$/nSi photoelectrochemical cells
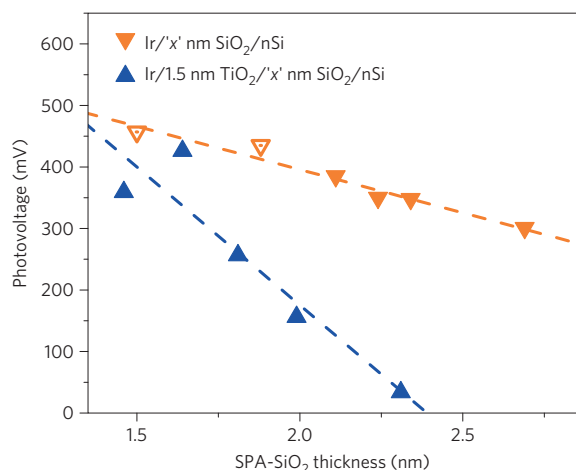
Figure 3 | Photovoltage loss observed with increasing thickness of the SiO₂ interlayer with and without TiO₂. The photovoltage decreases with thickness of the SiO₂ both with (blue) and without (orange) protective TiO₂. Anodes with less than 2 nm of SiO₂ and no protective TiO₂ (hollow orange markers) are highly unstable and the results are subject to error. It is possible that these devices have already degraded, leading to an underestimation of the photovoltage loss with respect to thickness for Ir/SiO₂/nSi photoanodes (see Supplementary Fig. 4). In all cases, the photovoltage decreases rapidly with SiO₂ interlayer thickness and, similar to the TiO₂ case, with a linear dependence on thickness, although the slope is much greater.

with a high-work-function electrolyte, ferri/ferrocyanide, exhibit essentially no photovoltage (Supplementary Fig. 5). The effect of decreasing photovoltage due to a resistive oxide barrier within the junction is thus applicable to Type 0 and Type 1 cells alike, with an increased penalty for a low-density-of-states contact as in the Type 0 case.

Capacitor model for voltage loss, and p⁺n buried junctions.
Previous reports on MIS photovoltaics showed that inversion layer n-type MIS junctions could perform as well as p⁺n buried junctions, principally as a result of surface state screening[20–25]. In that work, the

insulator was believed to promote ideal Schottky behaviour, which required only very thin insulating layers with no benefit from thicker layers. To study this new regime, where thicker layers provide benefit for device stability, Sentaurus modelling software was used (Fig. 4) to simulate band diagrams of Schottky (Type 1) and p⁺n (Type 2) photoanodes. The Type 1 cell contains a surface inversion layer as a result of the high work function catalyst, but the hole density is less than in a Type 2 cell, and is more sensitive to illumination and photo current (Supplementary Fig. 6). The implanted p⁺ region maintains a high hole density at the interface and, the deeper it is placed, the more the interface charge is unaffected by operating conditions. However, if buried deeper than the minority-carrier diffusion length (approximately 1 µm (refs 33,34) for degenerate boron-doping ∼10¹⁹ cm⁻³), recombination will increase.

From this modelling, buried junction p⁺nSi substrates were prepared with a high implantation dose ∼5 × 10¹⁹ cm⁻³ and junction depth less than the 1 µm minority-carrier diffusion length. The depth was characterized using an etched bevel and by scanning electron microscopy (SEM) cross-section imaging, both methods yielding approximately 450 nm (Supplementary Figs 8 and 9). Equivalent insulator layers and catalyst metal were deposited on these substrates, p⁺Si and nSi, to compare the photovoltage dependence of Type 1 and Type 2 structures. Capacitance–voltage analysis was carried out on these devices and on those in Fig. 2, confirming that the nSi Type 1 structure does exhibit an inversion layer at zero applied bias (Supplementary Section 10). As in Fig. 2, a large photovoltage loss relative to the p⁺Si sample was observed with increasing TiO₂ thickness for Type 1, but Type 2 showed no loss relative to the p⁺Si sample. Furthermore, record photovoltages were achieved across the thickness range studied.

Cyclic voltammetry data for ferri/ferrocyanide (FFC) redox clearly show large asymmetric losses at positive potentials for the Type 1 nSi structure, corresponding to the extraction barrier for holes (compare Fig. 5b to Fig. 5a). The p⁺nSi series, alternatively, shows nearly identical ferri/ferrocyanide peak shapes as for p⁺Si, but shifted by large photovoltages that are independent of the protective insulator thickness. Figure 5d shows the improvement obtained with p⁺nSi compared to Type 1 nSi, eliminating the loss and achieving photovoltages of over 600 mV both versus the ferri/ferrocyanide Nernstian cell potential and for water oxidation calculated as the shift between the p⁺Si reference and photoanodes
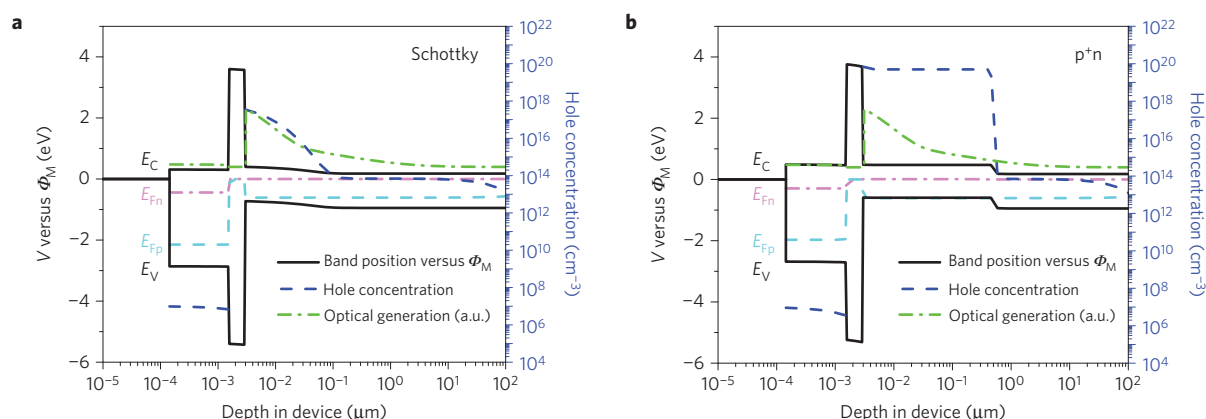

Figure 4 | Simulated band diagrams reveal differences between Type I Schottky junction structures and Type 2 p⁺n buried junction structures. a,b, Band diagrams are simulated under 1 sun of AM 1.5 G illumination and device operation at 1 mA cm⁻² for the Type 1 MIS Schottky (**a**) and the Type 2 buried junction case (**b**). E_C and E_V denote the conduction band and valence band. E_{Fn} and E_{Fp} denote the quasi-electron and quasi-hole Fermi levels under illumination. The high-work-function metal creates a thin inversion layer of holes in the Type 1 nSi structure, reaching 3×10^{17} cm⁻³ at the interface, but it is insufficient to maintain a high hole density at the interface, regardless of operating conditions, compared with a 5×10^{19} cm⁻³ implanted p⁺ region. The optical generation is shown here in arbitrary units. Full details and the integrated photogeneration can be found in Supplementary Section 7.
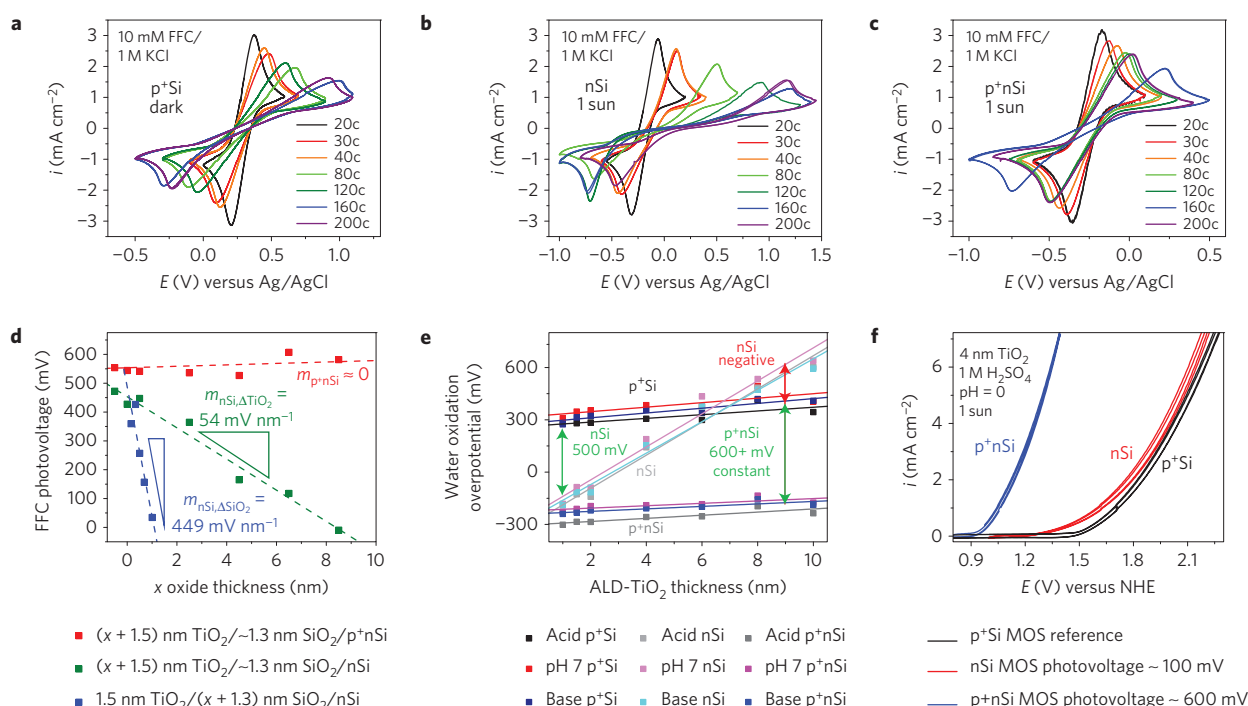
Figure 5 | Charge extraction photovoltage loss eliminated and record photovoltages achieved with Type 2 p⁺n buried junction cells. a–c, Electrochemical performance of Ir/ALD-TiO₂/SiO₂/Si anode of varying TiO₂ thickness (for example, 20c = 20 TDMAT/H₂O ALD cycles = 1.2 nm) in ferro/ferrocyanide (FFC) for a p⁺Si reference substrate (**a**), nSi Type 1 MIS junction under 1 sun illumination (**b**) and p⁺nSi Type 2 buried junction under 1 sun (**c**). A large, asymmetric loss (asymmetric stretching of the CV) is observed for Type 1 nSi MIS structures, compared with the p⁺Si reference, which is eliminated in the Type 2 p⁺nSi structure. TDMAT, tetrakis(dimethylamido)titanium. **d**, This translates to a near-constant photovoltage for Type 2 cells (red squares) compared with steep losses when increasing TiO₂ (green squares) or SiO₂ (blue squares) in the Type 1 cell. **e**, For water oxidation, the same effect is observed, where the Type 2 p⁺nSi leads to a constant overpotential shift with respect to the p⁺Si (dark) reference, corresponding to record photovoltages of 550 mV to >600 mV at all pH values. In the Type 1 nSi cell, the inferred photovoltage goes from positive (green double-headed arrow) 500 mV to negative (red double-headed arrow) 200 mV. **f**, Water-oxidation cyclic voltammetry for a 4 nm TiO₂ layer showing an ~100 mV photovoltage shift in the nSi MIS compared with an ~600 mV shift for the equivalent p⁺nSi MIS.

at approximately zero current (Supplementary Section 14). The highest value is 607 mV in FFC and 630 mV in pH 7 solution with 8 nm of TiO₂. Similar values of 550 mV to >600 mV are achieved for all thicknesses and pH (Supplementary Table 15). The previous record for silicon water oxidation was 550 mV, for ultrathin TiO₂ on nSi using a post-ALD forming gas anneal[9]. Other leading results for stable MIS photoanodes include 410 mV with conductive TiO₂ on nSi and 520 mV on p⁺nSi (ref. 11), 500 mV with Ni catalyst protecting nSi (ref. 17), and 500 mV with Ir/IrO$_x$ or NiO$_x$ protection of p⁺nSi (refs 18,19). Another recent report using a p-type transparent oxide NiCo₂O₄ as the protection layer, with the valence band aligned for hole transport, achieves a photovoltage shift at 1 mA cm^{-2} of 506 mV versus the p⁺Si reference, modelling a theoretical open-circuit voltage of ~650 mV for the p⁺n junction[35].

These findings support the hypothesis that a charge extraction barrier introduced by interposed insulators suppresses the photovoltage and that achieving a characteristic hole interface density for a given current density at the silicon/insulator interface is required. This is a requirement of Gauss' law. A given hole interface density in the semiconductor Q_{si} sets the surface field in the semiconductor E_s. This field in turn sets the field in the insulator E_i, which controls the leakage current through the insulator. Therefore, a given insulator leakage current density requires a characteristic interface charge density:

$$Q_{si} = -\varepsilon_0 \varepsilon_s E_s = -\varepsilon_0 \varepsilon_i E_i \qquad (1)$$

Equation (1) holds true assuming negligible fixed charge at the interface, where ε_0 is the permittivity of free space, and ε_i and ε_s

are the relative permittivities of the insulator and semiconductor, respectively. If, in Type 1 structures, the surface charge is insufficient to achieve the required photocurrent, a photovoltage penalty ΔV is incurred to increase the charge by an amount ΔQ for a given insulator thickness t_i as given by equation (2), where A is the MIS junction area:

$$\Delta V = \frac{\Delta Q}{C} = \frac{\Delta Q}{\varepsilon_0 \varepsilon_i A} t_i \qquad (2)$$

This predicted linear relationship between photovoltage loss and insulator thickness agrees with our results. Further, the constant of proportionality depends on the dielectric properties of the insulators. By considering a bilayer TiO₂/SiO₂ structure, the model can be extended. Figure 5d shows the empirical scaling of the photovoltage dependence for TiO₂ and SiO₂ individually. These trends intersect at a point representing the same device and, necessarily, the same surface charge. Taking the ratio of the partial derivatives about this shared point (Supplementary Section 16) yields equation (3), where m denotes the slope of the photovoltage loss (dV/dt_i):

$$\frac{m_{SiO_2}}{m_{TiO_2}} = \frac{\varepsilon_{TiO_2}}{\varepsilon_{SiO_2}} \qquad (3)$$

Equation (3) states that the ratio of the photovoltage losses for Type 1 junctions as a function of TiO₂ and SiO₂ thickness, m_{TiO_2} and m_{SiO_2}, respectively, is equal to the inverse ratio of the insulators' dielectric constants. For ferri/ferrocyanide redox, the bilayer photovoltage dependence with respect to SiO₂ is ~449 mV nm^{-1} and with respect to ALD-TiO₂ is ~54 mV nm^{-1}.

Table 1 | Photovoltage loss and inverse dielectric constant ratios for TiO$_2$/SiO$_2$ Type 1 anodes.

System	Photovoltage trend ratio	Inverse dielectric constant ratio
1.5 nm TiO$_2$/'x' nm SiO$_2$ 'x' nm TiO$_2$/1.3 nm SiO$_2$	$\dfrac{449\,\mathrm{mV\,nm^{-1}}}{54\,\mathrm{mV\,nm^{-1}}} = 8.3$	$\dfrac{32}{3.9} = 8.2$

We assume dielectric constants of 3.9 (ref. 36) for SiO$_2$ and 32 (ref. 37) for TiO$_2$, as previously measured for similar amorphous ALD-TiO$_2$. Predictions of the capacitor model and the observed empirical photovoltage scalings with TiO$_2$ and SiO$_2$ thickness are in excellent quantitative agreement (Table 1).

These results indicate the necessity of maintaining high minority-carrier interface charge density for efficient MIS operation with thicker protective insulators. This effect is not restricted to silicon as the semiconductor, and should not only be generally applicable to various MIS systems, but also to EIS and SIS systems whenever conduction through thicker insulators is required. Consideration of these design principles allows one to understand the surprising result that record photovoltages in Type 2 p$^+$nSi structures and negative inferred photovoltages in Type 1 nSi structures are observed for identical insulator layers and OER catalyst.

Conclusions

In this Article we have observed and quantified a photovoltage loss associated with hole extraction barriers in MIS water-splitting cells using n-type silicon photoanodes, proposed a general model to understand and predict the loss, fabricated cells using a p$^+$n silicon anode structure that overcomes this loss, and realized record photovoltages at all insulator thicknesses studied, with a maximum value of 630 mV. Understanding the protection layer's effects on built-in field, interface quality, and charge extraction suggests a set of general design principles. The first principle is to balance minimal resistance with a high-quality interface to ensure high built-in field and low recombination rate. High interface trap densities approaching ~1%, or ~10^{13} cm^{-2} states, may pin the Fermi level[38]. Alternatively, degenerate doping of an oxide protection layer changes the device to an SIS architecture, which can achieve ideal built-in fields only if the doped oxide exhibits a high work function. Less defective oxides can provide excellent surface passivation and allow the high-work-function OER catalyst to set the field. For the nSi case, this report demonstrates photovoltages of 550 mV with an MIS junction, compared to an ~400 mV photovoltage with a conductive TiO$_2$ SIS junction[11]. The second principle is to minimize charge extraction barriers to achieve a high photovoltage during operation. This can be accomplished either by reducing the oxide resistance within the junction or by separating the oxide layers from the junction and keeping the interface charge density high using a Type 2 p$^+$n anode structure. Reducing the oxide resistance must not compromise chemical, electrical and thermal stability or diminish the voltage. Keeping the interface hole density high promotes facile carrier transport. A Type 2 junction depth of ~450 nm thickness with 5 × 10^{19} cm^{-3} hole concentration was sufficient to recover all the photovoltage loss in corresponding Type 1 nSi water-splitting cells.

Methods

Methods and any associated references are available in the online version of the paper.

References

1. Fujishima, A. & Honda, K. Electrochemical photolysis of water at a semiconductor electrode. *Nature* **238**, 37–38 (1972).
2. Heller, A. Conversion of sunlight into electrical power and photoassisted electrolysis of water in photoelectrochemical cells. *Acc. Chem. Res.* **14**, 154–162 (1981).
3. Bard, A. J. & Fox, M. A. Artificial photosynthesis: Solar splitting of water to hydrogen and oxygen. *Acc. Chem. Res.* **28**, 141–145 (1995).
4. Turner, J. A. A realizable renewable energy future. *Science* **285**, 687–689 (1999).
5. Grätzel, M. Photoelectrochemical cells. *Nature* **414**, 338–344 (2001).
6. Lewis, N. S. Light work with water. *Nature* **414**, 589–590 (2001).
7. Lewis, N. S. & Nocera, D. G. Powering the planet: Chemical challenges in solar energy utilization. *Proc. Natl Acad. Sci. USA* **103**, 15729–15735 (2006).
8. Bassett, R. K. *To the Digital Age: Research Labs, Startup Companies, and the Rise of MOS Technology* (John Hopkins Univ. Press, 2007).
9. Chen, Y. W. *et al.* Atomic layer-deposited tunnel oxide stabilizes silicon photoanodes for water oxidation. *Nature Mater.* **10**, 539–544 (2011).
10. Scheuermann, A. G., Prange, J. D., Gunji, M., Chidsey, C. E. D. & McIntyre, P. C. Effects of catalyst material and atomic layer deposited TiO$_2$ oxide thickness on the water oxidation performance of metal–insulator–silicon anodes. *Energy Environ. Sci.* **6**, 2487–2496 (2013).
11. Hu, S. *et al.* Amorphous TiO$_2$ coatings stabilize Si, GaAs, and GaP photoanodes for efficient water oxidation. *Science* **344**, 1005–1009 (2014).
12. Lichterman, M. F. *et al.* Stabilization of n-cadmium telluride photoanodes for water oxidation to O$_2$(g) in aqueous alkaline electrolytes using amorphous TiO$_2$ films formed by atomic-layer deposition. *Energy Environ. Sci.* **7**, 3334–3337 (2014).
13. McDowell, M. T. *et al.* Improved stability of polycrystalline bismuth vanadate photoanodes by use of dual-layer thin TiO$_2$/Ni coatings. *J. Phys. Chem. C* **118**, 19618–19624 (2014).
14. Green, M. A. Limits on the open-circuit voltage and efficiency of silicon solar cells imposed by intrinsic Auger processes. *IEEE Trans. Electron Devices* **ED-31**, 671–678 (1984).
15. Green, M. A., Emery, K., Hishikawa, Y., Warta, W. & Dunlop, E. D. Solar cell efficiency tables (version 45). *Prog. Photovolt.* **23**, 1–9 (2015).
16. Hu, S. *et al.* An analysis of the optimal band gaps of light absorbers in integrated tandem photoelectrochemical water-splitting systems. *Energy Environ. Sci.* **6**, 2984–2993 (2013).
17. Kenney, M. J. *et al.* High-performance silicon photoanodes passivated with ultrathin nickel films for water oxidation. *Science* **342**, 836–840 (2013).
18. Mei, B. *et al.* Protection of p$^+$nSi photoanodes by sputter-deposited Ir/IrO$_x$ thin films. *J. Phys. Chem. Lett.* **5**, 1948–1952 (2014).
19. Mei, B. *et al.* Iron-treated NiO as a highly transparent p-type protection layer for efficient Si-based photoanodes. *J. Phys. Chem. Lett.* **5**, 3456–3461 (2014).
20. Green, M. A. & Godfrey, R. B. MIS solar cell—General theory and new experimental results for silicon. *Appl. Phys. Lett.* **29**, 610–612 (1976).
21. Green, M. A. Effects of pinholes, oxide traps, and surface states on MIS solar cells. *Appl. Phys. Lett.* **33**, 178–180 (1978).
22. Godfrey, R. B. & Green, M. A. 655 mV open-circuit voltage, 17.6% efficient silicon MIS solar cells. *Appl. Phys. Lett.* **34**, 790–793 (1979).
23. Singh, R., Green, M. A. & Rajkanan, K. Review of conductor–insulator–semiconductor (CIS) solar cells. *Solar Cells* **3**, 95–148 (1981).
24. Green, M. A. & Blakers, A. W. Advantages of metal–insulator–semiconductor structures for silicon solar cells. *Solar Cells* **8**, 3–16 (1983).
25. Grauvogl, M. & Hezel, R. The truncated-pyramid MIS inversion-layer solar cell: A comprehensive analysis. *Prog. Photovolt. Res. Appl.* **6**, 15–24 (1998).
26. McDowell, M. T. *et al.* The influence of structure and processing on the behavior of TiO$_2$ protective layers for stabilization of n-Si/TiO$_2$/Ni photoanodes for water oxidation. *ACS Appl. Mater. Interfaces* **7**, 15189–15199 (2015).
27. Mei, B. *et al.* Crystalline TiO$_2$: A generic and effective electron-conducting protection layer for photoanodes and -cathodes. *J. Phys. Chem. C* **119**, 15019–15027 (2015).
28. Levy, D., Ponpon, J. P., Grob, A., Grob, J. J. & Stuck, R. Rapid thermal annealing and titanium silicide formation. *Appl. Phys. A* **38**, 23–29 (1985).
29. Mann, R. W., Clevenger, L. A., Agnello, P. D. & White, F. R. Silicides and local interconnections for high-performance VLSI applications. *IBM J. Res. Dev.* **39**, 403–417 (1995).
30. Sekine, K., Saito, Y., Hirayama, M. & Ohmi, T. Silicon nitride film growth for advanced gate dielectric at low temperature employing high-density and low-energy ion bombardment. *J. Vac. Sci. Technol. A* **17**, 3129–3133 (1999).

31. Sugawara, T. *et al.* Characterization of ultra thin oxynitride formed by radical nitridation with slot plane antenna plasma. *Jpn. J. Appl. Phys.* **44,** 1232–1236 (2005).

32. Scheuermann, A. G., Lu, D. Q., Ito, T., Chidsey, C. E. D. & McIntyre, P. C. The effect of SPA-SiO$_2$ tunnel oxide thickness for metal–insulator–silicon photoelectrochemical cells. *ECS Trans.* **64,** 265–276 (2014).

33. Alamo, J. A. & Swanson, R. M. Modelling of minority-carrier transport in heavily doped silicon emitters. *Solid-State Electron.* **30,** 1127–1136 (1987).

34. Tyagi, M. S. & Van Overstraeten, R. Minority carrier recombination in heavily-doped silicon. *Solid-State Electron.* **26,** 577–597 (1983).

35. Chen, L. *et al.* p-type transparent conducting oxide/n-type semiconductor heterojunctions for efficient and stable solar water oxidation. *J. Am. Chem. Soc.* **137,** 9595–9603 (2015).

36. Sze, S. M. *Semiconductor Devices: Physics and Technology* (John Wiley, 2008).

37. Swaminathan, S. & McIntyre, P. C. Titania/alumina bilayer gate dielectrics for Ge MOS devices: Frequency- and temperature-dependent electrical characteristics. *Electrochem. Solid-State Lett.* **13,** G79–G82 (2010).

38. Bard, A. J., Bocarsly, A. B., Fan, F. R. F., Walton, E. G. & Wrighton, M. S. The concept of Fermi level pinning at semiconductor/liquid junctions. Consequences for energy conversion efficiency and selection of useful solution redox couples in solar devices. *J. Am. Chem. Soc.* **102,** 3671–3677 (1980).

Author contributions

A.G.S. and J.P.L. prepared all samples and performed all measurements for the initial TiO$_2$ photovoltage series first observing the photovoltage loss. A.G.S. prepared all samples and performed all measurements for the SiO$_2$ photovoltage series, capacitance voltage measurements, and buried junction p$^+$nSi experiments. A.W. prepared all p$^+$n buried junction substrates and performed all physical characterization of these junctions. K.W.K. performed Sentaurus modelling for light absorption in Type I and Type II cells, as well as simulating band diagrams. T.I. performed the SPA plasma oxidation for the experiments varying SiO$_2$ thickness. A.G.S. and K.W.K. maintained the ALD chamber for TiO$_2$ depositions and A.G.S. qualified and performed the runs. A.G.S., C.E.D.C. P.K.H. and P.C.M. designed the experiments and developed the solid-state capacitor model to explain the loss. All authors helped in the preparation of the manuscript.

Additional information

Supplementary information is available in the online version of the paper. Reprints and permissions information is available online at www.nature.com/reprints. Correspondence and requests for materials should be addressed to P.C.M.

Competing financial interests

The authors declare no competing financial interests.

Methods

Heavily boron-doped (100) p-type silicon wafers ($\rho = 0.001$–$0.002\,\Omega$ cm, thickness 505–545 μm) were used as conductive silicon substrates to study water oxidation in the dark. Moderately phosphorous-doped (100) n-type silicon wafers ($\rho = 0.14$–$0.24\,\Omega$ cm, thickness 450 μm) were used for Type I MIS Schottky junction photoanodes. Buried junction devices were made with n-type silicon wafers and were subjected to a standard clean using a Semitool Spray Acid: first the wafers are subjected to ozone and DI water, then NH$_4$OH (2000:1) is added to help remove particles and organics, and finally ozone, DI water and HF (1,150:1) are used to etch the chemical oxide and regenerate the surface oxide, also removing any metallic species. The implant is performed with a 4×10^{15} cm^2 dose of boron at 15 keV. Following the implantation, the samples were annealed at 950 °C for 40 min. The junction depth was characterized in two ways. First the surface was bevelled at a known angle through the p$^+$ surface region and the nSi was stained to allow an optical measurement to determine the depth. This resulted in a calculated depth of 448 nm. Second, the p$^+$ region was preferentially etched using a HNO$_3$:HF solution and scanning electron microscopy (SEM) was used to directly measure a junction depth of ∼460 nm. ALD-TiO$_2$ layers were amorphous as deposited, as detailed previously[39]. More details are also given in the Supplementary Information.

Devices for SiO$_2$ thickness experiments were fabricated by slot plane antenna plasma oxidation. Before SiO$_2$ growth, prime grade Si (100) wafers were prepared using a three-part clean: 10 min at 50 °C in 5:1:1 H$_2$O:H$_2$O$_2$:NH$_4$OH to remove trace organics, 10 min at 50 °C in 5:1:1 H$_2$O:H$_2$O$_2$:HCl to remove trace metal ions, and then 30 s in 2% HF to remove the silicon dioxide layer. The SiO$_2$ layer is regrown with precise thickness control using the SPA method, which utilizes radical oxidation to grow ultrathin oxide layers with reproducibility equal to or greater than that of thermal oxidation, and at significantly lower temperatures, achieving 0.7 to 1.0% thickness non-uniformity for films of 1.5 to 10 nm thickness at temperatures as low as 400 °C (refs 30–32).

Device simulations were performed using Synopsys Sentaurus (Version I-2013.12-SP1). Default material properties, found within the software, were used for both silicon and SiO$_2$. Doping densities and junction depths were set to the material values reported in the main text and Supplementary Information for the silicon actually used. The material TiO$_2$ is not found within the Sentaurus default material database and therefore its material properties were added manually. Moderate n-type doping of 1×10^{17} cm^{-3} was assumed. For the TiO$_2$ band

structure we assumed an electron affinity of 4.2 eV (ref. 40) relative to vacuum and a bandgap of 3.2 eV (ref. 41). Optical constants for TiO$_2$ were incorporated over the desired spectral range from previous literature values[42]. The default Sentaurus parameters were used for the Shockley–Read–Hall lifetimes of 10 μs and 3 μs for electrons and holes, respectively. The front and back contact metals were iridium and aluminium, respectively, again reflecting the actual devices fabricated in this study. Modelling of the electrodes consisted of defining the work functions of each contact. We assumed work functions of 5.1 eV and 4.1 eV for iridium and aluminium, respectively, based on ranges for values of 5.0–5.67 eV and 4.06–4.26 reported in the literature[43]. Surface recombination velocities of 2.57×10^6 cm s^{-1} and 1.93×10^6 cm s^{-1} were assumed for electrons and holes, respectively, at the iridium–TiO$_2$ interface. This interface is modelled using the Schottky contact physics model built into Synopsys Sentaurus. For all materials we assume the presence of both SRH and radiative recombination defined by the models present in the Synopsys Sentaurus Device User Guide using the specified material properties listed above and those included as default parameters in the Synopsys Sentaurus material database. Optical generation was modelled using the transfer matrix method (TMM) using a representative version of the AM1.5G spectrum. Description of optical generation models used by Sentaurus can be found within the Sentaurus Device User Guide.

References

39. Scheuermann, A. G., Lawrence, J. P., Gunji, M., Chidsey, C. E. D. & McIntyre, P. C. ALD-TiO$_2$ preparation and characterization for metal–insulator–silicon photoelectrochemical applications. *ECS Trans.* **58,** 75–86 (2013).
40. Fuke, N. *et al.* Influence of TiO$_2$/electrode interface on electron transport properties in back contact dye-sensitized solar cells. *Solar Energy Mater. Solar Cells* **93,** 720–724 (2009).
41. Pattantyus-Abraham, A. G. *et al.* Depleted-heterojunction colloidal quantum dot solar cells. *ACS Nano* **4,** 3374–3380 (2010).
42. Devore, J. R. Refractive index of rutile and sphalerite. *J. Opt. Soc. Am.* **41,** 416–417 (1951).
43. Haynes, W. M., Bruno, T. J. & Lide, D. R. (eds) *CRC Handbook of Chemistry and Physics* 95th edn, 12–124 (CRC Press, 2014).